STUDY ON STABILIZATION OF LARGE-SCALE COAL-FIRED LINEAR MHD GENERATORS

Takeshi Iwashita

December 1997

STUDY ON STABILIZATION OF LARGE-SCALE COAL-FIRED LINEAR MHD GENERATORS

Takeshi Iwashita

December 1997

Contents

Chapter 1 Introduction

1.1 Brief History of MHD Power Generation

Currently, the major energy source of human activities is fossil fuels such as oil, coal and natural gas. The consumption of a large amount of fossil fuels, however, not only causes environmental problems such as global warming and acid rain, but also leads to an exhaustion of fossil fuels themselves. Given the current scenario, it is therefore necessary to develop power generation technology for utilizing fossil fuels with high efficiency and low levels of pollution.

An MHD power generation system has a potential to satisfy the above requirements. The MHD power generation system can increase the total thermal efficiency of power plants when combined with a conventional steam Rankine cycle 1). It is easy to remove SO_x and NO_x from the exhaust gas in the MHD power generation system 2). The MHD power generation system also has a high potential to reduce CO_2 emission due to its high efficiency. In addition, a concept of CO_2 recovery MHD power generation system 3) has recently been proposed, showing a drastic reduction of CO_2 emissions with sufficiently high-thermal efficiency. In order to take advantage of these MHD power generation potentials, a great deal of research4) 5) on the MHD power generation has been carried out in many countries.

MHD generators are classified into three types according to their working fluid. The first is the open-cycle MHD generator in which nearly 3000 K of fossil fuel combustion gas is used. The second is the closed-cycle MHD generator in which about 2000 K of nonequilibrium plasma of alkali metal seeded noble gas is used. The last is the liquid metal MHD concept. In the present thesis, the open-cycle coal-fired MHD generator is studied.

In the field of open-cycle MHD power generation, a number of experiments and theoretical studies have been performed 4) in many countries. In the U.S.A., many experiments have been carried out using large-scale test facilities. These include the CDIF (Component Development and Integration Facility) in Montana, and the CFFF (Coal Fired Flow Facility) in Tennessee, which were with support from the DOE (U.S. Department of Energy) since the 1980's 6). The CDIF was a test facility with 50 MW thermal input for MHD topping cycle components using coal as fuel.

The CDIF channel was operated with a Faraday mode and a diagonal mode by the MSE (Mountain State Energy), achieving a power output of over 2 MW. Total operation time for power runs exceeded 600 hours [7). The CFFF was established for developing and testing of MHD bottoming cycle components. The CFFF was operated with a nominal thermal input of 28 MW by the UTSI (University of Tennessee Space Institute), and the total operation time exceeded 3600 hours [8). Although these experimental results proved the potential of coal-fired MHD power generation, the U.S. DOE MHD program was terminated due to national budget constraints in FY 1993. It is expected that the next experimental program of MHD power generation of commercial-scale will be set up soon.

In Russia [9), the majority of experimental research on MHD power generation has been conducted at the U-25 test facility. The U-25 is a large-scale complex facility with 250 MW thermal input, and is based on natural gas as fuel. The U-25, operated by IVTAN(Institute for High Temperatures), obtained a maximum power output of 25 MW and succeeded in achieving a continuous operation of 250 hours. After the successful development of the components of an MHD system and testing at the U-25 facility, Russia planned a 500 MW commercial MHD power plant project in 1980. The plant was designed to have a thermal input of 1100 MW obtained from burning natural gas with preheated air. The total expected power output was 582 MW (270 MW from MHD and 312 MW from the steam bottoming portion). The steam turbine part of the plant was established and began generating electrical power in 1988. However, soon after, in 1989, the 500 MW MHD power plant project was suspended due to radical changes in the country's investment policies and also due to the complexity of manufacturing large superconducting magnets. Now, the U-25 facility has been modified to a U-25M facility, with a thermal input of about 300 to 400 MW, which is being prepared for experiments of coal-fired MHD power generation and closed cycle MHD power generation.

In Japan [10), the open-cycle coal-fired 15 MWth MHD generator with an electrical power output of 100 kW was established in 1981 at ETL (Electro-Technical Laboratory) under MITI's (Ministry of International Trade and Industry) national MHD project and accumulated a total operation time of 430 hours. Although MITI's MHD project having achieved its objectives, ended in 1989, the next large-scale project was never planned. Research for the open-cycle MHD has, however, been continued in several universities such as Hokkaido University, Tokyo Institute of Technology and Kyoto University. In the field of experimental research for open-cycle MHD power generation, the 5 MWth oil-fired open-cycle MHD test facility at CARET (Center for Advanced Research of Energy Technology) at Hokkaido University is in operation.

A variety of experimental works have also been carried out in Australia 11), China12), India 13), Italy 14) and Poland 15).

1.2 Analysis of 25 MWth Coal-Fired MHD Generator at IEE, China

The most energetic experimental research activities on open-cycle MHD power generation in the world are presently being performed in China 12) 16) 17) 18) 19) 20). Research on MHD power generation in China started in 1962, showing a variety of MHD activities. Since 1987 coal-fired MHD power generation technology has been included in the Chinese High-Tech Research and Development Program (863 Program). In this project, a coal-fired MHD generator with 25 MW thermal input was designed and constructed at IEE (Institute of Electrical Engineering), Chinese National Academy of Sciences in 1992. After the first power generating experiment was carried out at the end of 1992, several experiments were performed in 1993 and 1994, yielding a maximum power output of about 120 kW.

For these experiments, a small-scale cooperation has been initiated between Japanese researchers at Kyoto University and a Chinese research group at IEE, where the Chinese side provides experimental data and the Japanese side carries out numerical analyses. With regard to this cooperation, the present thesis analyzes the 25 MWth Chinese MHD generator in Chapter 2. This analysis has three main objectives. The first is to estimate the various quantities which could not be measured experimentally due to the high temperature and the high flow velocity of the working fluid. The second is to evaluate the potential of the Chinese facility. The third is to confirm the validity of the simulation model used in the present thesis, in particular, of the model of thermodynamical properties of coal, in comparison to the experimental results. In the beginning of Chapter 2, basic equations for gasdynamics and electrodynamics used in the present thesis are introduced. The chapter then shows the numerical results of analyses for the Chinese MHD generator.

1.3 Stability Analyses of Open-Cycle MHD Generator of Commercial-Scale

After the success of the pilot plant-scale MHD power generation experiments described in section 1.1, numerical research was performed and a proposal to a U.S. national program was made for realizing commercialization of the open-cycle MHD power generation. M. Ishikawa et al. carried out a preliminary conceptual design of the commercial-scale coal-fired MHD-steam combined power generation system with a thermal input from 1000 MW to 2000 MW, showing that a total thermal efficiency of over 60 % (HHV) can be achieved 3). Y. Fujita et al., based on this system design, performed the conceptual design for the commercial-scale diagonal-type MHD generators and analyzed the behavior of MHD generators with external control circuits 21). This analysis, however, identified possible unstable behaviors in the commercial-scale diagonal-type MHD generators. Since the diagonal type generator has the advantage of simple load circuit constitution when compared with the Faraday type generator, the diagonal type is more suitable for large-scale linear type MHD generators which have many electrode pairs. It is, therefore, important to stabilize the commercial-scale diagonal-type MHD generator in order to realize the commercialization of MHD power generation. In the present thesis, stabilization analyses are carried out for diagonal-type MHD generators of commercial-scale.

A number of analytical studies on the unstable phenomena of weakly ionized plasma have pointed out the possibility of magneto-acoustic instability in the open-cycle MHD generator since the early works by Velikhov 22) and McCune 23) in the 1960's. Most of these 22) 23) 24) 25) have examined the stability of the MHD generator by calculating the local, time or spatial growth rates of magneto-acoustic waves derived from a dispersion equation. On the other hand, the unstable behavior of the MHD generator caused by the magneto-acoustic instability has not been found in any experiments performed until now. This is probably because the scale of generators has not been large enough or because the magnetic flux density has been rather small.

M. Ishikawa and A. Kyogoku et al. evaluated the local growth rates of traveling waves in the above mentioned commercial-scale diagonal-type MHD generator, showing that the instability results from the growth of magneto-acoustic waves 26). However, their local linear analysis is not sufficient as will be clear from the following considerations.

- The local linear analysis is not valid for examining the behavior of long wavelength disturbances. Accordingly, their analysis cannot examine the effects of electrical and gasdynamical boundary conditions on the stability of the generator.

- Their analysis does not explain how to suppress the wave growth by control of operational conditions of the MHD generator since effects of the boundary conditions are not considered.

Due to the above, it is therefore necessary to carry out the channel-length scale stability analysis, which takes into account electrical and gasdynamical boundary conditions. Rutkevich et al. performed a stability analysis based on the WKB method for subsonic MHD generators, finding the resonance instability caused by reflections of acoustic waves at the channel ends 27) 28). The WKB method, however, is not valid for low-frequency traveling waves. The low frequency waves which have channel-scale wavelength are apt to be affected by the loading condition of the generator and may lead to instability caused by interaction with the load current fluctuation. This instability, induced by the interaction between flow disturbance and load current fluctuation, was first discussed theoretically by Fishman 29) for supersonic single-loaded Hall generators, and was later studied by Marty et al. 30) for supersonic disk single-loaded generators. T. Matsuo et al., extending the technique presented by Fishman, proposed a method of linear stability analysis 31) for supersonic disk multi-loaded MHD generators, showing that multiple-loading schemes are effective in suppressing the magneto-acoustic instability. T. Matsuo et al. also proposed a method of linear stability analysis for subsonic MHD generators taking into consideration their gasdynamical boundary conditions, and showing that the inlet boundary condition greatly affects the stability of generators 32). The analyses for disk generators suggest the possibility that the commercial-scale diagonal-type MHD generators are also stabilized by the control of their operational condition. In Chapters 3 and 4, the effects of boundary conditions on the stabilization of diagonal type generators are examined through the application of the channel-length scale analysis. Diagonal type generators have many electrodes, unlike disk generators. Thus, the control of the electrode current may stabilize generators. This possibility is also examined in these chapters.

Chapter 3 discusses the stability of supersonic diagonal-type MHD generators using a sensitivity analysis and a linear stability analysis, which have been proposed for disk MHD generators 31). The sensitivity analysis evaluates spatial growth rates of flow disturbances during propagation along the channel. The linear stability analysis calculates the time growth rate of the load current disturbance which circulates through the channel and the load circuit. In this chapter, the author investigates the loading condition which stabilizes the generator. The effect of inserting inductors into the diagonal links is also examined.

Chapter 4 deals with subsonic diagonal-type MHD generators using a local linear perturbation analysis and a channel-length scale linear stability analysis. The local linear perturbation analysis estimates the local growth rates of traveling waves in the MHD generator using a dispersion equation. The channel-length scale linear stability analysis, which has been proposed for disk MHD generator 32), deals with the resonance instability related to gasdynamical boundary conditions. At first, the author analyzes the conventional type subsonic MHD generator in which the flow velocity is designed to be near the sound velocity, showing the MHD generator is apt to be unstable. Then the author proposes a new conceptual design for the subsonic MHD generator in which the flow velocity is relatively low. The analyses show that the newly designed channel works stably, generating a sufficient power output.

In Chapter 5, a subsonic Faraday type MHD generator is analyzed. Since a large-scale Faraday type MHD generator requires a complex external load circuit, it may not be suitable as a commercial-scale MHD power generation system. The progress of power electronics technology will, however, decrease the difficulties found in the external load circuit for the Faraday type generator in future. The author therefore carries out a local linear perturbation analysis and a channel-length scale linear stability analysis for the Faraday type MHD generator, examining the effect of loading conditions on the stability of the generator.

1.4 Analysis of Interconnecting System of Large-Scale Diagonal-Type MHD Generator and AC Power System

In Chapter 4, the author succeeded in producing a conceptual design for the subsonic diagonal-type MHD generator which works stably without severe control of electrode currents. Chapter 6 discusses the behavior of the subsonic diagonal-type generator connected with an AC power system. When an MHD generator is connected with an AC power line, an inversion system is required because the output of MHD generator is DC. Inverter systems always bring periodic disturbances into the MHD channel flow and it is therefore necessary to conduct stability analyses for the MHD generator under the condition of strong coupling between the MHD generator and the inversion system, even though general stability analyses will show that the MHD generator is stable against small disturbances.

Some studies on the connection of an MHD generator into an AC power network have already been carried out both experimentally and analytically. The CDIF channel provided about 2 MWe to the power grid of Montana State through the inversion system 33) 34). In analytical studies, a great deal of research on basic components of inversion system have been performed with simplified generator models34) while some research on the interaction of MHD generator and AC power network have been carried out with detailed generator models 35) 36). Most of these analytical works, however, do not discuss the effects of the interaction on the stability of the large-scale MHD generator. N. Hayanose and A. L. Tan et al. analyzed a large-scale disk type MHD generator connected with an AC power network, showing that some inversion system controls are necessary for restoring the MHD generator to a stable state when line faults occur in the power system 36). On the other hand, no study has been reported on large-scale linear MHD generators when connected into the AC power network through inversion systems.

In Chapter 6, the author first analyzes the large-scale subsonic diagonal-type MHD generator connected with an AC power network under the nominal condition. The MHD generator with the AC power network is then analyzed when faults such as line faults occur in the AC power network.

Chapter 2 Analysis of Experiments of Chinese 25 MWth Coal-Fired MHD Generator

2.1 Introduction

This chapter presents an analysis of the Chinese coal-fired Faraday type MHD generator which has a thermal input of 25 MW $^{12)}$. The gasdynamical condition at the inlet is first estimated according to the analysis of experimental data provided by Chinese researchers. Next, the following three key parameters of electrical properties are estimated with experimental results from 1992 and 1993: (1) effective conductivity, (2) leakage resistance in the flow direction, and (3) leakage resistance in the Faraday direction. Next, the author analyzes the power run in November, 1994 which yielded the maximum power output of 119.7 kW. The author also predicts the performance of the channel with diagonal operation and evaluates the hidden capabilities of the Chinese facility.

The analyses of the Chinese channel and the comparison with the experimental data can give a validation and a confidence of mathematical models adopted in the present thesis.

2.2 Basic Equations

2.2.1 Coordinate System

The coordinate system used in the present thesis is shown in Figure 2.1. The plasma flow runs along the x direction and the magnetic field is applied in the $+z$ direction.

2.2.2 Approximations and Assumptions

Some approximations are used generally when problems of MHD energy conversion are being presented. The approximations and assumptions which are used in the present thesis are listed below.

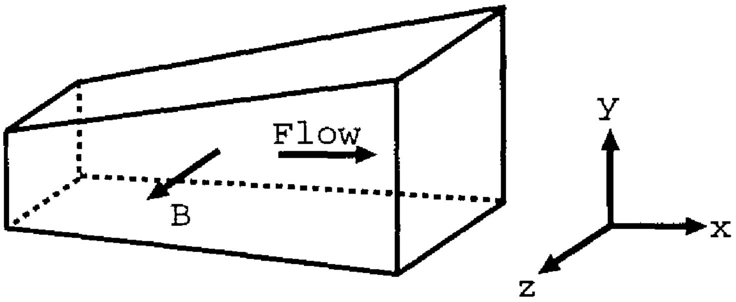

Figure 2.1: Coordinate system

(1) The applied magnetic flux density does not vary with time.

(2) The induced magnetic field is negligible since the magnetic Reynolds number of the gas plasma is much smaller than unity 1) .

(3) The displacement current is much smaller than the conduction current and is negligible.

2.2.3 Basic Equations for Gasdynamics

The basic equations used for the gasdynamical part 37) 38) are given by the conservation of the mass, the momentum and the energy, and by the state equations of working gas. A one-dimensional approximation is applied to the present gasdynamical analysis.

The one-dimensional conservation laws are given by

$$\partial \boldsymbol{U}/\partial t + \partial \boldsymbol{F}(\boldsymbol{U})/\partial x = \boldsymbol{S}(\boldsymbol{U}) \tag{2.1}$$

$$\boldsymbol{U} = \begin{pmatrix} U_1 \\ U_2 \\ U_3 \end{pmatrix} = \begin{pmatrix} \rho A \\ \rho u A \\ \rho(\varepsilon + u^2/2)A \end{pmatrix} \tag{2.2}$$

$$\boldsymbol{F}(\boldsymbol{U}) = \begin{pmatrix} \rho u A \\ (\rho u^2 + p)A \\ \rho u(\varepsilon + \frac{p}{\rho} + u^2/2)A \end{pmatrix} \tag{2.3}$$

$$\boldsymbol{S}(\boldsymbol{U}) = \begin{pmatrix} 0 \\ \mathrm{p}\mathrm{d}A/\mathrm{d}x + AJ_yB - f_{ric} \\ (\boldsymbol{J}\cdot\boldsymbol{E})A - q_{loss} \end{pmatrix} . \tag{2.4}$$

In the above equations t is the time, x the coordinate along the duct axis, A the duct cross section, ρ the gas mass density, u the gas velocity, ε the internal energy, p the static pressure, f_{ric} the friction, q_{loss} the heat loss; $\boldsymbol{E} = (E_x, E_y, 0)$ is the electric field, $\boldsymbol{J} = (J_x, J_y, 0)$ the electric current density and $\boldsymbol{B} = (0, 0, B)$ the magnetic flux density. The friction f_{ric} and the heat loss q_{loss} are given in Appendix A.

The state equations of working gas are written as

$$\rho = \rho(p, T), \quad \varepsilon = \varepsilon(p, T) \tag{2.5}$$

where T is the static temperature [39].

2.2.4 Relations for Electrodynamics

The relation between the electric field and the electric current density is given by the Maxwell equations and the generalized Ohm's law. The Maxwell equations are written below under the assumptions (1)-(3) in Subsection 2.2.2:

$$\nabla \cdot \boldsymbol{J} = 0 \tag{2.6}$$

$$\nabla \times \boldsymbol{E} = 0. \tag{2.7}$$

The generalized Ohm's law is given by

$$\boldsymbol{J} = \sigma(\boldsymbol{E} + \boldsymbol{u} \times \boldsymbol{B}) - \frac{\beta}{B}(\boldsymbol{J} \times \boldsymbol{B}) + \frac{\beta\beta_i}{B^2}(\boldsymbol{J} \times \boldsymbol{B}) \times \boldsymbol{B} + \frac{\sigma}{n_e e}\nabla p_e - \tau\frac{D\boldsymbol{J}}{Dt} \tag{2.8}$$

where σ is the electrical conductivity, $\boldsymbol{u}$ the gas velocity, β the hall parameter of electron, β_i the hall parameter of ion, p_e the electron partial pressure, n_e the electron density, e the magnitude of electron charge, τ the mean free time between collisions and $\frac{D}{Dt}$ the Lagrange derivate. The 3rd, 4th and 5th terms on the right are much smaller than the 1st and 2nd terms on the right and can be neglected [1] in the present analysis. Consequently, the generalized Ohm's law can be written as

$$\boldsymbol{J} = \sigma(\boldsymbol{E} + \boldsymbol{u} \times \boldsymbol{B}) - \frac{\beta}{B}(\boldsymbol{J} \times \boldsymbol{B}). \tag{2.9}$$

2.3 Numerical Schemes

2.3.1 Gasdynamics

In the present thesis, the one-dimensional gasdynamical equation (2.1) is solved by the 1969 MacCormack two-step explicit method [40] [41]. The procedure is given as follows.

Predictor step:

$$\Delta \boldsymbol{U}_i^n = -\frac{\Delta t}{\Delta x}(\boldsymbol{F}_{i+1}^n - \boldsymbol{F}_i^n) + \Delta t\, \boldsymbol{S}_i^n \tag{2.10}$$

$$\boldsymbol{F}_i^* = \boldsymbol{F}(\boldsymbol{U}_i^n + \Delta \boldsymbol{U}_i^n), \quad \boldsymbol{S}_i^* = \boldsymbol{S}(\boldsymbol{U}_i^n + \Delta \boldsymbol{U}_i^n) \tag{2.11}$$

Corrector step:

$$\Delta \boldsymbol{U}_i^* = -\frac{\Delta t}{\Delta x}(\boldsymbol{F}_i^* - \boldsymbol{F}_{i-1}^*) + \Delta t\, \boldsymbol{S}_i^* \tag{2.12}$$

$$\boldsymbol{U}_i^{n+1} = \boldsymbol{U}_i^n + \frac{1}{2}(\Delta \boldsymbol{U}_i^n + \Delta \boldsymbol{U}_i^*) \tag{2.13}$$

where n is the time step and i the i-th node along the duct, Δt and Δx the time and space increments, respectively. At each step, the gas mass density ρ and the internal energy ε are given from the gasdynamical variable vector $\boldsymbol{U}$ as

$$\rho = \frac{U_1}{A}, \quad \varepsilon = \frac{U_3}{U_1} - \frac{U_2^2}{2U_1^2}. \tag{2.14}$$

After that, the static pressure and the static temperature are determined from the state equations (2.5) by using the Newton-Raphson method.

2.3.2 Electrodynamics

The two-dimensional electric equivalent circuit method [42] [43] is applied, where the MHD channel is divided into small regions and the voltage-current characteristics of each region are expressed by a four-terminal equivalent circuit as shown in Figure 2.2.

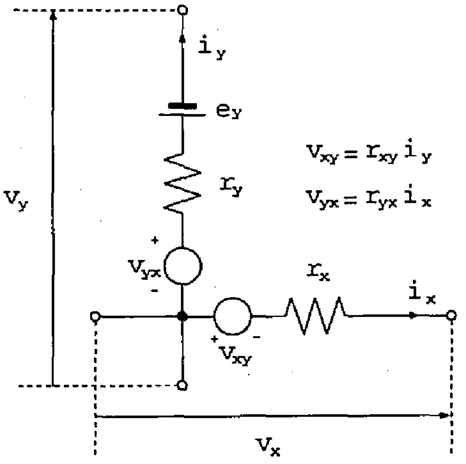

Figure 2.2: Four-terminal equivalent circuit

Under one-dimensional approximation of gasdynamics, the gas velocity $\boldsymbol{u}$ and the magnetic flux density $\boldsymbol{B}$ are written as:

$$\boldsymbol{u} = (u, 0, 0), \qquad \boldsymbol{B} = (0, 0, B). \tag{2.15}$$

From Equations (2.9) (2.15), the following two-dimensional equations are derived for electrodynamics:

$$E_x = (J_x + \beta J_y)/\sigma \tag{2.16}$$

$$E_y - uB = (-J_x + J_y)/\sigma. \tag{2.17}$$

When a divided region has the length s_e in the x-direction, the hight h_e in the y-direction and the width d_e in the z-direction, the following expressions are obtained from Equations (2.16) and (2.17) for the small regions:

$$\begin{pmatrix} v_x \\ v_y + e_y \end{pmatrix} = \begin{pmatrix} r_x & r_{xy} \\ -r_{yx} & r_y \end{pmatrix} \begin{pmatrix} -i_x \\ -i_y \end{pmatrix} \tag{2.18}$$

$$r_x = s_e/\sigma d_e h_e, \quad r_{xy} = r_{yx} = \beta/\sigma d_e \tag{2.19}$$

$$r_y = h_e/\sigma d_e s_e, \quad e_y = h_e u B \tag{2.20}$$

where v_x and v_y are the terminal voltages of the four-terminal equivalent circuit in the x- and y-directions, and i_x and i_y the terminal currents.

Figure 2.3 shows the schematic of the network of four terminal equivalent circuits. One electrode pitch is divided by two nodes, and the channel height in the y-direction is divided by nine nodes, including slag layers.

2.3.3 Thermodynamical Properties

In the present thesis, coal combustion gas is selected as the working fluid. The thermodynamical properties including the gas mass density ρ, the enthalpy h, the internal energy ε, the hall parameter β and the electrical conductivity σ are independently calculated with thermodynamical equilibrium approximation. These properties are given by the approximate functions of static temperature and static pressure, which are reduced from thermodynamical calculations [39]. The functions of the thermodynamical properties are described by

$$\rho = \sum_{j=1}^{5} \sum_{k=1}^{5} \rho_{jk} p^{j-3} T^{k-2} \tag{2.21}$$

$$h = \sum_{j=1}^{5} \sum_{k=1}^{5} h_{jk} p^{j-3} T^{k-2} \tag{2.22}$$

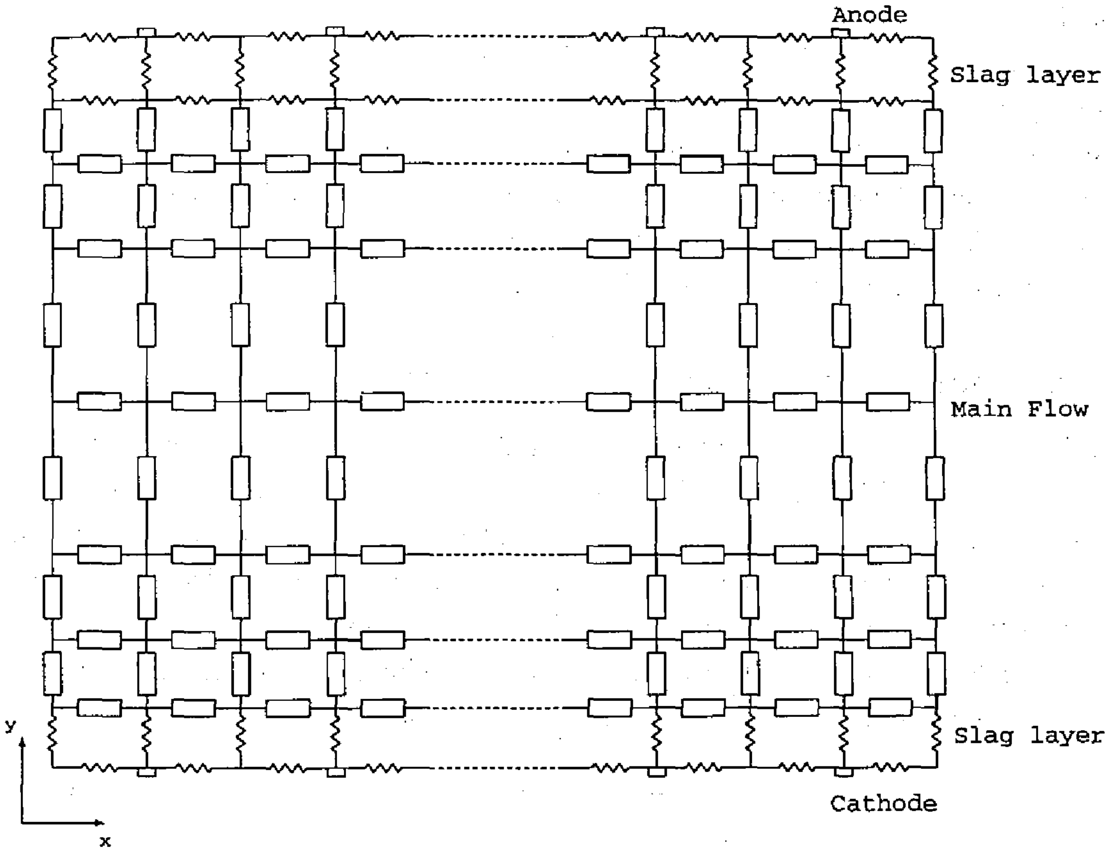

Figure 2.3: Schematic diagram of electrical equivalent circuits

$$\varepsilon = h - \frac{p}{\rho} \tag{2.23}$$

$$\beta = B \sum_{j=1}^{5} \sum_{k=1}^{5} \beta_{jk} p^{j-3} T^{k-2} \tag{2.24}$$

$$\sigma = \exp\left(\sum_{j=1}^{5} \sum_{k=1}^{5} \sigma_{jk} p^{j-3} T^{k-2}\right) \tag{2.25}$$

where ρ_{jk}, h_{jk}, β_{jk} and σ_{jk} are coefficients determined by the thermodynamical calculations.

In this chapter, the fuel is basically Datung coal from China and the oxidant is Oxygen-enriched air. Since its combustion condition changes from experiment to experiment, the thermodynamical properties are calculated for each experiment. The experimental conditions have been reported in Ref. 17) and the composition of the coal is shown in Appendix B. Figures 2.4 depict the thermodynamical properties of the coal used in the power run at October, 1993.

2.3.4 Boundary Layer and Slag Layer

The MHD channel at IEE, China, is still small, and therefore, the boundary layer and slag layer on the channel walls have relatively large effects on the gasdynamical behavior. At first, the steady gasdynamical calculation is carried out without the magnetic field, where the boundary layer and slag layer are neglected, and the designed values are used for the thermodynamical properties of gas and for the inlet boundary condition. The boundary layer thickness δ and the displacement thickness δ_d can now be estimated with turbulent boundary layer theory $^{44)}$.

$$\delta = 0.37x\left(\frac{ux}{\nu}\right)^{-0.2} \tag{2.26}$$

$$\delta_d = \frac{\delta}{8} \tag{2.27}$$

where $\nu = \mu/\rho$ is the kinematic viscosity and μ the viscosity. The thickness is then fixed in all the other computations. It is assumed that the slag thickness, 1 mm, is constant along the channel.

The electrical characteristics of the slag layer are expressed by leakage resistances as is shown in Figure 2.5. The accumulated experience $^{21)}$ $^{45)}$ indicates that the leakage resistance along the cathode wall in the x-direction is much smaller than the other leakage resistance and thus is critically important. Accordingly, leakage resistance of the cathode wall in the x-direction, R_x, is determined from results of

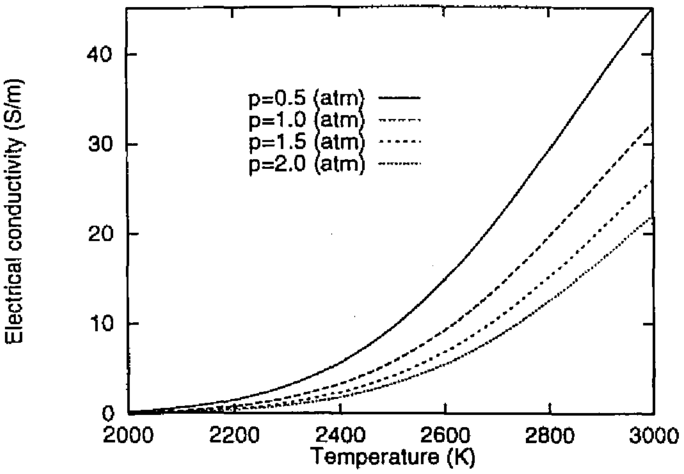

(a) Electrical conductivity

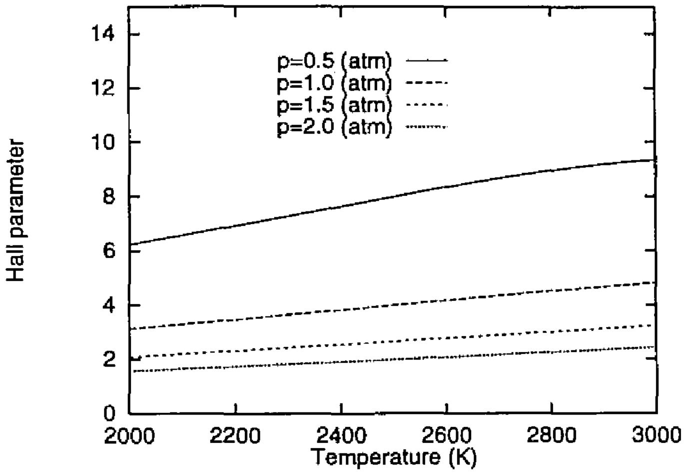

(b) Hall parameter (B=1 T)

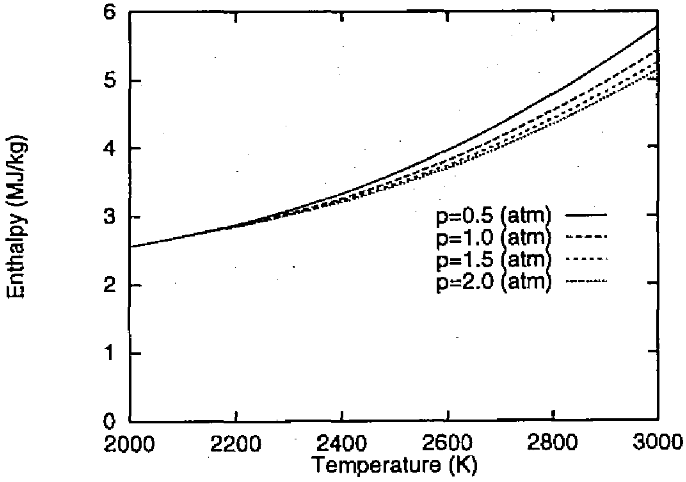

(c) Enthalpy

Figure 2.4: Thermodynamical properties of coal used in power run at October 1993

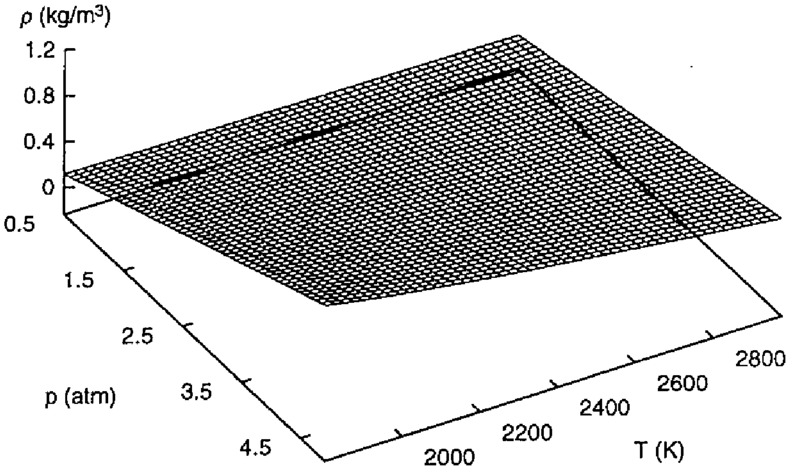

(d) Gas mass density

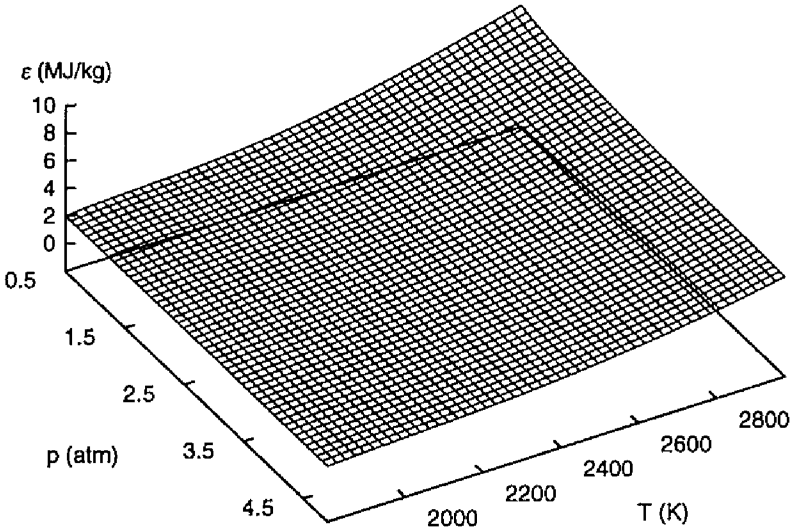

(e) Internal energy

Figure 2.4: Thermodynamical properties of coal used in power run at October 1993

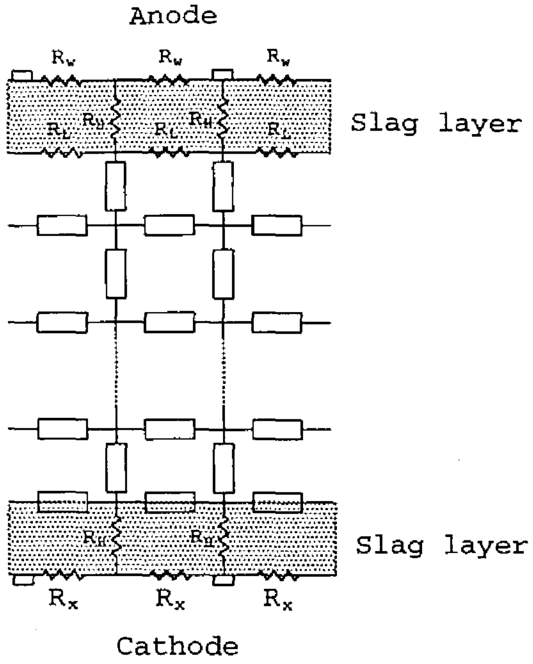

Figure 2.5: Equivalent model of slag layer with leakage resistances

the Chinese experiments. On the other hand, the other leakage resistances R_L, R_w and R_H are assumed to be the same values as obtained for CDIF channel [45]:

$$R_L = 95.0\ \Omega, \quad R_w = 190\ \Omega, \quad R_H = 0.963\ \Omega. \tag{2.28}$$

A cathode open-gap has not been observed in the Chinese experiments [17], and thus these effects are not included in the present analysis.

2.4 Coal-Fired MHD Generator Operated in IEE, China

2.4.1 Experimental Facility at the IEE

The experimental facility constructed at the IEE consists of a coal combustor, a conventional magnet, and an MHD channel with supersonic diffuser. Figure 2.6 shows the schematic diagram of the Chinese facility. Figure 2.7 depicts the channel structure [12] and Figure 2.8 shows the distribution of the applied magnetic flux density. The generator channel consists of two linearly divergent sections which have different semi-expansion angles, 1.47° for the first section and 0.81° for the

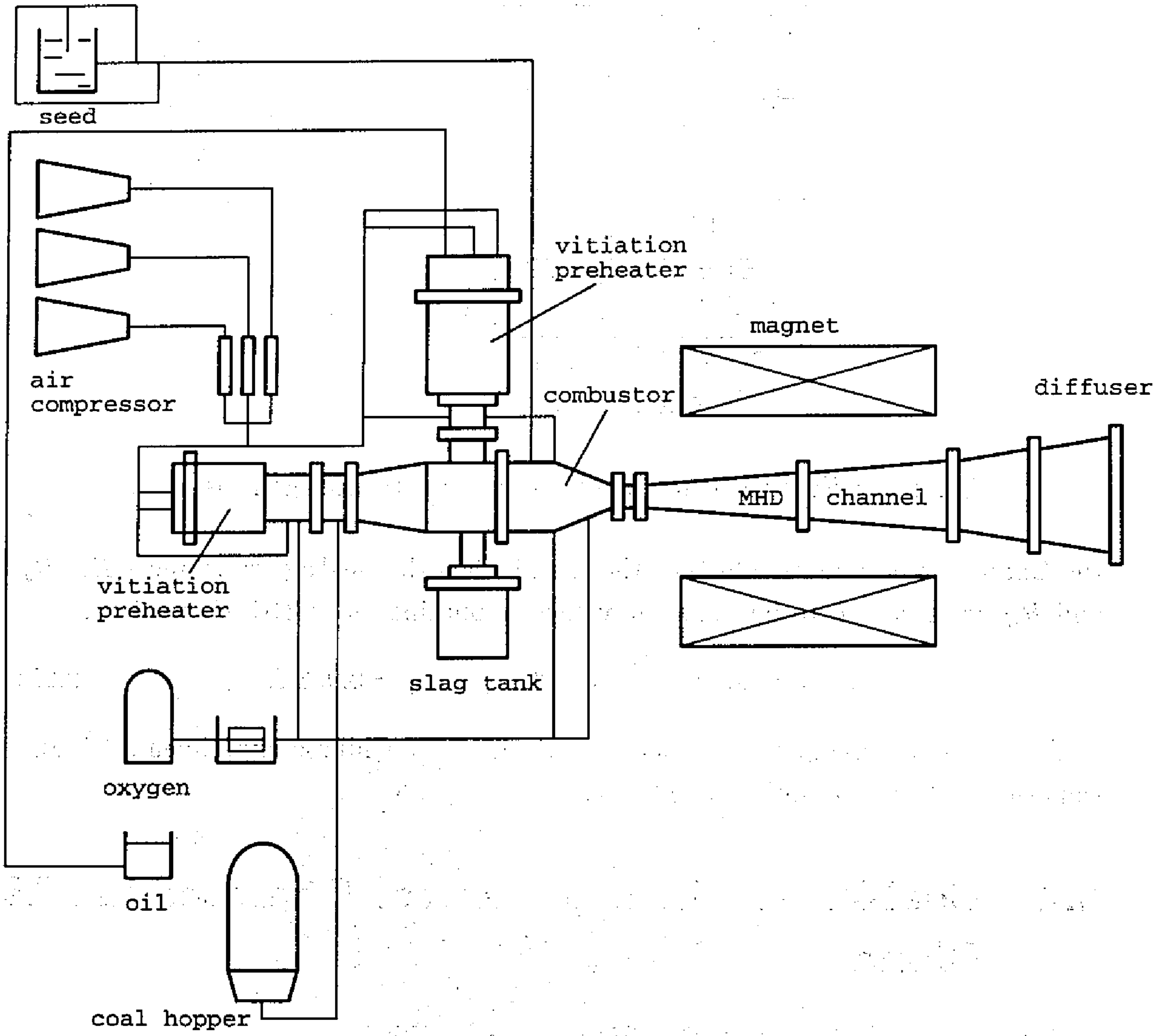

Figure 2.6: Schematic diagram of Chinese coal-fired MHD facility

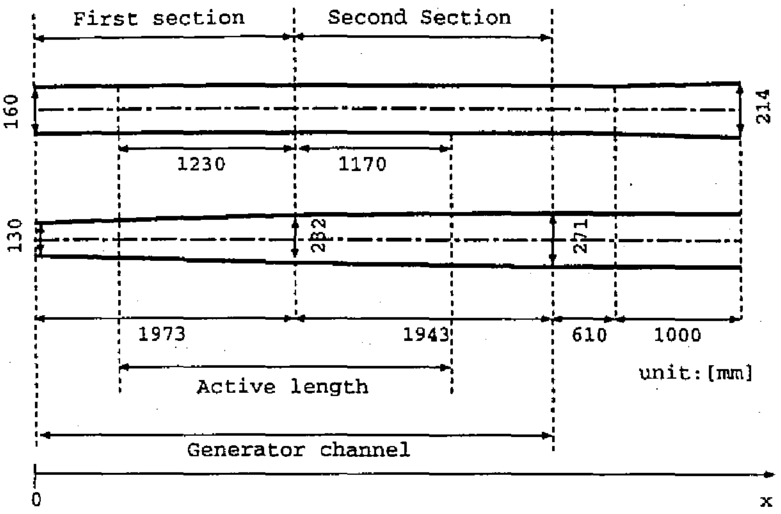

Figure 2.7: Structure of Chinese channel

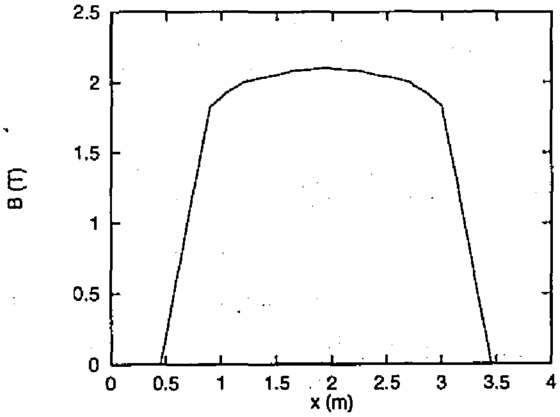

Figure 2.8: Distribution of applied magnetic flux density

second section. Table 2.1 lists the basic specifications of the MHD generator. The rated thermal input is 25 MW, the peak value of magnetic flux density is 2.1 T and the channel length is 3.98 m, where the active length for the MHD generator is 2.4 m. The MHD channel consists of 80 pairs of electrodes. Table 2.2 shows the estimated design condition 12) of the Chinese channel.

Table 2.1: Basic specifications of MHD generator at IEE, China

Total length	3.916 m
Length of 1st section	1.937 m
Length of 2nd section	1.943 m
Cross section at channel inlet	0.16 × 0.13 m^2
Cross section at channel exit	0.16 × 0.27 m^2
Cross section at interface between 2 sect.	0.16 × 0.23 m^2

Table 2.2: Estimated design condition of MHD channel at IEE, China

	Channel inlet	Channel exit
Mach number	1.20	1.03
Static temperature	2589 K	2325 K
Static pressure	1.36 atm	0.712 atm
Velocity	1080 m/s	880 m/s
Power output	161.3 kW	
Total axial voltage	1861.1 V	

2.4.2 Brief Summary of Experiments

The experimental test conditions and power output 12) 17) 18) 19) are summarized in Table 2.3. The first power test 17) was carried out in December, 1992, showing rather low performance caused mainly by the water leakage occurring at the nozzle. The power output was about 30 kW. The experimental data for the open-circuit condition showed that the Hall field was induced along the channel in spite of the open-circuit condition, suggesting electrical leakage in the y-direction.

The second power run 17) was conducted in October, 1993. The power output was much improved, resulting in 98.2 kW. Direct measurement of the electrical conductivity was tried and reported in Ref. 17), showing rather low conductivity compared with the theoretical prediction estimated from the thermodynamic calculation.

The third power run [17] was conducted in April, 1994. The power output, 80.3 kW, was rather low. This is mainly because the coal used was not of high quality, and high temperatures could not be obtained in the coal combustor, resulting in low electrical conductivity in the MHD channel.

The fourth power run [18] was carried out in November, 1994. The power output, 119.7 kW, was rather high. This is because the first half of the channel was improved to reduce the leakage current in the y-direction.

Table 2.3: Experimental test results

Date	Dec. 1992	Oct. 1993	Apr. 1994	Nov. 1994	Designed
Mass flow rate kg/s	4.048	4.035	4.243	3.800	4.00
Thermal input of combustor MW	26.12	22.89	unknown	30.21	26.92
Power output kW	33.7	98.2	80.3	119.7	161.3

2.4.3 Estimation of Condition of Channel Inlet

In the present analysis, the inlet gasdynamical condition is kept constant for the inlet boundary condition. The inlet gasdynamical condition is given by the mass flow rate, the static pressure and the static temperature at the inlet. The mass flow rate was reported in Ref. 17) and is listed in Table 2.3. On the other hand, the static pressure and the static temperature are estimated from the thermal input of channel and the inlet stagnation pressure. The inlet stagnation pressure of each experiment is not reported and is assumed to be 3 atm which is the designed value. The designed value of the thermal input of combustor is 26.92 MW, however, the experimental value is often lower than the designed one because of the low quality of coal. Accordingly, when the reported thermal input of combustor is lower than the designed value, the thermal input of the channel is calculated from the thermal input of combustor (reported) with the assumption that the heat loss at the combustor is 10 %. On the other hand, when the thermal input of combustor is larger than the designed one, the thermal input of the channel is assumed to be 25 MW which is the designed value.

Table 2.4 lists the estimated gasdynamical condition at the channel inlet. For the case of April, 1994, the thermal input of combustor has not been reported, and thus, the inlet static pressure and the inlet static temperature are assumed to be the designed values.

Table 2.4: Estimated inlet condition

Date	Dec. 1992	Oct. 1993	Apr. 1994	Nov. 1994	Designed
Mass flow rate kg/s	4.048	4.035	4.243	3.800	4.00
Static pressure atm	1.65	1.35	1.36	1.56	1.66
Static temperature K	2768	2612	2591	2850	2811

2.5 Results of Analyses

2.5.1 Estimation of Electrical Properties

In order to evaluate the performance of experiments, the following three key parameters of electrical properties are estimated: (1) effective conductivity, (2) leakage resistance between adjacent cathodes in the x-direction, R_x, and (3) leakage resistance between paired anode and cathode in the y-direction, R_y.

It is, however, rather difficult to decide these values. Three different experimental results are used to evaluate these values: (1) direct measurement of electrical conductivity, carried out in October, 1993, (2) open-circuit experiment done in December, 1992, and (3) second power run having generated 98.2 kW in October, 1993.

At first, the effective electrical conductivity is estimated by using the direct measurement. Figure 2.9 compares the experimental data and computational results of electrical conductivity along the channel, where experimental and computational values are represented by the circles and the solid line respectively. The experimental measurement was performed under the condition of no magnetic field 17), showing rather constant conductivity along the channel. The computation is carried out for identical conditions as the experiment, where the flow field is determined by the steady one-dimensional calculation. In Figure 2.9, the experimental value is lower than the theoretical value obtained from the thermodynamic equilibrium equation. The reason why the measured conductivity is low is not clear, though there are some possibilities, such as incomplete coal combustion, insufficient mixture

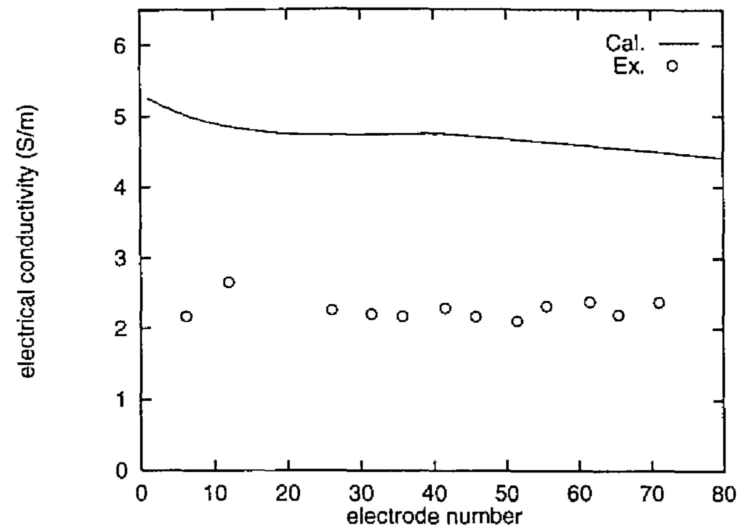

Figure 2.9: Comparison of experiment and computation of electrical conductivity (circles: experiment; line: computation)

of seeding material or measurement problems. The ratio of measured to calculated values is about 5/9, and thus, the effective conductivity of the gas is assumed to be 5/9 of the theoretical value as a rough estimation.

Next, the leakage resistances R_x and R_y are estimated by using the experimental data of the open circuit experiment and the second power run. These leakage resistances are parametrically changed, and the obtained power output for the experiment in October, 1993, and the Hall potential for the open-circuit run in December, 1992, are shown in Figure 2.10 and Figure 2.11, respectively. The differences of lines are 1 kW and 20 V, respectively, in Figure 2.10 and 2.11, while the bold lines indicate the experimental values of 98.2 kW for the output and 492 V for the Hall potential. The cross point in Figure 2.12 indicates the estimated leakage resistances in the x- and y-directions, which are 0.024 Ω for the x-direction and 82.4 Ω for the y-direction. These values are treated as basic values of leakage resistance, though the real situation varies, depending on each experiment.

2.5.2 Analysis of Experiment Performed in December 1992

The first power test was performed in December, 1992, showing rather low performance, mainly because the nozzle suffered from water leakage. The power output was about 30 kW. The water leakage at the nozzle may have cooled the gas temperature, resulting in low electrical conductivity. A simulation is performed where the

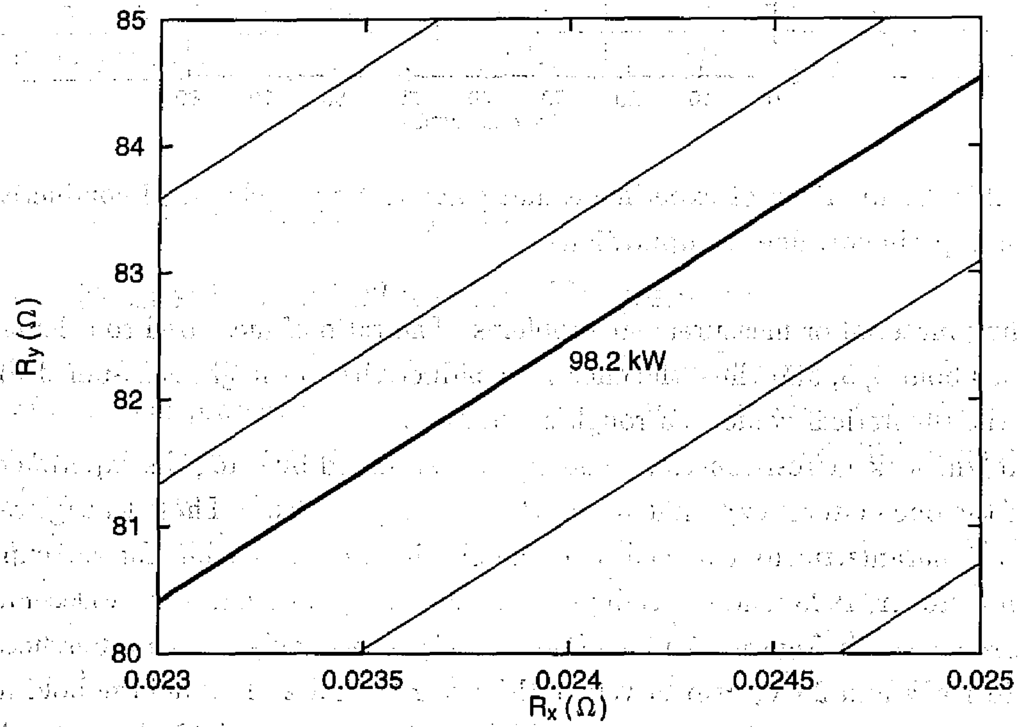

Figure 2.10: Effects of leakage resistances in the x- and y-directions on power output (difference of lines:1 kW, the bold line:98.2 kW)

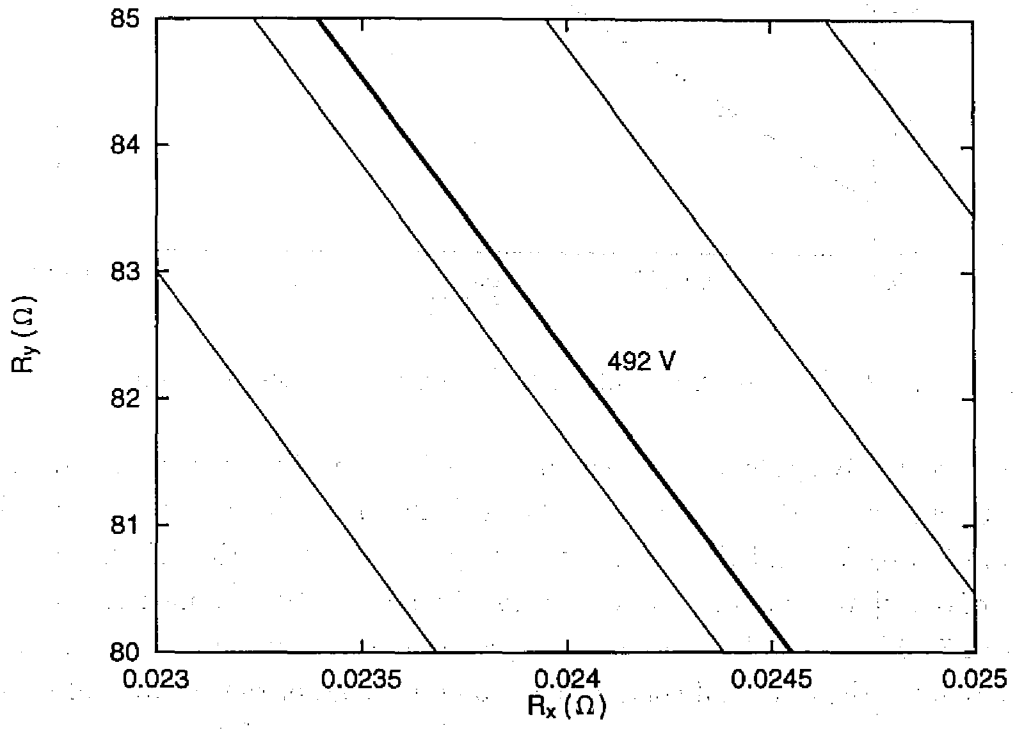

Figure 2.11: Effects of leakage resistances in the x- and y-directions on Hall potential (difference of lines:20 V, the bold line:492 V)

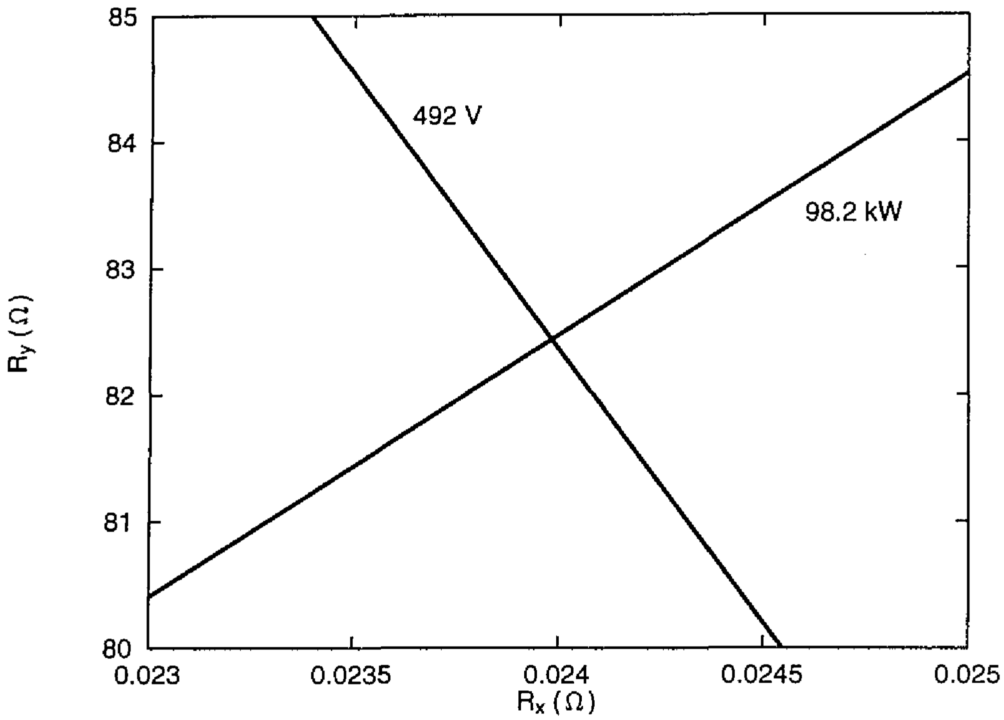

Figure 2.12: Estimation of leakage resistances in the x- and y-directions

electrical conductivity alone is reduced parametrically, while the leakage resistances are kept constant at the basic values. The calculation with the three basic values results in 121.0 kW, and the parametric analysis shows that the effective conductivities of one third, one fifth and one sixth of the theoretical value give the power output of 74.0 kW, 37.6 kW and 28.5 kW, respectively. This shows that the water leakage reduces the electrical conductivity to about 20% of the theoretical value.

The open-circuit voltage was also measured, where the Hall voltage along the channel was induced in spite of the open-circuit. Figure 2.13 depicts the experimental data and the computation of potential distribution along the channel, where the three basic parameters are used. The figure shows a rather good agreement of not only the Hall potential but also the distribution. Some discrepancy is, however, seen mainly at the downstream part, and therefore, some parametric calculations are performed for the distribution of effective leakage resistance in the y-direction. The leakage resistance of the first and second sections are set to be 60 Ω and 200 Ω, respectively. Figure 2.14 compares the distributions of Hall field for the experiment and computation, demonstrating a good agreement. This result indicates that the insulation in the y-direction of the second section is better than the first one.

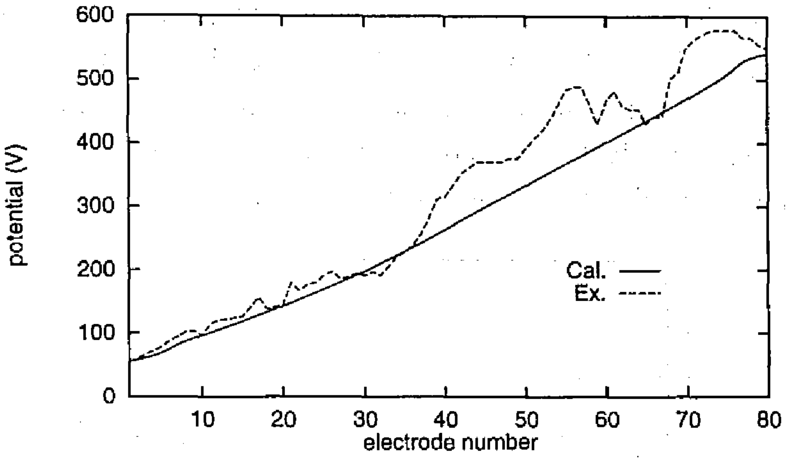

Figure 2.13: Comparison of potential distribution along channel with basic parameters for open-circuit run

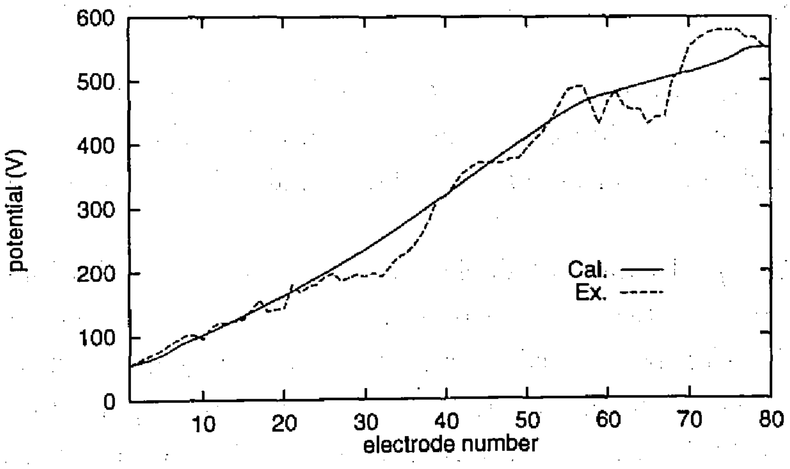

Figure 2.14: Comparison of potential distribution along channel with modified leakage resistance in the y-direction for open-circuit run

2.5.3 Analysis of Experiment Performed in October 1993

The second power run was performed in October, 1993. The power output improved to 98.2 kW, where the thermal input of combustor is 22.89 MW. The power output obtained by computation is 98.3 kW when the three basic values are used, showing a good agreement with experiment in the power output. Figure 2.15 shows the load resistances used in the calculation whose values are evaluated from the measured experimental data of load voltages and load currents.

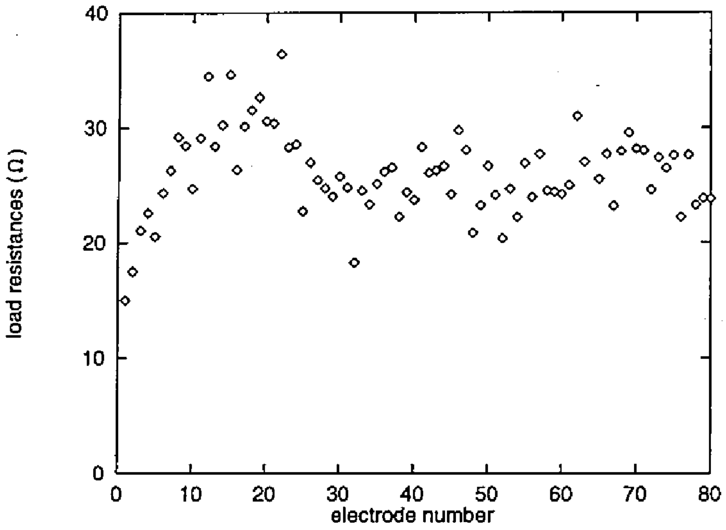

Figure 2.15: Load resistances used in the analysis of power run at October 1993

Figures 2.16 (a), (b) and (c) show distributions of flow field, where the flow is accelerated up to the midpoint of the channel, approaching a Mach number of nearly two, and then an almost constant Mach number is maintained to the end of the channel.

Figures 2.17 (a), (b) and (c) depict two-dimensional distributions of electric quantities. Figure 2.17 (a) is the current stream function in the channel with the contour of 20 A, (b) shows the eddy current at both end regions with the contour of 2 A and (c) is the electrical potential. A rather large x-component of current can be seen in Figure 2.17, which results from a large leakage current on the cathode wall as shown in Figure 2.19.

Figure 2.18 compares the distribution of electrode currents (Faraday current) along the channel between the experiment and the computation. Both values approximately agree with each other where the computational value is larger than the experimental value in the 35th through the 60th electrodes. This is because a

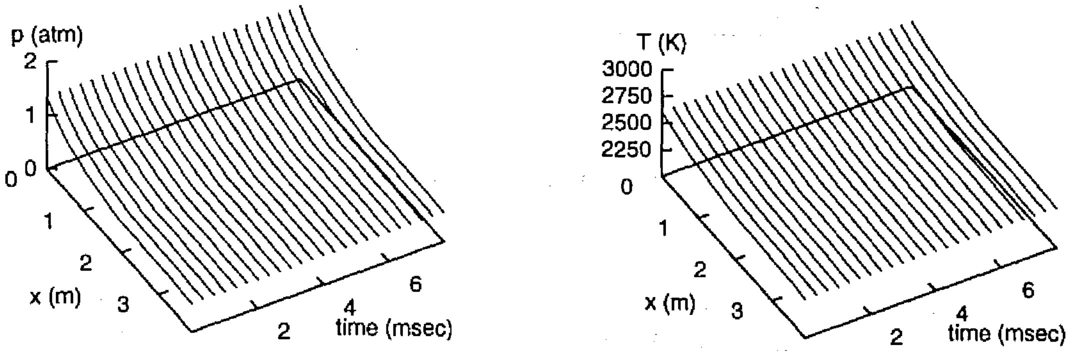

(a) Pressure

(b) Temperature

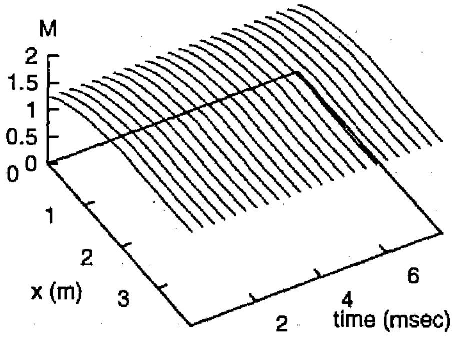

(c) Mach number

Figure 2.16: Distributions of flow field at the condition of power output of 98.2 kW

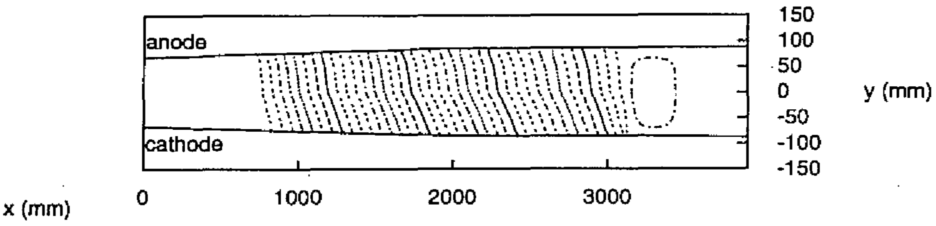

(a) Current stream lines

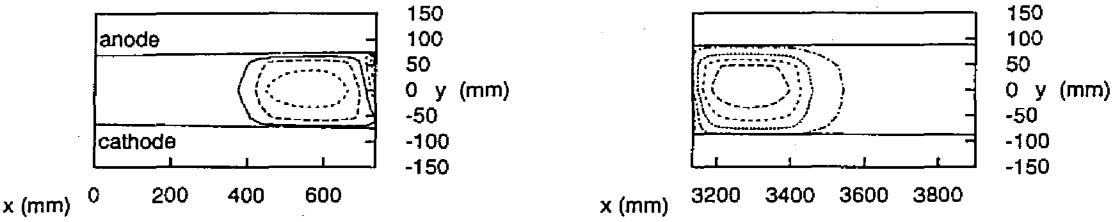

(b) Current stream lines

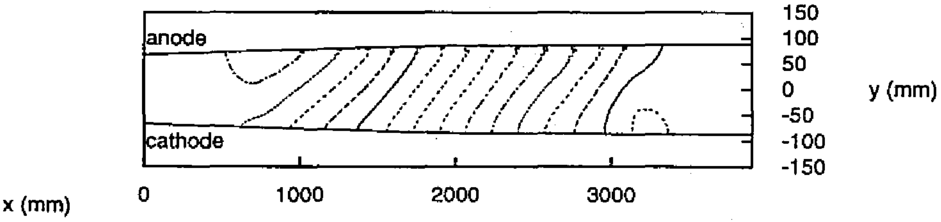

(c) Equi-potential lines

Figure 2.17: Two-dimensional distributions of electric quantities at the condition of power output of 98.2 kW: (a) current stream-function (contour of 20 A); (b) eddy current at end regions (contour of 2 A); (c) potential (contour of 100 V)

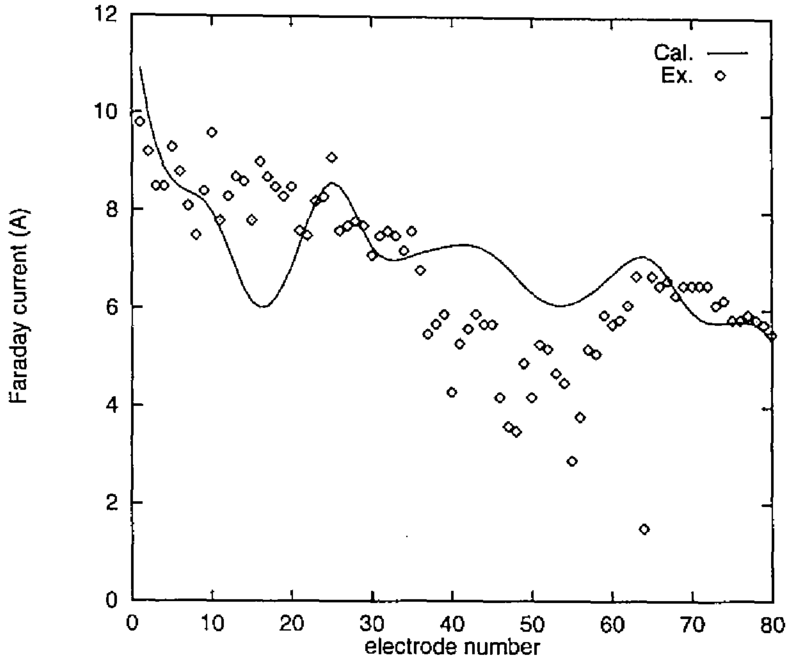

Figure 2.18: Comparison of electrode currents at the condition of power output of 98.2 kW

large local leakage in the y-direction exists in this region, which is suggested by the open-circuit run mentioned later.

Figure 2.19 depicts the distribution of leakage currents along the walls. Figure 2.19 shows that a rather large leakage current exists along the cathode wall in the x-direction while leakage current along the anode wall is very small. About 60 A is shown at the mid part of the channel, which is about eight times that of the electrode current.

The dependency of power output on load resistance is calculated, as is shown in Figure 2.20, where the relative load resistance to the experimental value is a parameter. Figure 2.20 indicates that power output can be improved a little by controlling the load resistance.

The open-circuit voltage was also measured in a separate run. This run showed a strange voltage distribution along the channel which was probably induced by the strong local leakage in the y-direction. Then, the distribution of effective leakage resistance in the y-direction was estimated, which leads to 300 Ω of leakage resistance in the y-direction with almost zero effective resistance at the mid point of the channel and also at the 55th electrode. The value of 300 Ω of leakage resistance in the y-direction is larger than that of about 80 Ω which had been estimated in

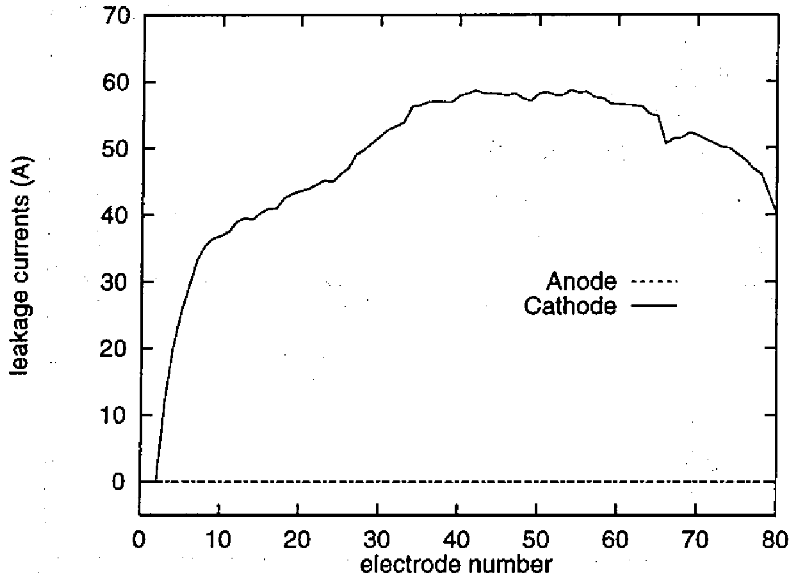

Figure 2.19: Distribution of leakage currents along anode and cathode walls

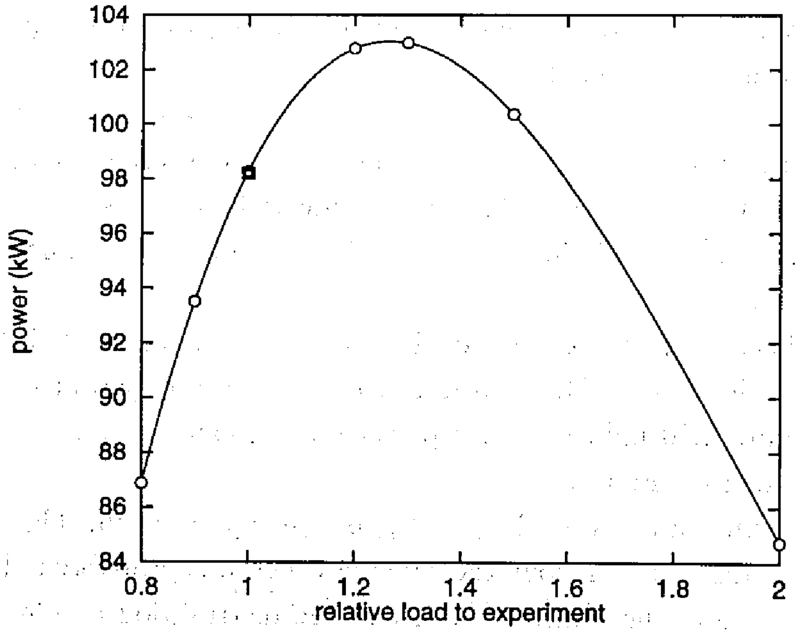

Figure 2.20: The dependency of power output on relative load resistance (Square shows the experimental data)

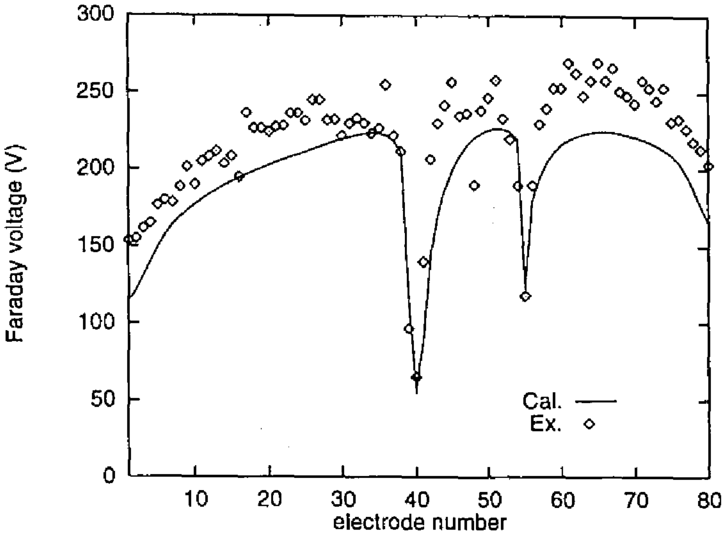

Figure 2.21: Comparison of distribution of open-circuit voltage

Subsection 2.5.1, but the estimation in Subsection 2.5.1 does not include the effect of local shortings. Figure 2.21 plots the distribution of the open-circuit voltage obtained by the analysis taking into account local shortings. Figure 2.21 indicates good agreement of the computational result with the experimental one although the experimental values are generally a little larger than the calculation result.

2.5.4 Analysis of Experiment Performed in April 1994

The power output of 80.3 kW was rather low. This is mainly because the quality of coal was low, leading to low electrical conductivity. In this experiment, the thermal input was not reported, and thus, the design condition is used as the initial condition for the time-dependent calculation. The calculation results in 90.2 kW with the three basic parameters. Then, the effective electrical conductivity is changed to match the experiment, resulting in 53 % of the theoretical value which gives 83.1 kW, being close to the experimental output of 80.3 kW.

2.5.5 Analysis of Experiment Performed in November 1994

The power run in November, 1994 yielded 119.7 kW. The MHD channel was modified where ceramics capped elements were used for the side-walls of first half of the channel [18]. An experiment with the open-circuit condition showed that only a small Hall field was induced at the first half of the channel, indicating that the leakage current along the y-direction was reduced in the first half of the channel.

In the power run of November, 1994, the values of the load resistances are reported in Ref. 18). Thus, these values are used in the present analysis. Figure 2.22 shows the distribution of the load resistances. The assumed leakage resistance in the y-direction is modified according to the modification of channel wall itself. The numerical calculation is carried out with 300 Ω of effective leakage resistance in the y-direction for the first half channel, with 2 Ω at the center of channel where the first and second channels are linked with a metal frame, and with 80 Ω for the second half channel. As shown below, these parameters can give relatively good agreement with the experimental result, indicating that the leakage in the y-direction is improved several times at the first half of the channel compared with the old channel. The effective electrical conductivity is estimated to be one quarter of the theoretical value in order to reproduce the power output obtained from the experiment. This means that the estimated stagnation temperature is too high or the mixing of seed is very poor.

The power output calculated is 120.0 kW, which is almost the same as the experimental result of 119.7 kW.

Figure 2.23 depicts the potential distribution along the channel, where the top and bottom lines show potentials along the cathode and anode walls, respectively.

Figure 2.24 shows the Faraday current distribution along the channel. Figures 2.25 (a), (b) and (c) depict two-dimensional distributions of electric quantities. Figure 2.25 (a) is the current stream function in the channel with the contour of 20 A, (b) shows the eddy current at both end regions with the contour of 2 A and (c) is the electrical potential. The total loading current is 846 A, whereas the experiment resulted in 814 A, indicating good agreement between the computation and the experiment. Figures 2.23 and 2.25(c), however, indicate that the Hall potential obtained by the analysis is 1537 V although the experimental result is 565 V. The calculation yields a value that is about 2.7 times higher than the experiment. This disagreement is investigated in the next subsection.

Figures 2.26 depict distributions of various quantities in the channel operated in November 1994. The flow field becomes different between the first and the second half of the channel. In the first half of the channel the flow is accelerated and the pressure decreases sharply, on the other hand, the flow is slightly decelerated and the pressure and the temperature is kept almost constant along the second half of the channel. Within the active channel, the electrical conductivity is rather low, being less than 4 S/m to less than 3 S/m while the Hall parameter is less than 1.8.

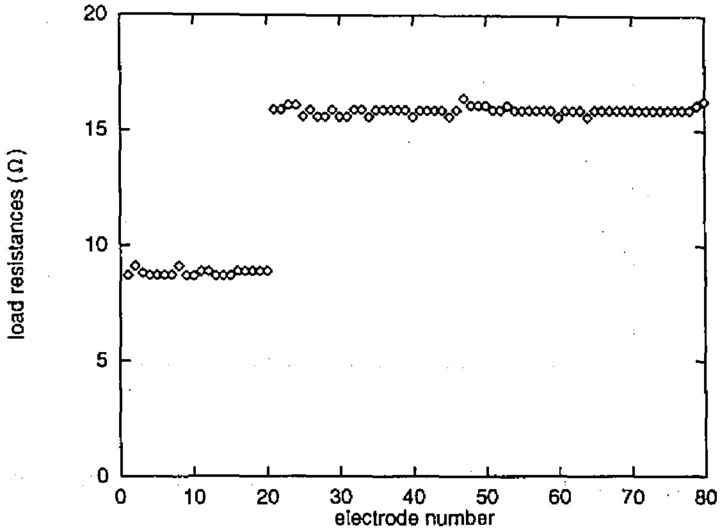

Figure 2.22: Reported load resistances on power run at November 1994

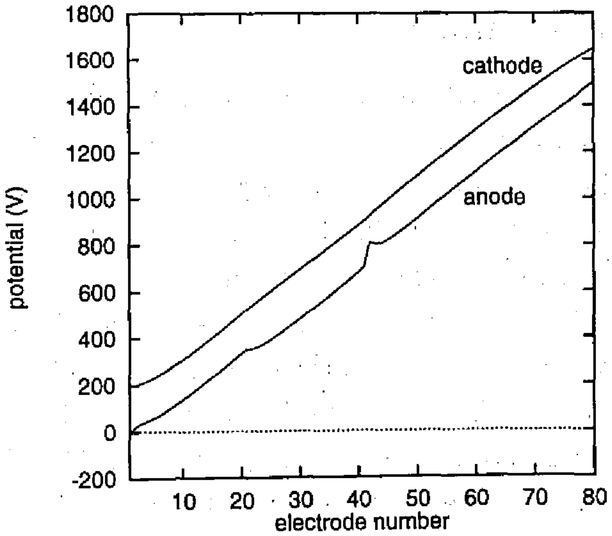

Figure 2.23: Potential distribution along channel (Power run at November 1994)

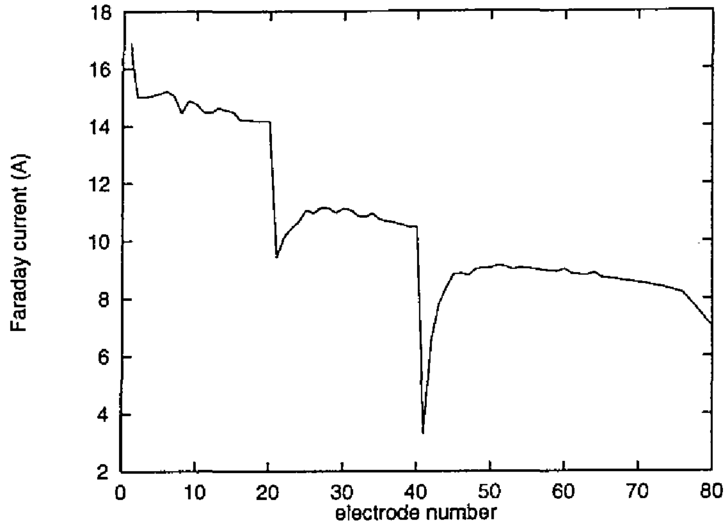

Figure 2.24: Faraday current distribution along channel (power run at November 1994)

The maximum value of current density in the y-direction (J_y) is about 3.2 A/cm^2 and abnormal behavior is seen at the center along the channel which is shorted by the metal frame.

2.5.6 Effects of the External x-direction Leakage (Power Run at November 1994)

In the above analysis performed for power run at November 1994, the calculated potential distribution does not agree with the experiment. This is possibly caused by the external leakage in the x-direction as is suggested in Ref. 19). This subsection then examines the external leakage in the x-direction which is shown in Figure 2.27. The internal leakage resistance in the x-direction, R_x, is determined to be 0.18 Ω. The external leakage resistance in the x-direction is 6.5 Ω, the effective electrical conductivity is one third of its theoretical value. The y-direction leakage resistances are selected to be the same as in the foregoing analysis. Figure 2.28 plots the potential distribution, showing that the Hall voltage is 582 V which agrees well with the experimental value. The power output is 117 kW and the total load current is 835 A, which also agree well with the experimental values.

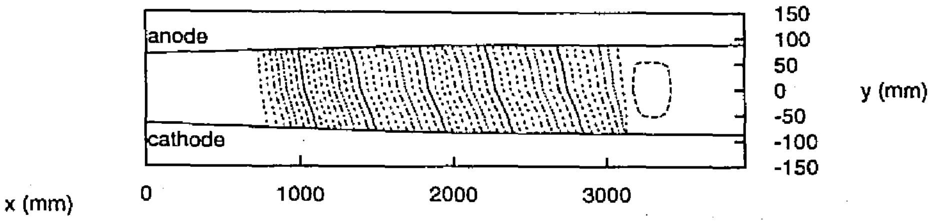

(a) Current stream lines

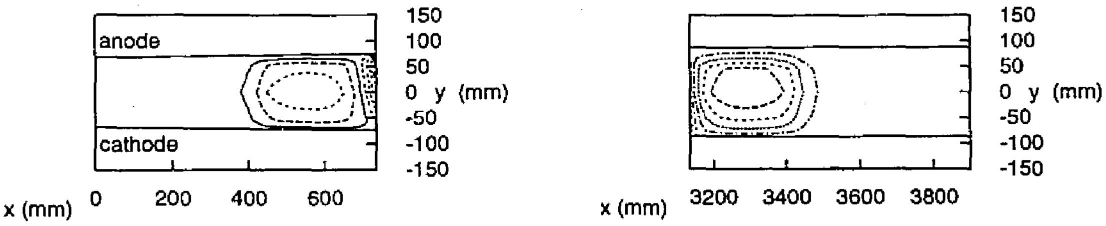

(b) Current stream lines

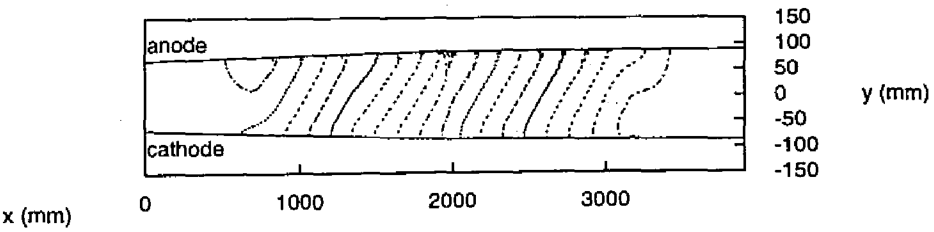

(c) Equi-potential lines

Figure 2.25: Two-dimensional distributions of electric quantities at the condition of power output of 120 kW:(a) current stream function(contour of 20 A); (b) eddy current at end regions (contour of 2 A); (c) potential (contour of 100 V)

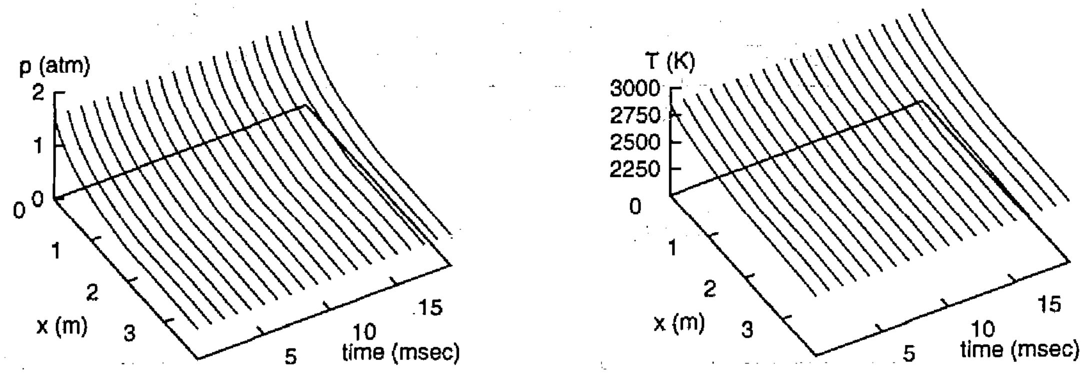

(a) Pressure

(b) Temperature

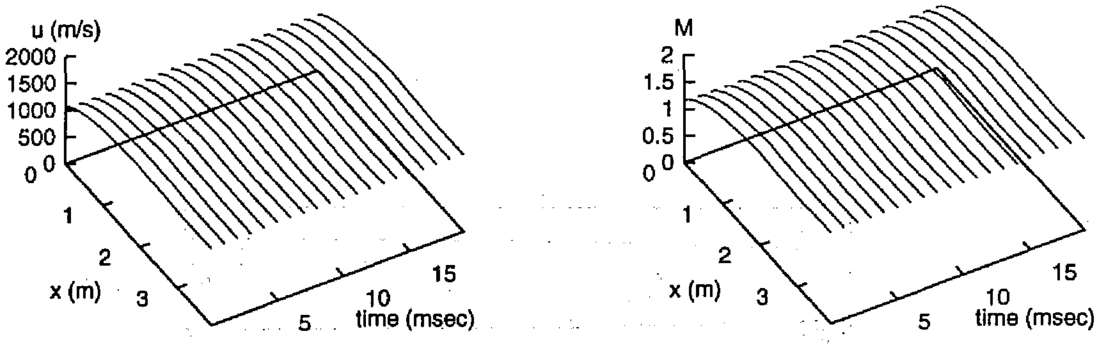

(c) Flow velocity

(d) Mach number

Figure 2.26: Distributions of various quantities in the channel operated in November 1994

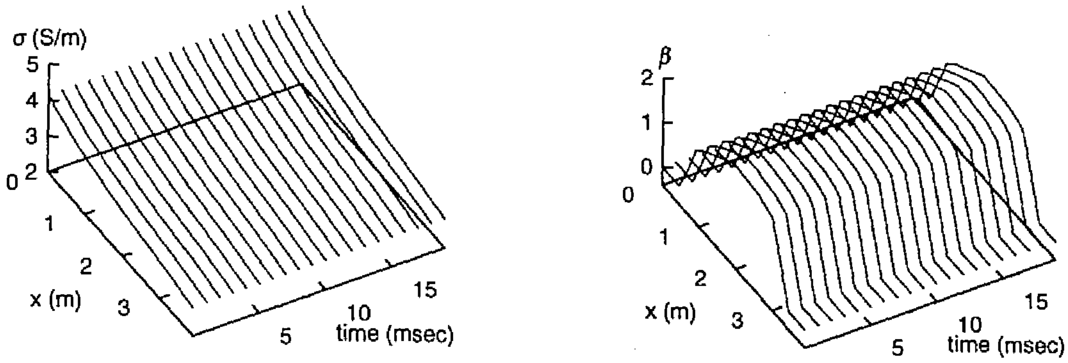

(e) Electrical conductivity

(f) Hall parameter

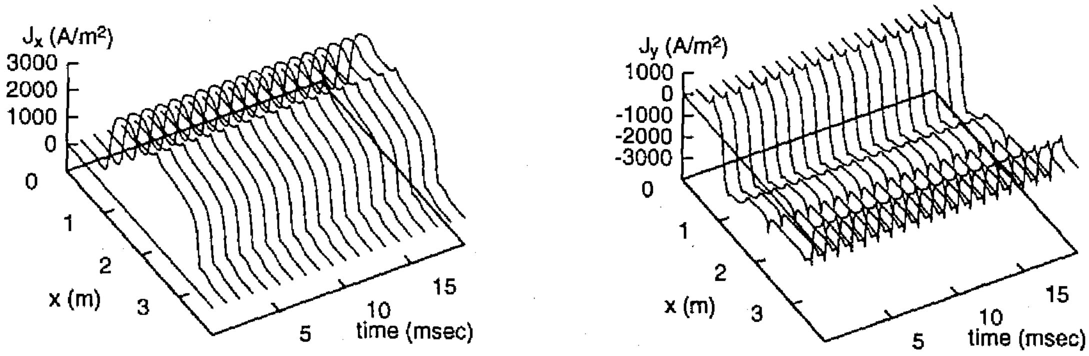

(g) Current density in x-direction

(h) Current density in y-direction

Figure 2.26: Distributions of various quantities in the channel operated in November 1994

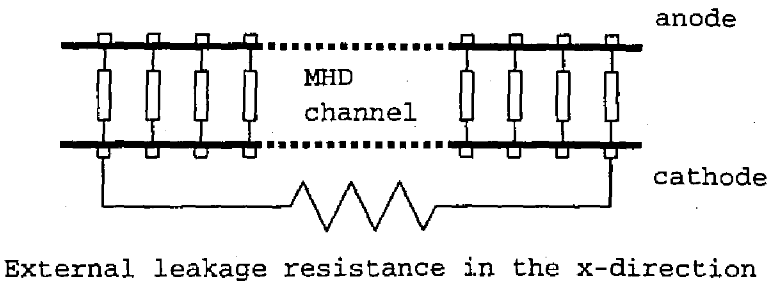

Figure 2.27: External leakage in the x-direction

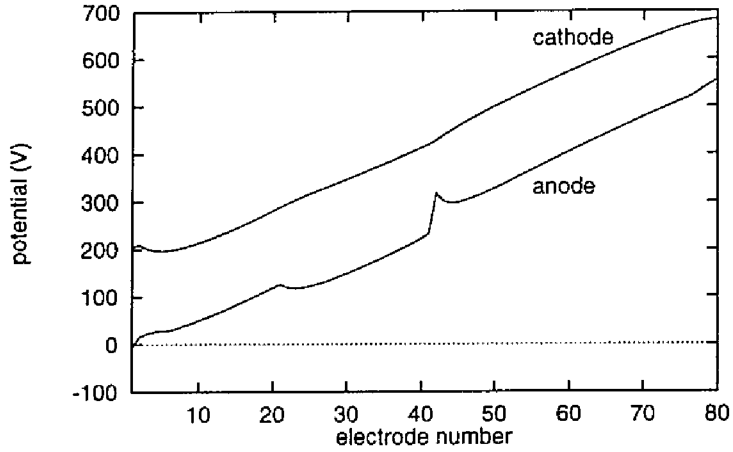

Figure 2.28: Potential distribution along channel of power run at November 1994 considering external leakage in x-direction

2.6 Prediction of Performance of Diagonal Mode Operation

So far all experiments have been carried out with the Faraday mode. However, it is also important to examine performance of the MHD channel with the diagonal mode. A numerical analysis is, therefore, carried out for the diagonal operation before experiments. In the analysis, the inlet boundary condition, the effective electrical conductivity and leakage resistances are assumed to be the same as those of the power run of October, 1993.

2.6.1 Independent Five Loads of Diagonal Operation

The diagonal overlap is assumed to be 6 which results in the diagonal angle of 43.0° at the channel inlet and 53.1° at the channel exit. Figure 2.29 shows the schematic diagram of the generator with independent five loads of diagonal operation. After a rough optimization the values of five loads are selected as 150, 95, 75, 75 and 75 Ω from upstream to downstream. The calculation results in the power output of 104.7 kW, a little larger than the experimental result of the Faraday mode operation (98.2 kW), when the loads are not consolidated, being with the five independent loads.

Figure 2.30 plots the potential distribution along the diagonal channel with the independent five loads, where the top and bottom lines show potentials along the cathode wall and the anode wall, respectively. The Hall potential (the load voltage)

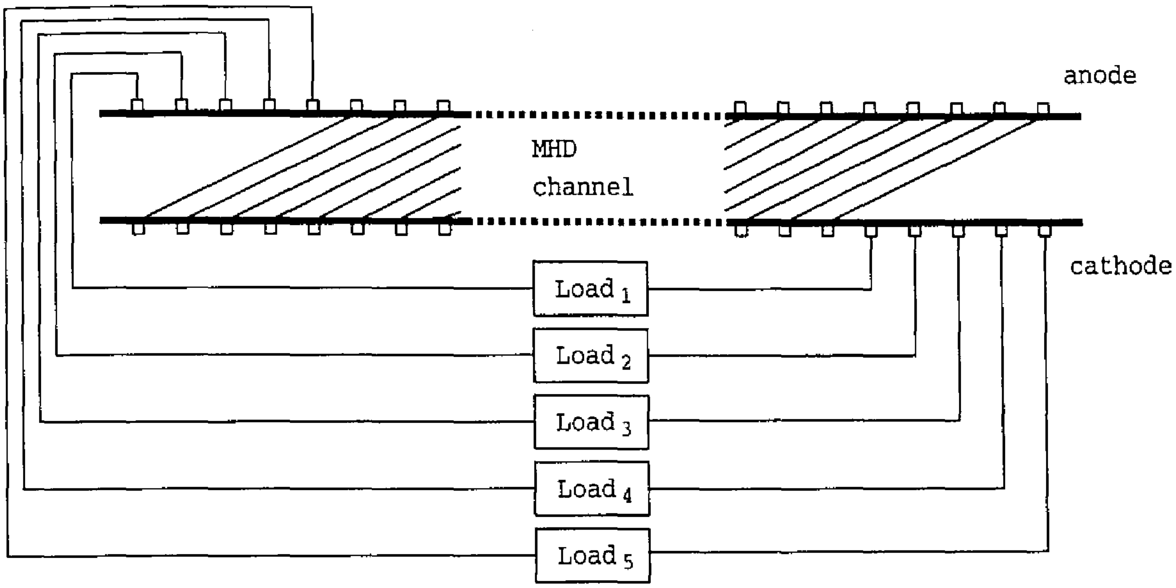

Figure 2.29: Generator with independent five loads of diagonal operation

is about 1.22 kV and the total load current is about 86 A.

Figures 2.31 show the two-dimensional distributions of electric quantities. The total Faraday current is 870 A, which is about 5 % higher than the Faraday channel.

2.6.2 Consolidated Single Load of Diagonal Operation

The diagonal overlap is also assumed to be 6 and the five loads are consolidated with ballast resistances and diodes as shown in Figure 2.32. After a rough optimization the value of single load is selected as 20 Ω. A power output of 98 kW is obtained, which is identical to the experimental result of the Faraday mode operation. The Hall potential (the load voltage) is about 1.4 kV and the load current is about 70 A, while the open voltage is about 2600 V and the short current is about 158 A, as shown in Figure 2.33, which depicts the voltage-current characteristics. The curve of voltage-current characteristics is linear and therefore the MHD interaction within the present channel is still low.

Figure 2.34 depicts the potential distribution along the diagonal channel with the consolidated single load, the top and bottom lines show potentials along the cathode and anode walls, respectively, showing that the Hall potential is slightly higher when the load is consolidated than when loads are independent.

Figures 2.35 plot distributions of various quantities in diagonal channel with consolidated single load, showing that the basic feature of the flow field is almost

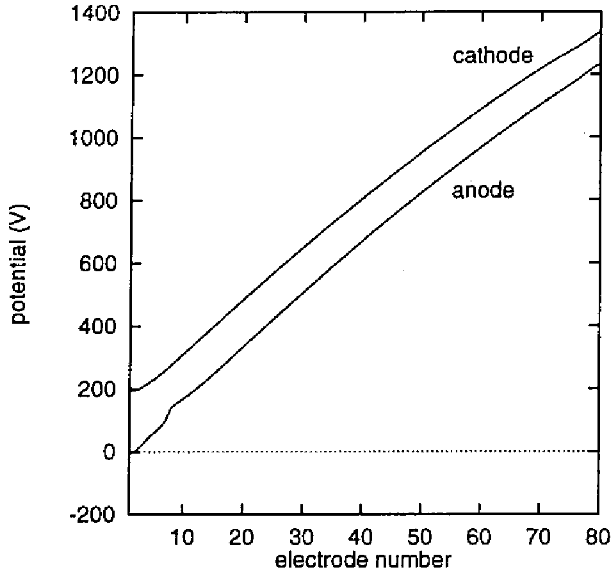

Figure 2.30: Potential distribution along diagonal channel with independent five loads

the same as the flow field of the Faraday channel. In the first half of the channel the flow is accelerated and the flow remains unchanged along the second half of the channel. A rather large x-component of current density is induced in the entire channel, indicating that the present channel has a rather large leakage current along the flow direction probably due to the slag layers on the cathode wall.

2.7 Hidden Capability of the Facility

Here, we will check the capability of the present MHD facility by changing the basic parameters. At first, the effective electrical conductivity is assumed as the theoretical value, while the other two parameters are the same, and the inlet condition and the thermodynamic properties are assumed to be the designed values. The power output obtained is, thus, 437.8 kW, which is about four times that of the experiment. The computation shows that the increase of electrical conductivity is very important to increase the power output. This probably can be realized by the complete combustion of coal or by the better mixing of seed.

Next, the leakage resistance in the x-direction is assumed to be 10.0 Ω with the same values for the other parameters, resulting in a power output of 406.2 kW. This can be realized by the improvement of insulation between cathodes. It is

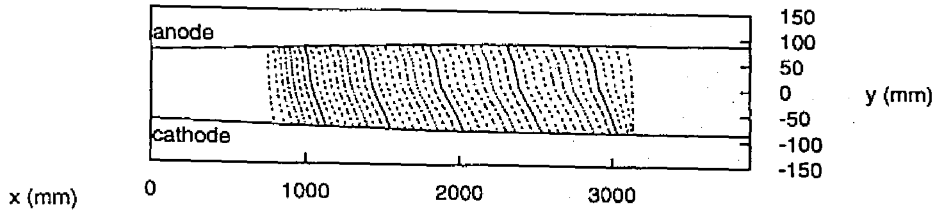

(a) Current stream lines

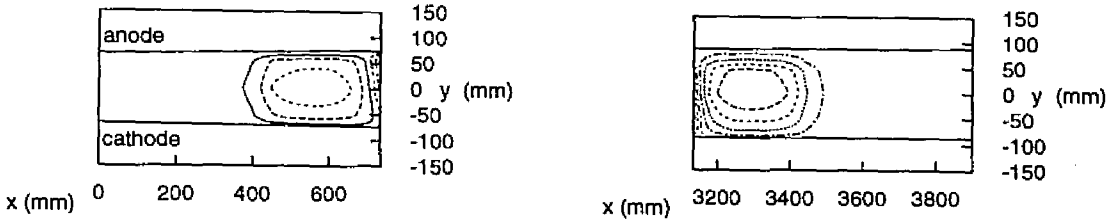

(b) Current stream lines

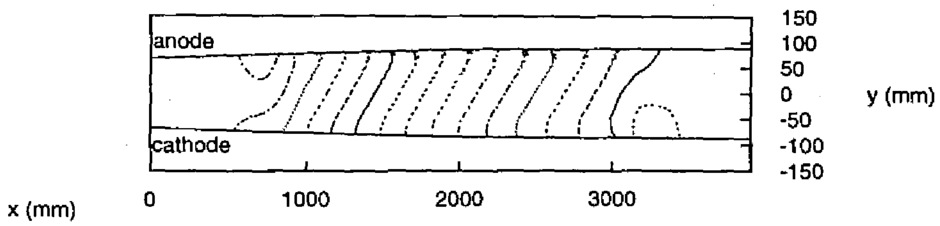

(c) Equi-potential lines

Figure 2.31: Two-dimensional distributions of electric quantities in diagonal channel with independent five loads:(a) current stream function (contour of 20 A); (b) eddy current at end regions (contour of 2 A); (c) potential (contour of 100 V)

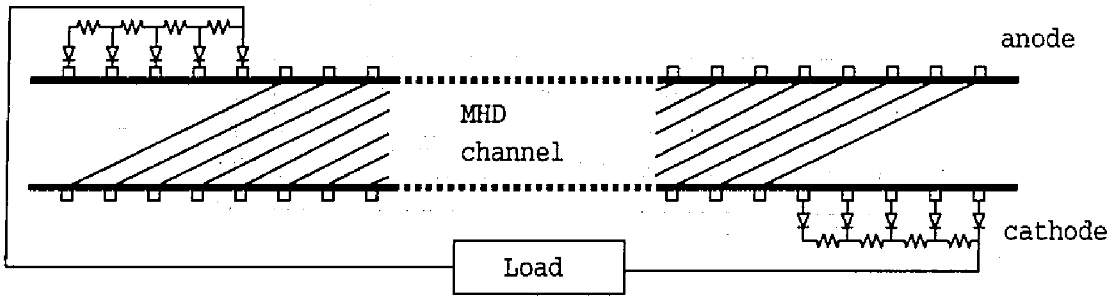

Figure 2.32: Generator with single load consolidated by ballast resistances and diodes

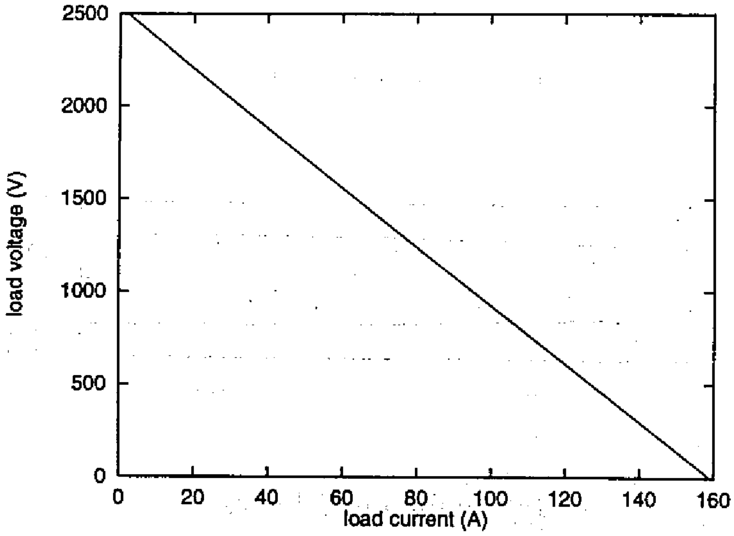

Figure 2.33: Voltage-current characteristics of diagonal channel with consolidated single load

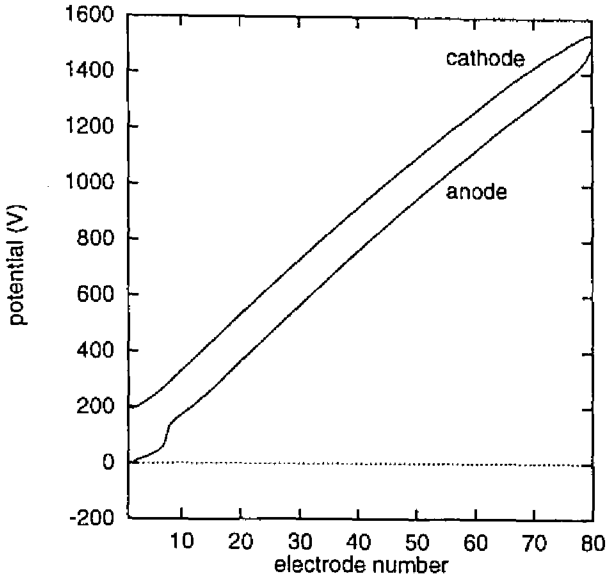

Figure 2.34: Potential distribution along diagonal channel with consolidated single load

however difficult to realize a better insulation between cathodes when the channel is operated with the low temperature walls which are covered with molten slag of coal.

Next, the leakage resistance in the y-direction is assumed to be 1000 Ω, while the other parameters have the same values, leading to a power output of 302.9 kW, about three times that of the experiment. This probably can be realized where the real cause of the leakage in the y-direction is revealed.

Finally, it is assumed that the effective conductivity is the theoretical value, the leakage resistance in the x-direction is 10.0 Ω, the leakage resistance in the y-direction is 1000 Ω. The obtained power output reaches 548.2 kW which is about five times that of the experiment. This is the real capability of the facility, which is hidden in the present situation.

2.8 Concluding Remarks

The Chinese 25 MWth Faraday type MHD generator is analyzed in this chapter. The followings are summaries of the results of the analysis.

- The three key parameters of electrical behavior of the MHD Faraday channel at IEE, China are evaluated with the experimental data of 1992 and 1993. The

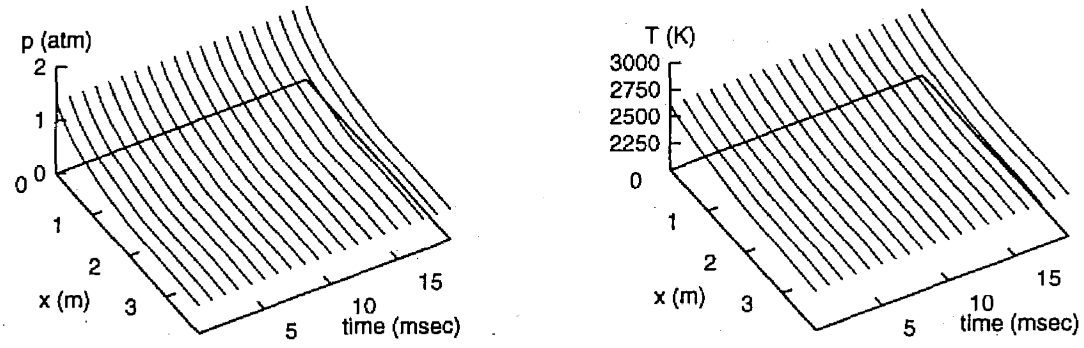

(a) Pressure

(b) Temperature

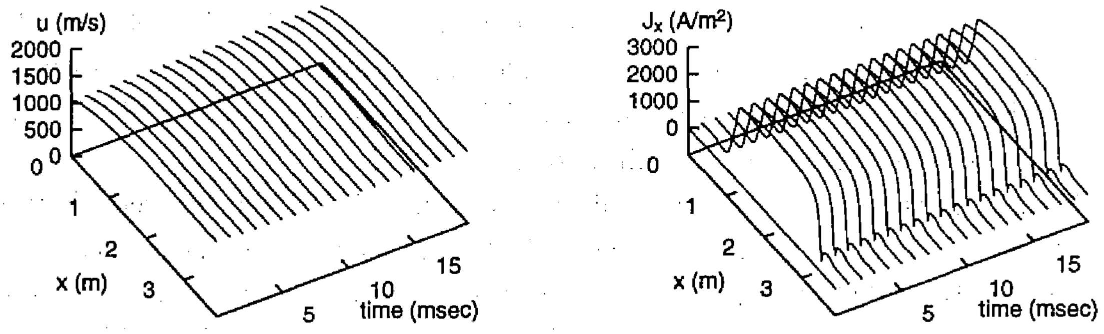

(c) Flow velocity

(d) Current density in x-direction

Figure 2.35: Distributions of various quantities in diagonal channel with consolidated single load

effective electrical conductivity is 5/9 times that of the theoretical value, the leakage resistance in the x-direction is 0.024 Ω and the leakage resistance in the y-direction is 82.4 Ω, which can give very close values to the experimental results. The power output is 98.3 kW in the calculation, whereas 98.2 kW was obtained in the experiment for the power run performed in August, 1993.

- Experimental data obtained in November, 1994 is analyzed to examine the effect of the modification of the channel, showing that the implemented improvement was effective in reducing the leakage current in the y-direction and resulted in the maximum power output (about 120 kW).
- The diagonal operation is estimated. The analysis shows that the diagonal operation can produce almost the same power output as the Faraday operation can (98 kW). The load current is about 70 A with the load voltage of 1400 V.
- The hidden capability of the Chinese channel is evaluated, and the effects of electrical conductivity are found to be large. If the theoretical value can be obtained, the obtained power output becomes over 400 kW.
- These analyses validate the mathematical models adopted in the present thesis.

Chapter 3 Stability Analysis of Supersonic Diagonal-Type MHD Generator of Commercial-Scale

3.1 Introduction

The stability of supersonic diagonal type MHD generator of commercial-scale is studied in this chapter.

In preliminary analyses of commercial-scale MHD power system, Y. Fujita found the possibility of unstable behavior of large-scale diagonal type MHD generators21). Using a local linear perturbation analysis, M. Ishikawa and A. Kyogoku showed that the instability is caused by the growth of magneto-acoustic waves 26). This analysis, however, assumed constant current loads and did not examine the effect of the loading condition on the stability of the MHD generator. On the other hand, T. Matsuo et al. carried out stability analysis for large-scale supersonic disk type MHD generators and showed that the loading condition, i.e., the electrical boundary condition, greatly, affects the stability of the generator 31). The stability analysis for the disk type generator suggests that the diagonal type generator is expected to be stabilized by the control of electrical behavior in the generator through its many electrode pairs.

In this chapter, the author, therefore, performs linear stability analyses and time-dependent calculations in order to examine effects of the electrical boundary condition.

In the supersonic flow, disturbances of flow go out of the channel in finite time, since the supersonic flow has no upstream acoustic waves and disturbances do not propagate upstream. When the disturbance is magnified, so large as to induce a shock wave during its propagation, the generator becomes unstable. Then the author evaluates the spatial growth rate of flow disturbances by a sensitivity analysis31), and examines what kinds of the loading condition or the diagonal-link circuit can suppress the growth of flow disturbance.

On the other hand, since load current disturbances circulate through the load circuit and the channel, the generator becomes unstable if their time growth rate is positive. Then the time growth rate of the load current disturbance is evaluated by a linear stability analysis 31). The analysis examines what kinds of loading condition suppress the growth of the load current disturbance.

Time-dependent calculations are also performed for confirming results of the linear analysis and for examining the stability when large disturbance, which the linear analysis cannot treat, comes into the generator.

3.2 Basic Equations

3.2.1 Basic Equations for Gasdynamics

The basic equations used for the gasdynamical part are given under a one-dimensional approximation as:

$$\partial \boldsymbol{U}/\partial t + \partial \boldsymbol{F}(\boldsymbol{U})/\partial x = \boldsymbol{S}(\boldsymbol{U}) \tag{3.1}$$

$$\boldsymbol{U} = \begin{pmatrix} U_1 \\ U_2 \\ U_3 \end{pmatrix} = \begin{pmatrix} \rho A \\ \rho u A \\ \rho(\varepsilon + u^2/2)A \end{pmatrix} \tag{3.2}$$

$$\boldsymbol{F}(\boldsymbol{U}) = \begin{pmatrix} \rho u A \\ (\rho u^2 + p)A \\ \rho u(\varepsilon + \frac{p}{\rho} + u^2/2)A \end{pmatrix} \tag{3.3}$$

$$\boldsymbol{S}(\boldsymbol{U}, I) = \begin{pmatrix} 0 \\ p\mathrm{d}A/\mathrm{d}x + AJ_yB - f_{ric} \\ (\boldsymbol{J}\cdot\boldsymbol{E})A - q_{loss} \end{pmatrix} \tag{3.4}$$

where I is the load current.

The state equations of working gas are written as

$$\rho = \rho(p, T), \quad \varepsilon = \varepsilon(p, T). \tag{3.5}$$

By dropping the time derivatives, the steady state form of Equation (3.1) is obtained:

$$\frac{\mathrm{d}\boldsymbol{U}(x)}{\mathrm{d}x} = (\frac{\partial \boldsymbol{F}(\boldsymbol{U}, A)}{\partial \boldsymbol{U}})^{-1}[\boldsymbol{S}(\boldsymbol{U}, x) - \frac{\partial \boldsymbol{F}(\boldsymbol{U}, A)}{\partial A}\frac{\mathrm{d}A}{\mathrm{d}x}]. \tag{3.6}$$

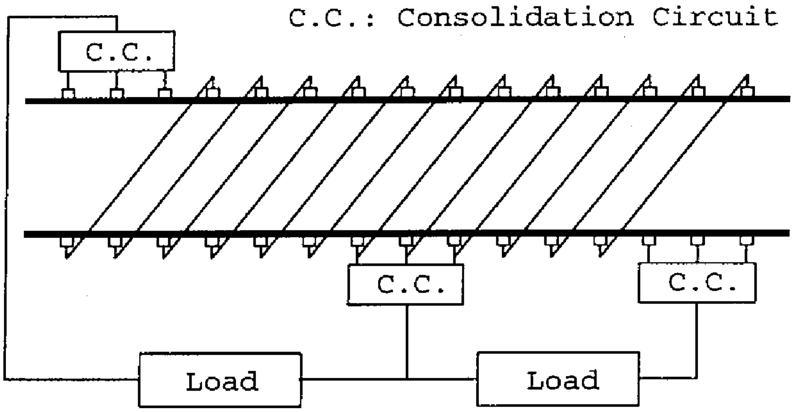

Figure 3.1: Diagonal type MHD generator

3.2.2 Relations for Electrodynamics

The relation between the electric field and the electric current density is given by the steady Maxwell equations (2.6) and (2.7), and by the generalized Ohm's law (2.9).

In this chapter, the diagonal type MHD generator shown in Figure 3.1 is analyzed with quasi-one-dimensional approximation. From Equation (2.9), the generalized Ohm's law is reduced to Equations (3.7) and (3.8) under quasi-one-dimensional approximation.

$$J_x + \beta J_y = \sigma E_x \tag{3.7}$$

$$-\beta J_x + J_y = \sigma(E_y - uB + \frac{\Delta V}{h_{chl}}) \tag{3.8}$$

where h_{chl} is the channel hight, ΔV the electrode voltage drop (see Appendix A).

The continuity equation of electric current for the diagonal type MHD generator is derived from Equation (2.6):

$$(J_x - J_y \cot\theta_d)A = I - \frac{E_x}{R_{leak}} w_{chl} \tag{3.9}$$

where w_{chl} is the channel width, θ_d the diagonal angle and R_{leak} the leak resistance ratio at the channel wall.

Figure 3.2 depicts the schema of diagonal connection. When diagonal links are short-circuited, Equation (2.7) leads to

$$E_y = -E_x \cot\theta_d. \tag{3.10}$$

When the link is connected with an inductor, the equation for the diagonal-link circuit can be written as

$$L_{link}\frac{\mathrm{d}I_{link}}{\mathrm{d}t} = (E_x \cot\theta_d + E_y)h_{chl} \tag{3.11}$$

where $I_{link} = -J_y w_{chl}\Delta x$ is the current of the diagonal link, Δx the electrode pitch and L_{link} the inductance of the link.

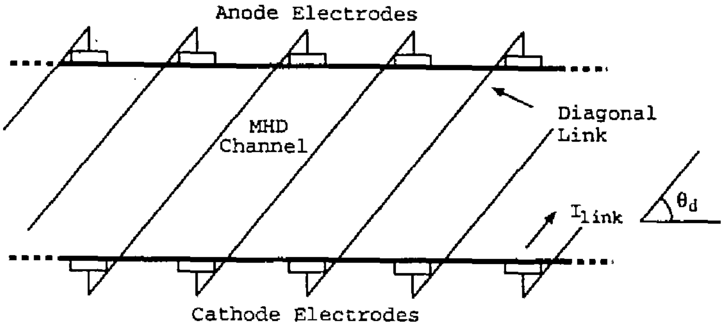

Figure 3.2: Diagonal connection

3.2.3 Behavior of Perturbations

In order to analyze the stability of the generator, the present thesis examines the behavior of the perturbations added to the steady-state flow given by Equation (3.6). The perturbations of $\boldsymbol{U}$ and I are assumed to be given as

$$\boldsymbol{U} \to \boldsymbol{U} + \delta\boldsymbol{U}(x)\exp(st), \quad I \to I + \delta I\exp(st) \tag{3.12}$$

where s is the time growth rate of perturbations. From Equations (3.1) and (3.12), the equation which describes the propagation of perturbations is obtained:

$$\frac{\partial\boldsymbol{F}}{\partial\boldsymbol{U}}\frac{\mathrm{d}\delta\boldsymbol{U}(x)}{\mathrm{d}x} = (\frac{\partial\boldsymbol{S}}{\partial\boldsymbol{U}} - s\mathbf{1} - \frac{\mathrm{d}\boldsymbol{U}}{\mathrm{d}x}\frac{\partial^2\boldsymbol{F}}{\partial\boldsymbol{U}^2} - \frac{\mathrm{d}A}{\mathrm{d}x}\frac{\partial^2\boldsymbol{F}}{\partial A\partial\boldsymbol{U}})\delta\boldsymbol{U}(x) + \frac{\partial\boldsymbol{S}}{\partial I}\delta I \tag{3.13}$$

where $\mathbf{1}$ is the 3×3 unit matrix and

$$\frac{\mathrm{d}\boldsymbol{U}}{\mathrm{d}x}\frac{\partial^2\boldsymbol{F}}{\partial\boldsymbol{U}^2} = \sum_{i=1}^{3}\frac{\mathrm{d}U_i}{\mathrm{d}x}\frac{\partial^2\boldsymbol{F}}{\partial U_i\partial\boldsymbol{U}}. \tag{3.14}$$

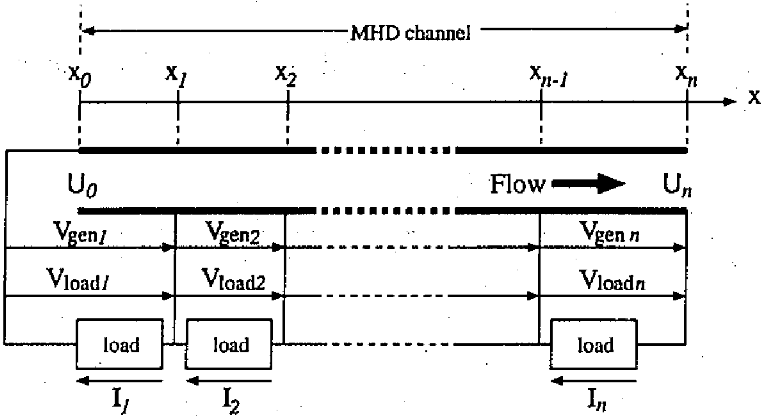

Figure 3.3: Loading scheme of multi-loaded MHD channel

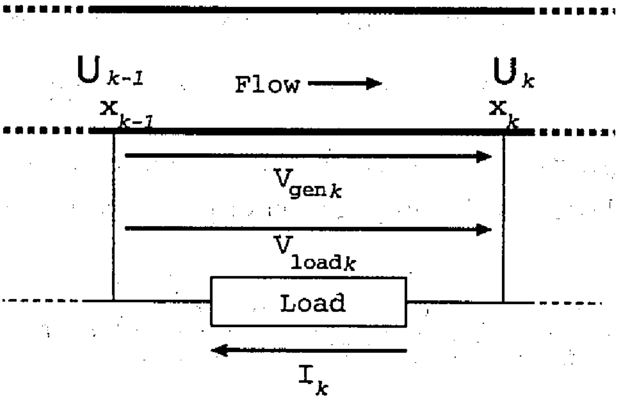

Figure 3.4: k-th loading section

3.3 Method of Analyses

3.3.1 Loading Condition

The MHD channel is divided into n loading sections $[x_{k-1}, x_k](k = 1, 2, \cdots, n)$ as is shown in Figure 3.3, where the load circuit is constituted with the direct-coupling scheme. The generator voltage, the load current and the load voltage of the k-th loading section are denoted by $V_{\text{gen}k}$, I_k and $V_{\text{load}k}$, respectively, as is shown in Figure 3.4. The gasdynamical variable vector $\boldsymbol{U}$ at $x = x_k$ is denoted by $\boldsymbol{U}_k$.

The integration of Equation (3.6) from $x = x_{k-1}$ with the initial value $\boldsymbol{U}(x_{k-1}) = \boldsymbol{U}_{k-1}$ gives $\boldsymbol{U}(x)(x_{k-1} \leq x \leq x_k)$ in the steady state, which is written as a function of $\boldsymbol{U}_{k-1}$ and I_k:

$$\boldsymbol{U}(x) = \boldsymbol{U}(x, \boldsymbol{U}_{k-1}, I_k). \tag{3.15}$$

The generator voltage $V_{\text{gen}k}$ depends on the gasdynamical variables $\boldsymbol{U}$ and on the load current I_k:

$$V_{\text{gen}k} = -\int_{x_{k-1}}^{x_k} E_x(\boldsymbol{U}, I_k)dx. \tag{3.16}$$

From Equations (3.15) and (3.16), $V_{\text{gen}k}$ in the steady state is written as a function of $\boldsymbol{U}_{k-1}$ and I_k:

$$V_{\text{gen}k} = V_{\text{gen}k}(\boldsymbol{U}_{k-1}, I_k). \tag{3.17}$$

On the other hand, the load voltage $V_{\text{load}k}$ depends on the characteristics of the load circuit, which is given as a function of the load current I_k:

$$V_{\text{load}k} = V_{\text{load}k}(I_k). \tag{3.18}$$

Then, the loading condition for the k-th loading section is given by

$$V_{\text{gen}k}(\boldsymbol{U}_{k-1}, I_k) - V_{\text{load}k}(I_k) = 0. \tag{3.19}$$

3.3.2 Method of Sensitivity Analysis

A sensitivity analysis examines the spatial growth rate of perturbations. The growth rate of perturbations during propagation along the k-th loading section is given by the eigenvalues of the matrix $\partial \boldsymbol{U}_k / \partial \boldsymbol{U}_{k-1}$. This matrix means the rate of the variation of exit flow $\boldsymbol{U}_k$ due to the variation of inlet flow $\boldsymbol{U}_{k-1}$.

The growth rate of perturbations during propagation along the whole channel is given by the eigenvalues of the matrix $\partial \boldsymbol{U}_n / \partial \boldsymbol{U}_0$. By using $\partial \boldsymbol{U}_k / \partial \boldsymbol{U}_{k-1}$, the sensitivity matrix $\partial \boldsymbol{U}_n / \partial \boldsymbol{U}_0$ is written as

$$\frac{\partial \boldsymbol{U}_n}{\partial \boldsymbol{U}_0} = \frac{\partial \boldsymbol{U}_n}{\partial \boldsymbol{U}_{n-1}} \frac{\partial \boldsymbol{U}_{n-1}}{\partial \boldsymbol{U}_{n-2}} \cdots \frac{\partial \boldsymbol{U}_1}{\partial \boldsymbol{U}_0}. \tag{3.20}$$

The matrix $\partial \boldsymbol{U}_k / \partial \boldsymbol{U}_{k-1}$ is calculated as in the following subsections.

3.3.2.1 Variational equations

From Equation (3.13), the variational equation of Equation (3.1) in $[x_{k-1}, x_k]$ with respect to $\boldsymbol{U}_{k-1}$ is obtained:

$$\frac{\mathrm{d}}{\mathrm{d}x} \frac{\partial \boldsymbol{U}(x)}{\partial \boldsymbol{U}_{k-1}} = (\frac{\partial \boldsymbol{F}}{\partial \boldsymbol{U}})^{-1} (\frac{\partial \boldsymbol{S}}{\partial \boldsymbol{U}} - s\mathbf{1} - \frac{\mathrm{d}\boldsymbol{U}}{\mathrm{d}x} \frac{\partial^2 \boldsymbol{F}}{\partial \boldsymbol{U}^2} - \frac{\mathrm{d}A}{\mathrm{d}x} \frac{\partial^2 \boldsymbol{F}}{\partial A \partial \boldsymbol{U}}) \frac{\partial \boldsymbol{U}(x)}{\boldsymbol{U}_{k-1}} \tag{3.21}$$

where the matrix $\partial \boldsymbol{U}(x) / \partial \boldsymbol{U}_{k-1}$ represents the rate of the variation of $\boldsymbol{U}(x)$ due to the variation of $\boldsymbol{U}_{k-1}$ when I_k is fixed.

The variational equation of Equation (3.1) in the k-th loading section with respect to I_k is also derived from Equation (3.13):

$$\frac{\mathrm{d}}{\mathrm{d}x} \frac{\partial \boldsymbol{U}(x)}{\partial I_k} = (\frac{\partial \boldsymbol{F}}{\partial \boldsymbol{U}})^{-1} [(\frac{\partial \boldsymbol{S}}{\partial \boldsymbol{U}} - s\mathbf{1} - \frac{\mathrm{d}\boldsymbol{U}}{\mathrm{d}x} \frac{\partial^2 \boldsymbol{F}}{\partial \boldsymbol{U}^2} - \frac{\mathrm{d}A}{\mathrm{d}x} \frac{\partial^2 \boldsymbol{F}}{\partial A \partial \boldsymbol{U}}) \frac{\partial \boldsymbol{U}(x)}{\partial I_k} + \frac{\partial \boldsymbol{S}}{\partial I}]. \tag{3.22}$$

where the vector $\partial \boldsymbol{U}(x) / \partial I_k$ is the variation rate due to the variation of I_k when $\boldsymbol{U}_{k-1}$ is fixed. The initial values of Equations (3.21) and (3.22) at $x = x_{k-1}$ are

$$\frac{\partial \boldsymbol{U}(x_{k-1})}{\partial \boldsymbol{U}_{k-1}} = \mathbf{1}, \quad \frac{\partial \boldsymbol{U}(x_{k-1})}{\partial I_k} = \mathbf{0}. \tag{3.23}$$

3.3.2.2 Calculation of the matrix $\partial \boldsymbol{U}_k / \partial \boldsymbol{U}_{k-1}$

Equations (3.16), (3.17), (3.18) and (3.19) lead to a relation between perturbations $\delta \boldsymbol{U}_{k-1}$ and δI_k:

$$\frac{\partial V_{\mathrm{gen}k}}{\partial \boldsymbol{U}_{k-1}} \delta \boldsymbol{U}_{k-1} + [Z_{\mathrm{gen}kk}(s) - Z_{\mathrm{load}kk}(s)] \delta I_k = 0 \tag{3.24}$$

where

$$\frac{\partial V_{\mathrm{gen}k}}{\partial \boldsymbol{U}_{k-1}} = -\int_{x_{k-1}}^{x_k} \frac{\partial E_x}{\partial \boldsymbol{U}} \frac{\partial \boldsymbol{U}(x)}{\partial \boldsymbol{U}_{k-1}} \mathrm{d}x \tag{3.25}$$

$$Z_{\mathrm{gen}kk}(s) = \frac{\partial V_{\mathrm{gen}k}}{\partial I_k} = -\int_{x_{k-1}}^{x_k} (\frac{\partial E_x}{\partial \boldsymbol{U}} \frac{\partial \boldsymbol{U}(x)}{\partial I_k} + \frac{\partial E_x}{\partial I_k}) \mathrm{d}x \tag{3.26}$$

$$Z_{\mathrm{load}kk}(s) = \frac{\partial V_{\mathrm{load}k}}{\partial I_k}. \tag{3.27}$$

By taking the loading condition into account, the variation rate matrix $\partial \boldsymbol{U}_k / \partial \boldsymbol{U}_{k-1}$ is given from Equation (3.15) by

$$\frac{\partial \boldsymbol{U}_k}{\partial \boldsymbol{U}_{k-1}} = \frac{\partial \boldsymbol{U}(x_k)}{\partial \boldsymbol{U}_{k-1}} + \frac{\partial \boldsymbol{U}(x_k)}{\partial I_k} \frac{\partial I_k}{\partial \boldsymbol{U}_{k-1}} \tag{3.28}$$

where $\partial \boldsymbol{U}(x_k)/\partial \boldsymbol{U}_{k-1}$ and $\partial \boldsymbol{U}(x_k)/\partial I_k$ are given by the integration of Equations (3.21) and (3.22) from $x = x_{k-1}$ to x_k with the initial values of Equation (3.23). The term $\partial I_k/\partial \boldsymbol{U}_{k-1}$ in Equation (3.28) depends on the loading condition. It is given from Equation (3.24) by

$$\frac{\partial I_k}{\partial \boldsymbol{U}_{k-1}} = -[Z_{\mathrm{gen}kk}(s) - Z_{\mathrm{load}kk}(s)]^{-1} \frac{\partial V_{\mathrm{gen}k}}{\partial \boldsymbol{U}_{k-1}}. \tag{3.29}$$

In the case of the constant current loading condition, incidentally, $\partial I_k/\partial \boldsymbol{U}_{k-1} = \boldsymbol{0}$ because $Z_{\mathrm{load}kk} = \infty$.

3.3.3 Linear Stability Analysis Method

A linear stability analysis examines the time growth of perturbations of load currents. The perturbations of load currents continue to circulate through the channel and the load circuit. Thus, the MHD generator becomes unstable when the time growth rate of the perturbation is positive even if it is small. In the case of the direct-coupling scheme, whether the perturbations grow or decay is judged in the following way.

From Equations (3.19), (3.26) and (3.27), the equation for the perturbation of the k-th load current, δI_k, is given as

$$\Delta_k(s)\delta I_k = 0 \tag{3.30}$$

where

$$\Delta_k(s) = Z_{\mathrm{gen}kk}(s) - Z_{\mathrm{load}kk}(s). \tag{3.31}$$

Equation (3.30) implies that the perturbation can exist only when

$$\Delta_k(s) = 0. \tag{3.32}$$

The perturbation of I_k increases when the growth rate s satisfies both Equation (3.32) and

$$\mathrm{Re}(s) > 0. \tag{3.33}$$

Whether s, which satisfies Equations (3.32) and (3.33), exists or not is judged by plotting the locus of $\Delta_k(\mathrm{j}\omega)(\omega : -\infty \to \infty)$. The perturbation grows in the k-th loading section if the locus turns clockwise around the origin. This analysis requires the assumption that the transformation (3.31): $s \rightarrow \Delta_k(s)$ transforms the right half plain ($\mathrm{Re}(s) > 0$) into the right-hand side of the locus $\Delta_k(\mathrm{j}\omega)(\omega : -\infty \rightarrow \infty)$. We can examine whether or not the assumption holds by plotting values of $\Delta_k(s)$ for various points s which satisfy Equation (3.33) (see Appendix C).

The generator works stably if the perturbations decay in all the loading sections, while it becomes unstable if a perturbation grows in any of the loading sections.

3.3.4 Time-Dependent Calculation

Time-dependent calculations are also performed to confirm the linear stability analyses. The gasdynamical equation (3.1) is solved by the 1969 MacCormack two-step explicit method. The procedure is described in Subsection 2.3.1.

3.4 Conceptual Design of MHD Generator

The MHD generator analyzed here is a coal-fired diagonal type MHD generator of commercial-scale 46), whose basic specifications are listed in Table 3.1. The thermal input is 1300 MW and the number of loads is 4. The fuel used is the Datung coal of China and the oxidant is preheated air. Potassium, 1 %(wt), is seeded in the form of K_2CO_3. Figures 3.5 show the thermodynamical properties calculated from the thermodynamical equilibrium calculation 39). The composition of Chinese Datung coal is shown in Appendix B. Figures 3.6 show the distributions of quantities under the designed condition in the MHD generator. The load currents are determined to get almost the maximum electrical power output under the limitation of the electric field and the electric current density as:

$$|E_x| < 3500 \text{ V/m} \tag{3.34}$$

$$|J_y| < 10^4 \text{ A/m}^2. \tag{3.35}$$

At first, we analyze the MHD generator connected with 4 loads as is shown in Figure 3.7 (a). Table 3.2 lists the design values of the load currents, the load voltages and the load resistances.

Next, the two downstream loading sections of the four sections are further subdivided into four loading sections in order to stabilize the MHD generator. Figure 3.7 (b) shows the loading scheme in the case of this 6 loads connection. Table 3.3 shows the load currents, the load voltages and the load resistances in this case.

Table 3.1: Basic specifications of diagonal MHD generator

Fuel	Chinese Datung coal
Seed, Seed fraction	K_2CO_3, 1 %(wt)
Thermal input	1300 MW
Channel length	15 m
Inlet stagnation pressure	4.50 atm
Exit stagnation pressure	1.17 atm
Inlet stagnation temperature	2700 K
Exit stagnation temperature	2370 K
Inlet Mach number	1.2
Maximum magnetic flux density	6 T
Electrical power output	220.6 MW
Enthalpy extraction ratio	16.97 %

Table 3.2: Load currents, load voltages, load resistances (connection with 4 loads)

Loading section	Section length	Load current	Load voltage	Load resistance
1st	3.75 m	12000 A	6883 V	0.5737 Ω
2nd	3.75 m	8000 A	7919 V	0.9899 Ω
3rd	3.75 m	5800 A	7187 V	1.239 Ω
4th	3.75 m	4000 A	8249 V	2.062 Ω

Table 3.3: Load currents, load voltages, load resistances (connection with 6 loads)

Loading section	Section length	Load current	Load voltage	Load resistance
1st	3.75 m	12000 A	6883 V	0.5737 Ω
2nd	3.75 m	8000 A	7919 V	0.9899 Ω
3rd	1.875 m	5800 A	4625 V	0.7975 Ω
4th	1.875 m	5800 A	2561 V	0.4417 Ω
5th	1.875 m	4000 A	5233 V	1.308 Ω
6th	1.875 m	4000 A	3015 V	0.7539 Ω

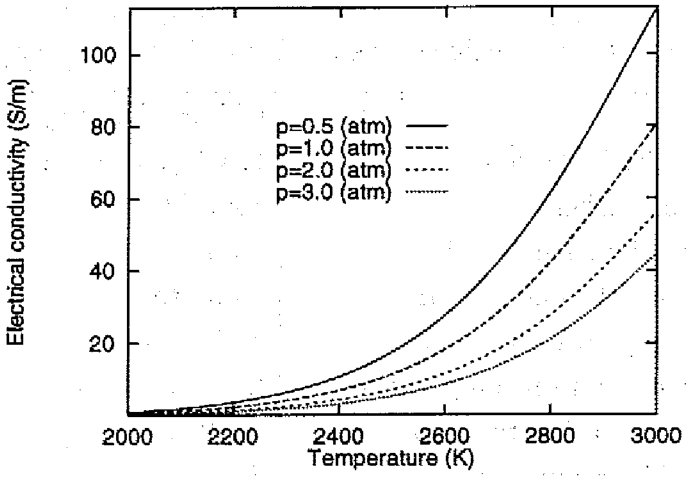

(a) Electrical conductivity

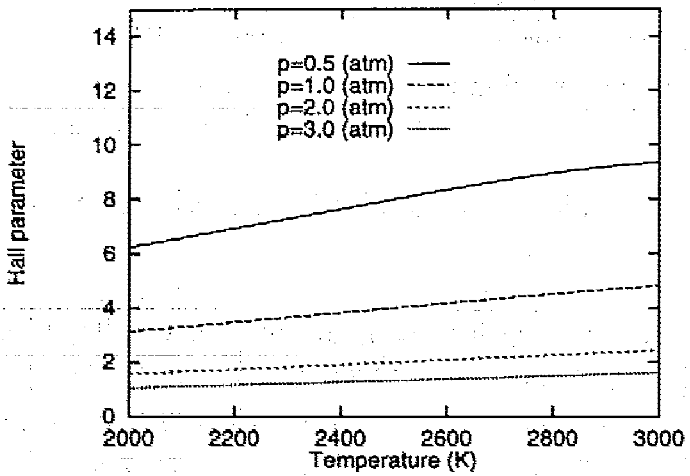

(b) Hall parameter (B=5 T)

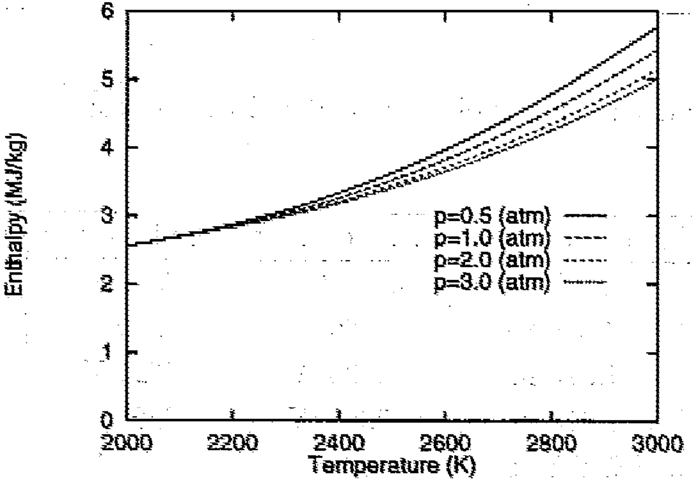

(c) Enthalpy

Figure 3.5: Thermodynamical properties of Chinese Datung coal

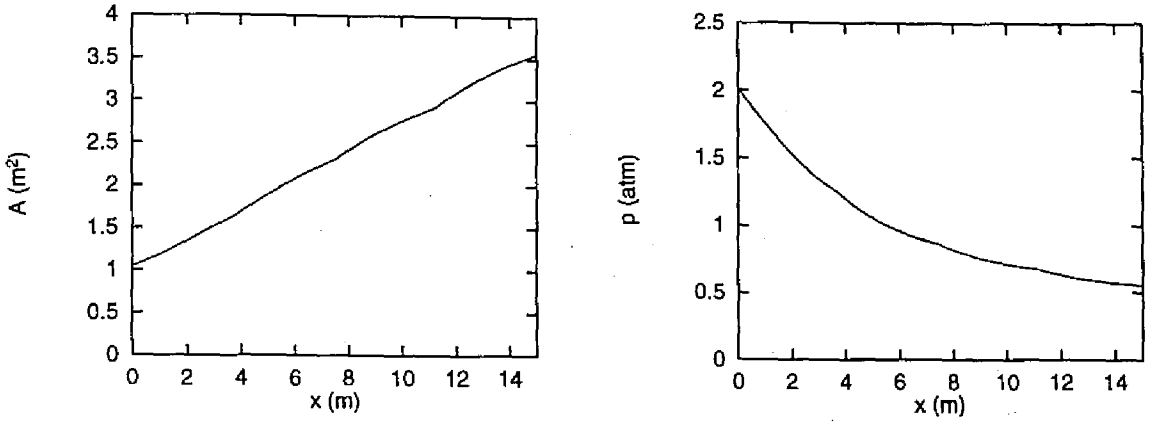

(a) Duct cross section (b) Pressure

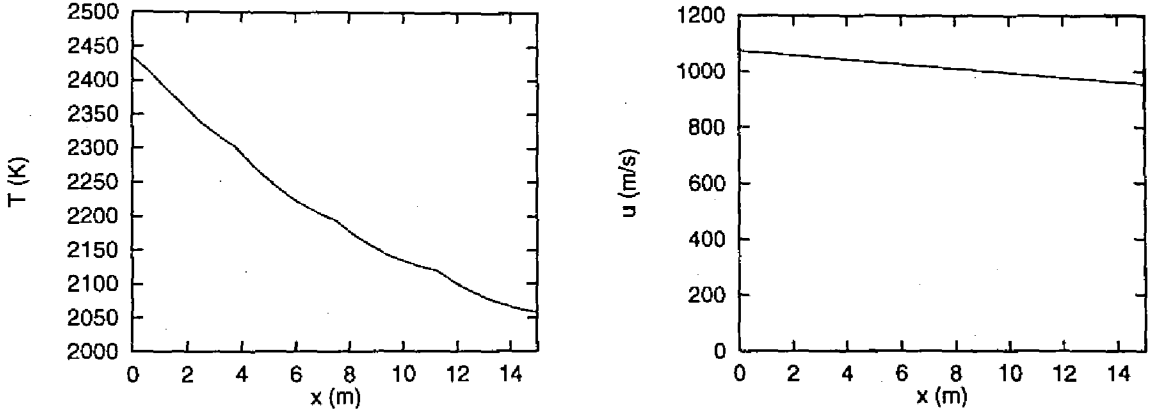

(c) Temperature (d) Flow velocity

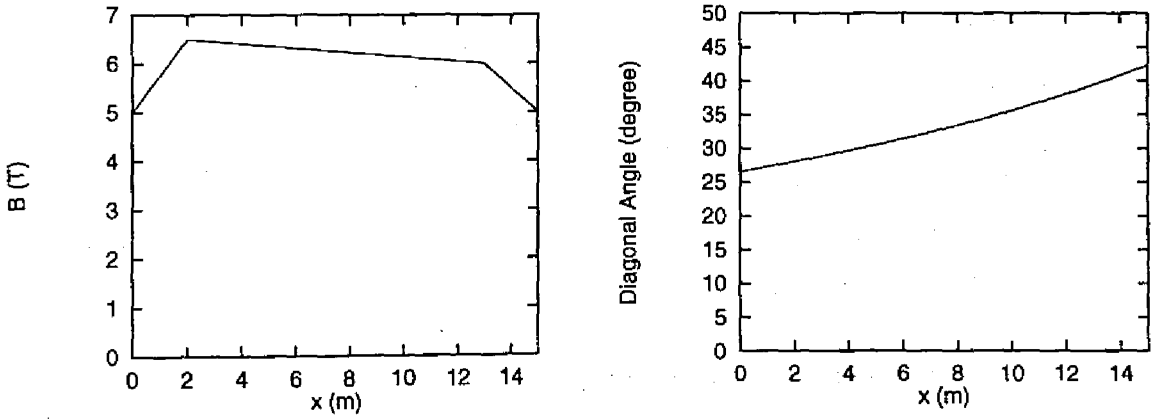

(e) Magnetic flux density (f) Diagonal angle

Figure 3.6: Distributions of quantities under design condition

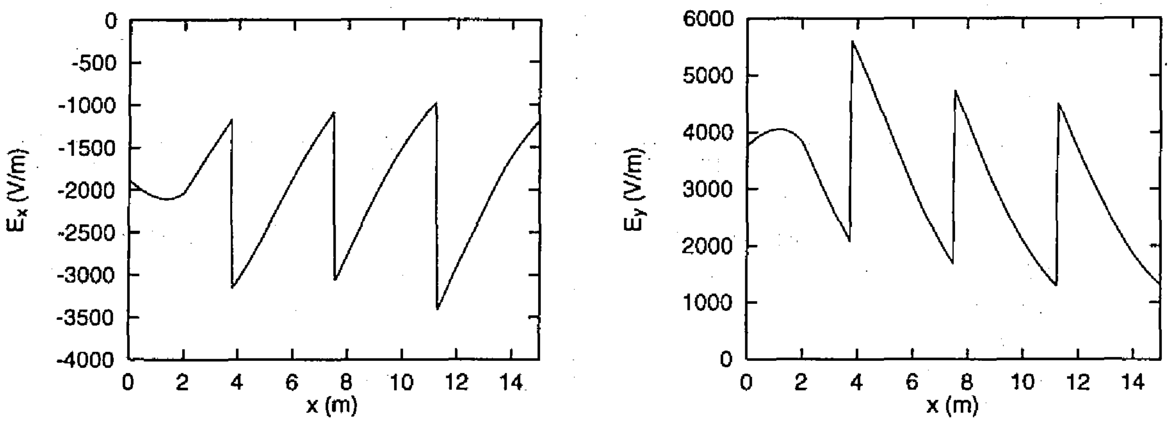

(g) Electric field in x-direction

(h) Electric field in y-direction

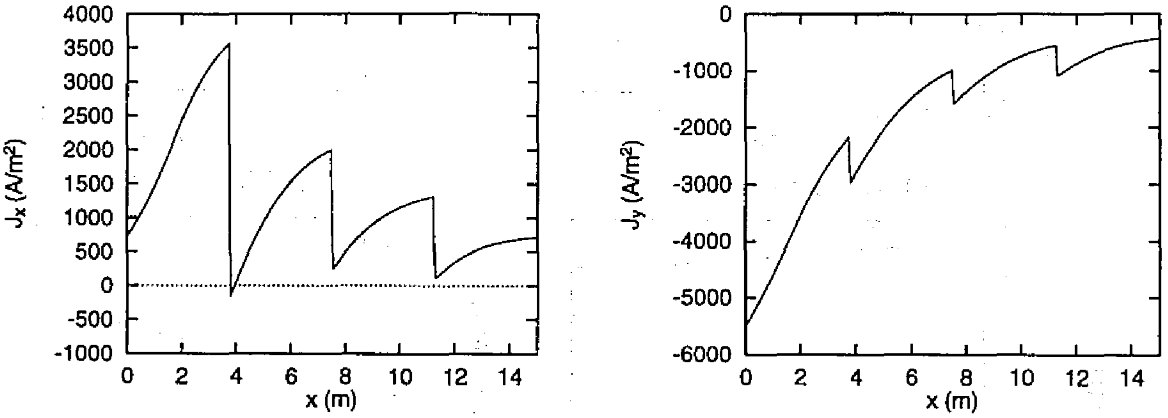

(i) Electric current density in x-direction

(j) Electric current density in y-direction

Figure 3.6: Distributions of quantities under design condition

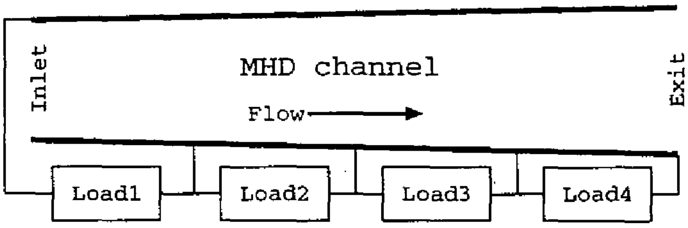

(a) 4 loads connection

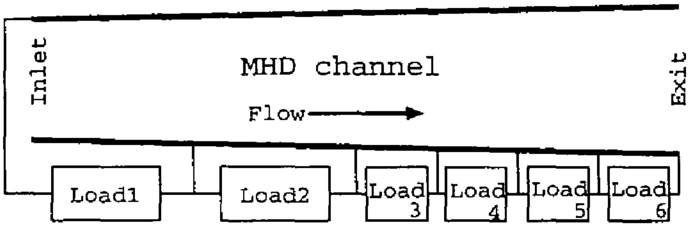

(b) 6 loads connection

Figure 3.7: Load circuit

3.5 Results of Analyses

3.5.1 Results of Sensitivity Analysis

The three eigenvalues of the matrix $\partial U_n/\partial U_0$ give the spatial growth rate of inlet disturbance during propagation to the exit. The stability of the generator is evaluated by the maximum absolute value of the three eigenvalues, which we call "sensitivity of the channel" in this chapter. On the other hand, the three eigenvalues of the matrix $\partial U_k/\partial U_{k-1}$ signify the spatial growth rate of disturbance during propagation along the k-th loading section. The stability of the k-th loading section is also examined by the maximum absolute value of the three eigenvalues, which we call " sensitivity of the k-th loading section".

At first, the sensitivity is calculated when the generator has 4 loads and $s = 0$. Table 3.4 lists the sensitivity of the channel (the maximum absolute value of the eigenvalues of $\partial U_n/\partial U_0$) calculated under various loading conditions. Table 3.4 shows that the generator with constant current loads has very high sensitivity (exceeding 10^4). The generator is far less sensitive, under the constant voltage loading condition and the ohmic condition, than under the constant current loading condition. Table 3.5 shows the sensitivities of the four loading sections (the maximum absolute value of the eigenvalues of $\partial U_k/\partial U_{k-1}, k = 1,2,3,4$) with the constant current loads. Table 3.5 indicates that the perturbations are magnified especially in the downstream loading sections.

Table 3.4: Sensitivity of the channel calculated under various loading conditions

Loading condition	Sensitivity of the channel
constant current loads	11920
constant voltage loads	31.83
ohmic loads	92.09

Table 3.5: Sensitivity of the four loading sections with constant current loads

Loading section	Sensitivity
1st	2.921
2nd	10.15
3rd	23.74
4th	50.75

Next, the sensitivity is calculated when the angular frequency of the perturbation is ω, i.e., $s = \mathrm{j}\omega$ where $\mathrm{j} = \sqrt{-1}$. Figure 3.8 shows the sensitivity of the channel when $0 \leq \omega \leq 3000$. In Figure 3.8, the solid line shows the sensitivity in the case of constant current loads, the broken line represents the case of 4 constant voltage loads, and the line $- \cdot - \cdot -$ represents the case of 6 constant voltage loads. Table 3.4 and Figure 3.8 show that the generator with the constant voltage loads has small growth rate for low frequency perturbation, whereas it has very large growth rate for high frequency perturbation, as much as with the constant current loads. The dependence of sensitivity on the perturbation frequency in the case of constant voltage loads is explained below. The wavelengths of the perturbation are given by u/ω and $(u \pm a)/\omega$ because the propagation velocities of the perturbation are approximately written as u, $u+a$, $u-a$ where a is the sound velocity. Accordingly, when ω is small, the wavelengths of the perturbation are large and the electric field in the loading section can be almost fixed by the constant voltage load. However, when ω is large; i.e., the wavelengths of the perturbation are small, the constant voltage load circuit cannot control the electric field and thus fails to suppress the high sensitivity.

The analytical study in Ref. 47) has suggested that the suppression of the fluctuation of J_y is effective for preventing the growth of perturbations. Then, inductors are inserted into the diagonal links in order to prevent the growth of the high frequency perturbations. Figure 3.9 shows the sensitivity of the channel with link inductors under the constant voltage loading condition. In Figure 3.9, the solid line shows the sensitivity when the link inductance L_{link} is 500 mH, and the broken line shows the sensitivity when L_{link} is 100 mH. Figure 3.9 indicates that the link inductor can prevent the growth of the high frequency perturbation. In particular, a very large inductance, for example L_{link} of 500 mH, effectively suppresses the growth of the high frequency perturbation.

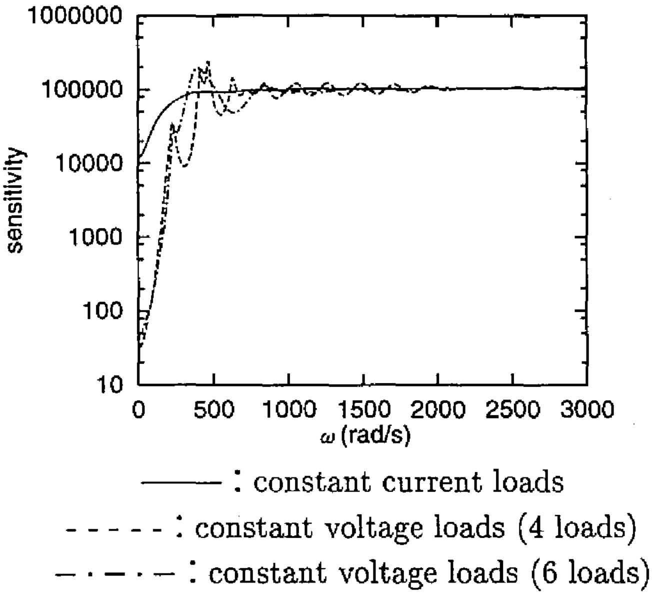

Figure 3.8: Sensitivity of the channel with various loading conditions

3.5.2 Results of Linear Stability Analysis

The linear stability is examined when the load circuit consists of 4 constant voltage loads. Figures 3.10, 3.11, 3.12 and 3.13 show the loci $\Delta_k(\mathrm{j}\omega)(\omega \geq 0)(k = 1, 2, 3, 4)$, respectively, where (◇) marks indicate the point at $\omega = 0$. In Figures 3.10 and 3.11, the loci $\Delta_1(\mathrm{j}\omega)$ and $\Delta_2(\mathrm{j}\omega)(\omega \geq 0)$ do not see the origin in the right-hand side. Accordingly, the generator can work stably in the 1st and the 2nd loading sections. The loci $\Delta_3(\mathrm{j}\omega)$ and $\Delta_4(\mathrm{j}\omega)(\omega \geq 0)$ turn clockwise around the origin in Figure 3.12

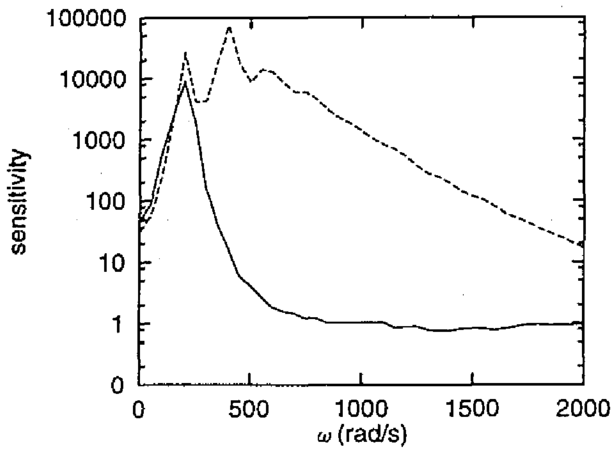

——:L_{link}=500 mH - - - - :L_{link}=100 mH

Figure 3.9: Sensitivity of the channel with link inductors

and 3.13, and thus the generator becomes unstable in the 3rd and the 4th loading sections.

Next, the linear stability analysis is performed in the case of 6 loads shown in Figure 3.7 (b), where the two unstable downstream loading sections are subdivided into 4 loading sections. Figure 3.14 shows $\Delta_6(j\omega)(\omega \geq 0)$ in the case of 6 constant voltage loads. In Figure 3.14, the locus does not see the origin in the right-hand side, which means that the generator behaves stably in the 6th loading section. By examining the loci for the other loading sections in the same way, it is found that the generator is stable in all the loading sections. The above analysis shows that the growth of load current perturbation is suppressed by subdividing the unstable loading sections.

3.5.3 Time-Dependent Calculations

Figures 3.15 show the time-dependent distributions of Mach number calculated under the loading conditions listed below:

(a) constant current loads (4 loads)
(b) constant voltage loads (6 loads)
(c) constant voltage loads (6 loads), link inductance L_{link} is 100 mH
(d) constant voltage loads (6 loads), link inductance L_{link} is 500 mH

where the design-point condition is used for the initial condition. The gasdynamical variables are fixed at the inlet for the inlet gasdynamical boundary condition.

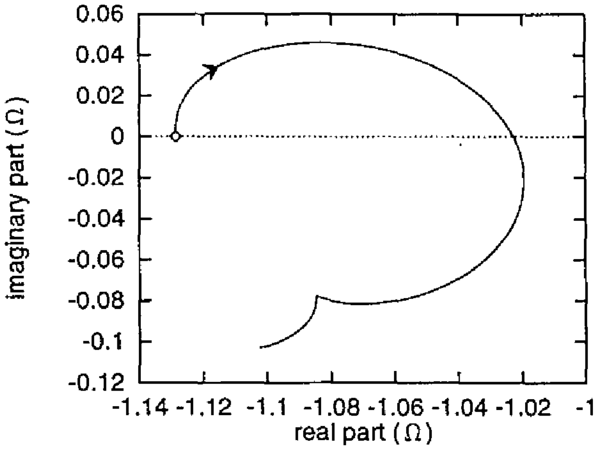

Figure 3.10: Locus $\Delta_1(j\omega)(\omega \geq 0)$ with 4 constant voltage loads

From the view point of the linear stability analysis, the generator with the constant current loads is stable because perturbations of the load currents do not exist. Figure 3.15 (a), however, shows that the generator becomes unstable with the growth of fluctuation in the flow field. This instability is caused by the high sensitivity under the constant current loading condition as indicated by the sensitivity analysis. The difference between the numerical scheme used in the design calculation (Runge-Kutta method) and the scheme in the time-dependent calculation (MacCormack method) causes numerical errors, which are utilized here as perturbations. These perturbations are magnified during the propagation and become so large in the downstream region that the flow in the generator cannot be maintained at the design-point.

A physical explanation of the instability is given below. It is assumed that a positive temperature perturbation is added to the flow. Since the electrical conductivity has an exponential dependence on the temperature as shown in Figure 3.5 (a), this temperature perturbation leads to a sharp increase of the electrical conductivity. When the electrical conductivity increases, the current density in the y-direction, J_y, also increases. The increase of J_y strengthens the Lorentz force J_yB. When the Lorentz force becomes large, the kinetic energy of the working gas is converted into the internal energy of the gas, and therefore, the temperature of the gas increases again. The flow disturbance is thus amplified by the positive feedback, leading to the instability.

Figure 3.15 (b) shows the time-dependent distribution of Mach number in the

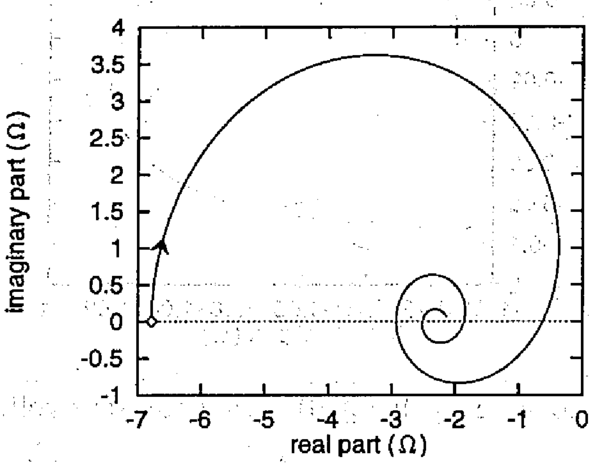

Figure 3.11: Locus $\Delta_2(j\omega)(\omega \geq 0)$ with 4 constant voltage loads

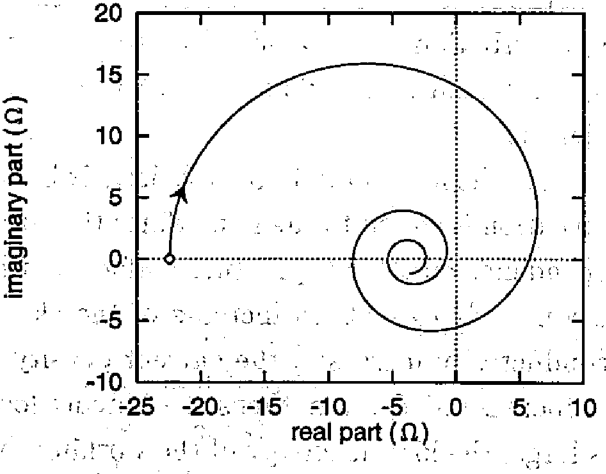

Figure 3.12: Locus $\Delta_3(j\omega)(\omega \geq 0)$ with 4 constant voltage loads

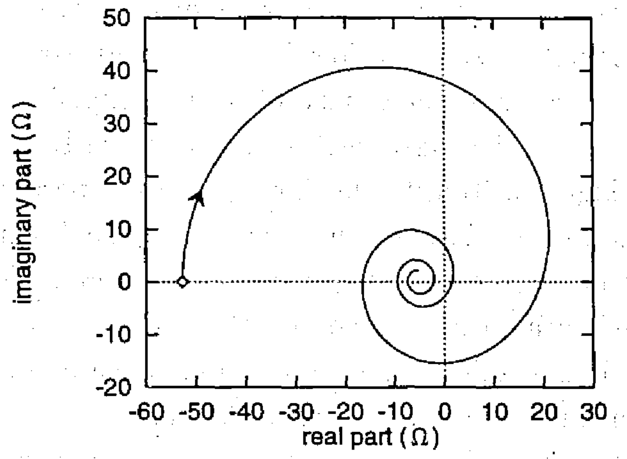

Figure 3.13: Locus $\Delta_4(j\omega)(\omega \geq 0)$ with 4 constant voltage loads

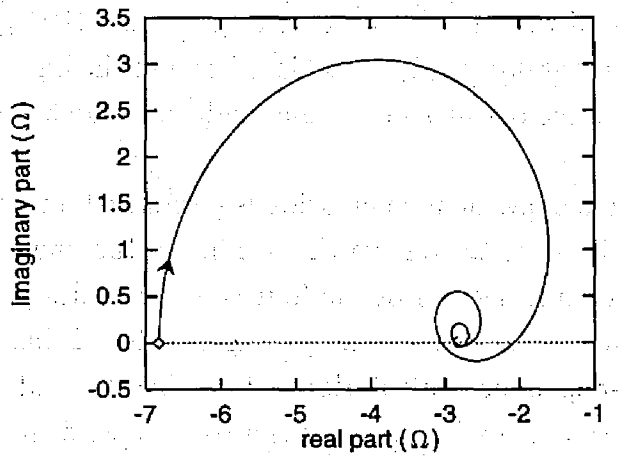

Figure 3.14: Locus $\Delta_6(j\omega)(\omega \geq 0)$ with 6 constant voltage loads

case of 6 constant voltage loads. The generator becomes unstable. In this case, the linear stability analysis indicates that small perturbations of the load currents do not grow along with time. On the other hand, the sensitivity analysis shows that the generator has a large spatial growth rate for high frequency perturbations while the generator is not sensitive to low frequency perturbations. Accordingly, the reason why the generator becomes unstable can be explained below. The high frequency part of the perturbations which comes transiently into the flow grows large because of the high sensitivity. This large growth of perturbations induces a shock wave in the duct, which destroys the flow field at the design-point condition.

Figures 3.15 (c) and (d) show results of time-dependent calculations when the generator is connected with 6 constant voltage loads and with diagonal-link inductors. The generator is unstable with the link inductance of 100 mH, whereas it works stably when the inductance is as large as 500 mH.

Instead of the link inductor, current-control circuits are inserted into diagonal links to suppress fluctuations of electrode currents in actual operations. The value of the inductance obtained in this analysis evaluates the extent to which the fluctuation of the current must be suppressed by the control circuit.

3.5.4 Validity of Linear Stability Analysis

Table 3.6 summarizes the results of linear stability analyses and time-dependent calculations. Table 3.6 shows that the time-dependent calculations often result in unstable behaviors of the MHD generator even if the MHD generator is stable according to the linear stability analysis. This is because the linear stability analysis is not valid when the large disturbances which induce a shock wave come from the upstream region.

Consequently, a time-dependent calculation is performed for only one of the multiple loading sections in order to confirm the validity of the linear stability analysis. We analyze the 3rd loading section of the four constant voltage loads and the 6th loading section in the case of 6 constant voltage loads. Table 3.7 and 3.8 show results of these time-dependent calculations. In Table 3.7 and 3.8, results of the linear stability analysis agree with those of the time-dependent calculations. This agreement indicates that the linear stability analysis is valid for small disturbances.

Here, we consider the 3rd loading section in the case of 4 constant voltage loads. Figure 3.16 (a) and (b) show the time-dependent variations of the 3rd load current and the Mach number distribution when the time-dependent calculation is carried

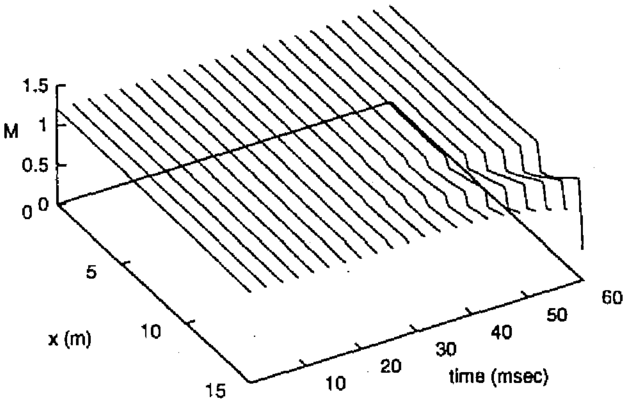

(a) With constant current loads

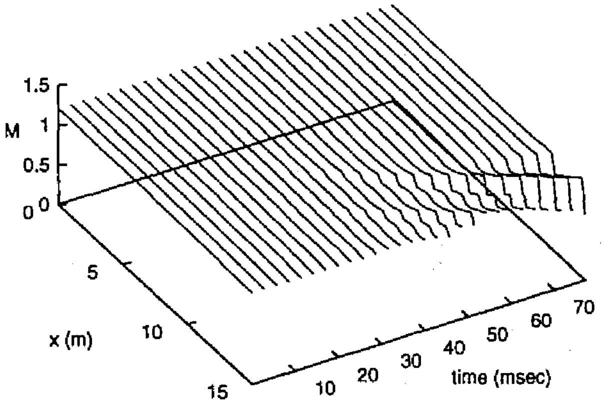

(b) With 6 constant voltage loads

Figure 3.15: Time-dependent distribution of Mach number

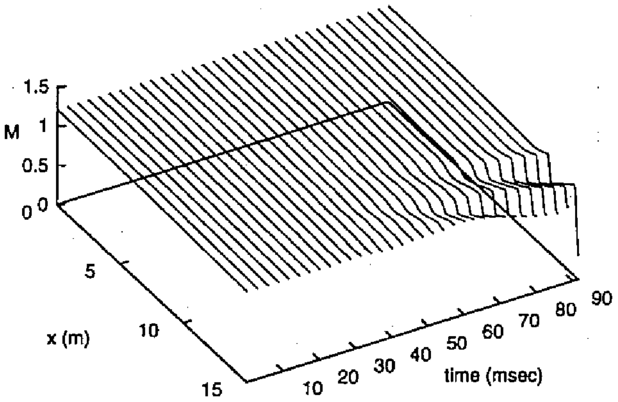

(c) With link inductance of 100 mH and with 6 constant voltage loads

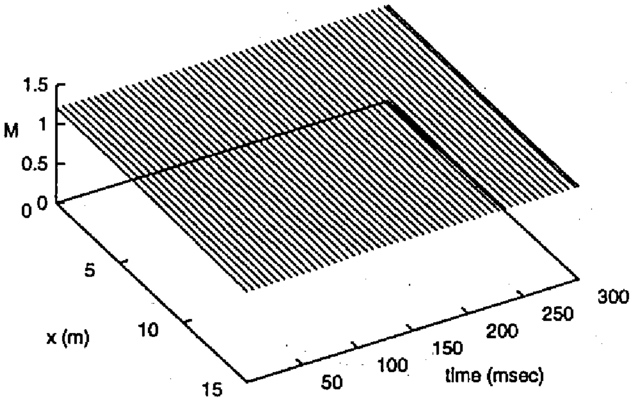

(d) With link inductance of 500 mH and with 6 constant voltage loads

Figure 3.15: Time-dependent distribution of Mach number

Table 3.6: Results of linear stability analyses and time-dependent calculations

Number of loads	Loading condition	Diagonal link condition	Linear stability analysis	Time-dependent calculation
4	constant current	shorted	stable	unstable
4	constant voltage	shorted	unstable in 3rd, 4th load sections	unstable
4	ohmic	shorted	unstable in 3rd, 4th load sections	unstable
4	constant voltage	L_{link}=500 mH	unstable in 3rd, 4th load sections	unstable
6	constant voltage	shorted	stable	unstable
6	ohmic	shorted	stable	unstable
6	constant voltage	L_{link}=100 mH	stable	unstable
6	constant voltage	L_{link}=500 mH	stable	stable

Table 3.7: Results of time-dependent calculations for 3rd loading section

Loading condition	Linear Stability analysis	Time-dependent calculation
constant current	stable	stable
constant voltage	unstable	unstable
ohmic	unstable	unstable

Table 3.8: Results of time-dependent calculations for 6th loading section

Loading condition	Linear Stability analysis	Time-dependent calculation
constant current	stable	stable
constant voltage	stable	stable
ohmic	stable	stable

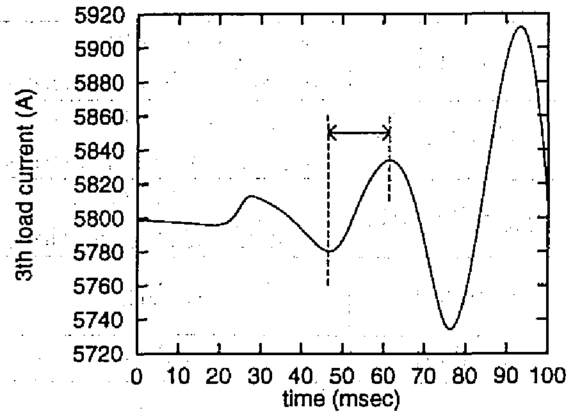

(a) Time variation of 3rd load current

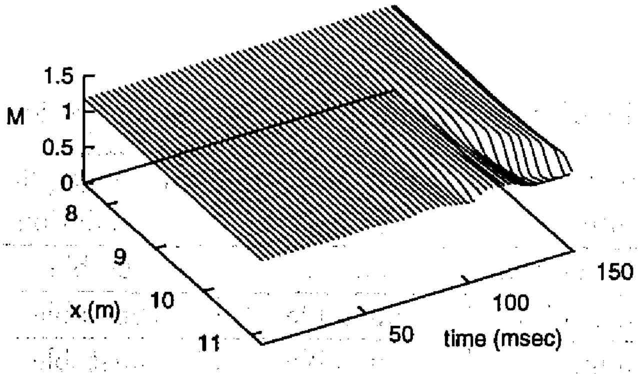

(b) Time-dependent distribution of Mach number

Figure 3.16: Results of time-dependent calculation only for 3rd loading section

out only for the 3rd loading section. In Figure 3.16 (a) and (b), the load current fluctuation grows as predicted by the linear stability analysis, after which a shock wave occurs in the duct and the generator becomes unstable. From the linear stability analysis, we can obtain the growth rate of the load current perturbation by calculating the zeropoint of $\Delta_3(s)$. In this case, the zeropoint s=41+j209 is obtained for the growth rate of the perturbation of the 3rd load current. On the other hand, the flow propagation time along the one loading section is about 3.7 msec. Then, the load current perturbation is magnified only 1.16(=exp(41×3.7×10^{-3})) times during the flow propagation time. Accordingly, it takes more calculation time than the flow propagation time to find the instability caused by the growth of the load current perturbation. Moreover, it is also difficult to estimate the calculation time needed for finding this instability without knowing the growth rate. Thus, the linear stability analysis is effective for examining the instability caused by the growth of the load current perturbation.

In the region indicated by the arrow ($\longleftrightarrow$) in Figure 3.16 (a), the growth rate of the load current oscillation is also calculated at 36+j209, which approximately agrees with the growth rate evaluated from the linear stability analysis.

3.6 General Loading Scheme

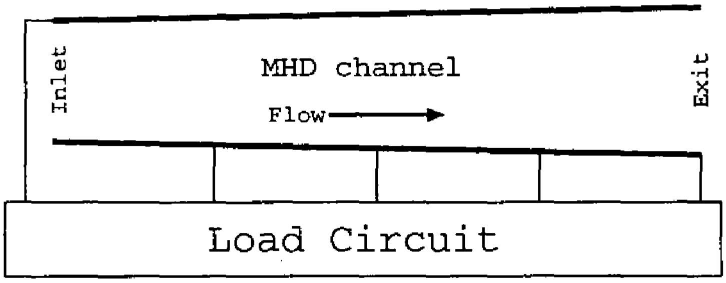

Figure 3.17: MHD generator with general loading scheme

In this section, the MHD generator with a general loading scheme shown in Figure 3.17 is analyzed. In the general loading scheme, the load voltage of the k-th loading section $V_{\mathrm{load}k}$ depends not only on the k-th load current but also on the other load currents $I_i(i \neq k)$. Accordingly, the individual loading sections cannot be treated separately.

The generator voltage vector $\boldsymbol{V}_{\text{gen}}$, the load current vector $\boldsymbol{I}$ and the load voltage vector $\boldsymbol{V}_{\text{load}}$ are defined as:

$$\boldsymbol{V}_{\text{gen}} = \begin{pmatrix} V_{\text{gen}1} \\ \vdots \\ V_{\text{gen}n} \end{pmatrix}, \quad \boldsymbol{I} = \begin{pmatrix} I_1 \\ \vdots \\ I_n \end{pmatrix}, \quad \boldsymbol{V}_{\text{load}} = \begin{pmatrix} V_{\text{load}1}(\boldsymbol{I}) \\ \vdots \\ V_{\text{load}n}(\boldsymbol{I}) \end{pmatrix}. \tag{3.36}$$

The loading condition follows as

$$\boldsymbol{V}_{\text{gen}}(\boldsymbol{U}_0, \boldsymbol{I}) - \boldsymbol{V}_{\text{load}}(\boldsymbol{I}) = 0. \tag{3.37}$$

3.6.1 Sensitivity Analysis

In the case of the general loading scheme, while the matrix $\partial \boldsymbol{U}_k / \partial \boldsymbol{U}_{k-1}$ cannot be evaluated separately, the sensitivity matrix $\partial \boldsymbol{U}_n / \partial \boldsymbol{U}_0$ is calculated as below. From Equation (3.15), the sensitivity matrix $\partial \boldsymbol{U}_n / \partial \boldsymbol{U}_0$ is given by

$$\begin{aligned} \frac{\partial \boldsymbol{U}_n}{\partial \boldsymbol{U}_0} &= \frac{\partial \boldsymbol{U}(x_n)}{\partial \boldsymbol{U}_{n-1}} \frac{\partial \boldsymbol{U}_{n-1}}{\partial \boldsymbol{U}_0} + \frac{\partial \boldsymbol{U}(x_n)}{\partial I_n} \frac{\partial I_n}{\partial \boldsymbol{U}_0} \\ &= \frac{\partial \boldsymbol{U}(x_n)}{\partial \boldsymbol{U}_{n-1}} \left[\frac{\partial \boldsymbol{U}(x_{n-1})}{\partial \boldsymbol{U}_{n-2}} \frac{\partial \boldsymbol{U}_{n-2}}{\partial \boldsymbol{U}_0} + \frac{\partial \boldsymbol{U}(x_{n-1})}{\partial I_{n-1}} \frac{\partial I_{n-1}}{\partial \boldsymbol{U}_0} \right] + \frac{\partial \boldsymbol{U}(x_n)}{\partial I_n} \frac{\partial I_n}{\partial \boldsymbol{U}_0} \\ &\vdots \\ &= \frac{\partial \boldsymbol{U}(x_n)}{\partial \boldsymbol{U}_0} + \sum_{i=1}^{n} \frac{\partial \boldsymbol{U}(x_n)}{\partial I_i} \frac{\partial I_i}{\partial \boldsymbol{U}_0}. \end{aligned} \tag{3.38}$$

In the above equation, $\partial \boldsymbol{U}(x_k) / \partial \boldsymbol{U}_0 (k > 2)$ and $\partial \boldsymbol{U}(x_k) / \partial I_i (k > i)$ are given from Equation (3.15) by

$$\frac{\partial \boldsymbol{U}(x_k)}{\partial \boldsymbol{U}_0} = \frac{\partial \boldsymbol{U}(x_k)}{\partial \boldsymbol{U}_{k-1}} \frac{\partial \boldsymbol{U}(x_{k-1})}{\partial \boldsymbol{U}_{k-2}} \cdots \frac{\partial \boldsymbol{U}(x_1)}{\partial \boldsymbol{U}_0} \tag{3.39}$$

$$\frac{\partial \boldsymbol{U}(x_k)}{\partial I_i} = \frac{\partial \boldsymbol{U}(x_k)}{\partial \boldsymbol{U}_{k-1}} \frac{\partial \boldsymbol{U}(x_{k-1})}{\partial \boldsymbol{U}_{k-2}} \cdots \frac{\partial \boldsymbol{U}(x_{i+1})}{\partial \boldsymbol{U}_i} \frac{\partial \boldsymbol{U}(x_i)}{\partial I_i} \tag{3.40}$$

and $\partial I_i / \partial \boldsymbol{U}_0 (i = 1, \cdots, n)$ are determined by the loading condition as follows.

From Equation (3.37), a relation between perturbations $\delta \boldsymbol{U}_0$ and $\delta \boldsymbol{I}$ is obtained:

$$\frac{\partial \boldsymbol{V}_{\text{gen}}}{\partial \boldsymbol{U}_0} \delta \boldsymbol{U}_0 + [\boldsymbol{Z}_{\text{gen}}(s) - \boldsymbol{Z}_{\text{load}}(s)] \delta \boldsymbol{I} = 0. \tag{3.41}$$

The matrix $\partial \boldsymbol{V}_{\text{gen}} / \partial \boldsymbol{U}_0$ is given by

$$\frac{\partial \boldsymbol{V}_{\text{gen}}}{\partial \boldsymbol{U}_0} = \begin{pmatrix} \partial V_{\text{gen}1} / \partial \boldsymbol{U}_0 \\ \vdots \\ \partial V_{\text{gen}n} / \partial \boldsymbol{U}_0 \end{pmatrix} \tag{3.42}$$

where $\partial V_{\mathrm{gen}1}/\partial \boldsymbol{U}_0$ is given by Equation (3.25) and $\partial V_{\mathrm{gen}k}/\partial \boldsymbol{U}_0 (k > 2)$ are given from Equation (3.16) by

$$\frac{\partial V_{\mathrm{gen}k}}{\partial \boldsymbol{U}_0} = \frac{\partial V_{\mathrm{gen}k}}{\partial \boldsymbol{U}_{k-1}} \frac{\partial \boldsymbol{U}(x_{k-1})}{\partial \boldsymbol{U}_0}. \tag{3.43}$$

The generator impedance matrix $\boldsymbol{Z}_{\mathrm{gen}}(s)$ is given by

$$\boldsymbol{Z}_{\mathrm{gen}}(s) = \partial \boldsymbol{V}_{\mathrm{gen}}/\partial \boldsymbol{I} = \begin{pmatrix} Z_{\mathrm{gen}11} & 0 & \cdots & 0 \\ Z_{\mathrm{gen}21} & Z_{\mathrm{gen}22} & \cdots & 0 \\ \vdots & \vdots & \ddots & \vdots \\ Z_{\mathrm{gen}n1} & Z_{\mathrm{gen}n2} & \cdots & Z_{\mathrm{gen}nn} \end{pmatrix} \tag{3.44}$$

where

$$Z_{\mathrm{gen}ki}(s) = \partial V_{\mathrm{gen}k}/\partial I_i. \tag{3.45}$$

The generator impedance $Z_{\mathrm{gen}kk}$ is obtained from Equation (3.26), and the generator impedance $Z_{\mathrm{gen}ki}(k > i)$ is given from Equations (3.16) and (3.45) by

$$Z_{\mathrm{gen}ki} = \frac{\partial V_{\mathrm{gen}k}}{\partial \boldsymbol{U}_{k-1}} \frac{\partial \boldsymbol{U}(x_{k-1})}{\partial I_i}. \tag{3.46}$$

The loading impedance matrix $\boldsymbol{Z}_{\mathrm{load}}(s)$ is written as

$$\boldsymbol{Z}_{\mathrm{load}}(s) = \partial \boldsymbol{V}_{\mathrm{load}}/\partial \boldsymbol{I} = \begin{pmatrix} Z_{\mathrm{load}11} & Z_{\mathrm{load}12} & \cdots & Z_{\mathrm{load}1n} \\ Z_{\mathrm{load}21} & Z_{\mathrm{load}22} & \cdots & Z_{\mathrm{load}2n} \\ \vdots & \vdots & \ddots & \vdots \\ Z_{\mathrm{load}n1} & Z_{\mathrm{load}n2} & \cdots & Z_{\mathrm{load}nn} \end{pmatrix}. \tag{3.47}$$

where

$$Z_{\mathrm{load}ki}(s) = \partial V_{\mathrm{load}k}/\partial I_i. \tag{3.48}$$

From Equation (3.41), $\partial I_i/\partial \boldsymbol{U}_0 (i = 1, \cdots, n)$ are obtained as

$$\begin{pmatrix} \partial I_1/\partial \boldsymbol{U}_0 \\ \vdots \\ \partial I_n/\partial \boldsymbol{U}_0 \end{pmatrix} = -(\boldsymbol{Z}_{\mathrm{gen}} - \boldsymbol{Z}_{\mathrm{load}})^{-1} \frac{\partial \boldsymbol{V}_{\mathrm{gen}}}{\partial \boldsymbol{U}_0}. \tag{3.49}$$

3.6.2 Linear Stability Analysis

In the case of the general loading scheme, we cannot treat the behavior of the perturbation of each load current separately. However, we can judge whether the perturbation of $\boldsymbol{I}$ grows or decays in the following way.

Since supersonic flows are not affected by the downstream conditions, their inlet perturbations can be independent of the downstream conditions. We assume the following equation for the inlet boundary condition.

$$\delta \boldsymbol{U}_0 = 0. \tag{3.50}$$

From Equations (3.41) and (3.50), the equation for the perturbation of $\boldsymbol{I}$ is given by

$$(\boldsymbol{Z}_{\text{gen}}(s) - \boldsymbol{Z}_{\text{load}}(s))\delta \boldsymbol{I} = 0. \tag{3.51}$$

The perturbations of $\boldsymbol{I}$ increase when the growth rate s satisfies both

$$\Delta(s) = \det(\boldsymbol{Z}_{\text{gen}}(s) - \boldsymbol{Z}_{\text{load}}(s)) = 0. \tag{3.52}$$

and

$$\text{Re}(s) > 0. \tag{3.53}$$

Whether or not $\Delta(s)$ has a zero point which satisfies Equation (3.53) is judged by plotting the locus $\Delta(\mathrm{j}\omega)(\omega : -\infty \to \infty)$ in the same way as in Subsection 3.3.3.

3.6.3 Results of Analyses

In this subsection, the MHD generator with the feedback loading scheme, as is shown in Figure 3.18, is analyzed. The basic specifications are same as those described in Subsection 3.5. Table 3.9 lists the load currents, the load voltages and the load resistances with the feedback loading scheme. The loading impedance matrix with the ohmic loads is given by

$$\boldsymbol{Z}_{\text{load}} = \begin{pmatrix} 1.721 & -1.721 & 0 & 0 \\ -1.721 & 8.450 & -6.729 & 0 \\ 0 & -6.729 & 18.95 & -12.22 \\ 0 & 0 & -12.22 & 19.78 \end{pmatrix}. \tag{3.54}$$

3.6.3.1 Sensitivity analysis

Figure 3.19 shows the sensitivity of the channel under the ohmic loading condition. The generator has a low sensitivity for a low frequency perturbation, whereas it has a large growth rate for a high frequency perturbation. This result is similar to the one with the constant voltage loads of the direct coupling scheme.

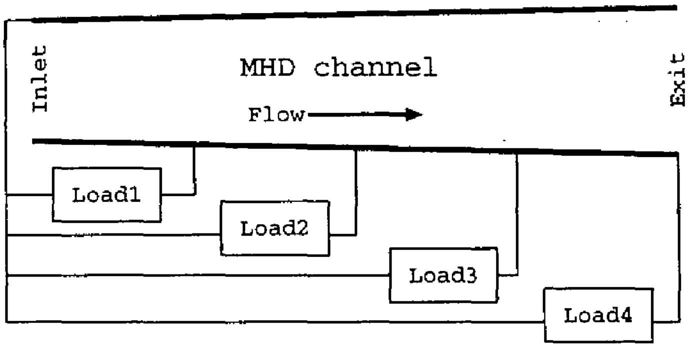

Figure 3.18: MHD generator with feedback loading scheme

Table 3.9: Load currents, load voltages and load resistances

Load number		Load current	Load voltage	Load resistance
1	$(0 \leq x \leq 3.75)$	4000 A	6883 V	1.721 Ω
2	$(0 \leq x \leq 7.5)$	2200 A	14800 V	6.729 Ω
3	$(0 \leq x \leq 11.25)$	1800 A	21990 V	12.22 Ω
4	$(0 \leq x \leq 15)$	4000 A	30240 V	7.560 Ω

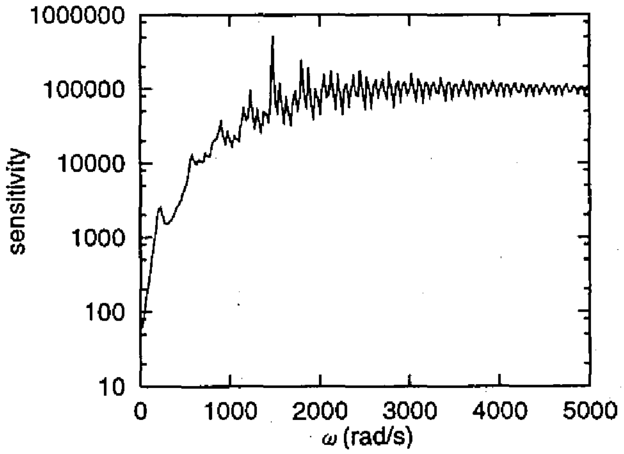

Figure 3.19: Sensitivity of the channel under ohmic loading condition with feedback loading scheme

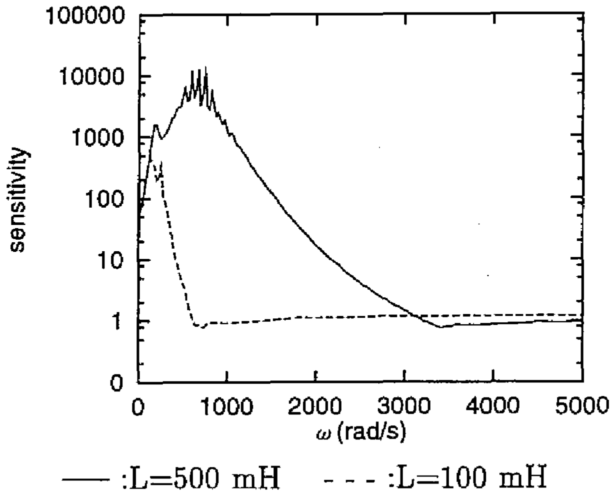

Figure 3.20: Sensitivity of the channel with link inductors (ohmic loads, feedback loading scheme)

Figure 3.20 depicts the sensitivity of the channel with link inductors under the ohmic loading condition. In Figure 3.20, the solid line plots the sensitivity in the case of L_{link}=100 mH, and the broken line corresponds to L_{link}=500 mH. Figure 3.20 indicates that the link inductor is effective in preventing the growth of the high frequency perturbation not only when the direct-coupling scheme is used but also when the feedback loading scheme is adopted.

3.6.3.2 Linear stability analysis and time-dependent calculation

Figure 3.21 plots the locus $\Delta(j\omega)(\omega \geq 0)$ under ohmic loading condition. In Figure 3.21, the locus turns around the origin clockwise and thus the generator becomes unstable.

The time-dependent calculation is also performed. Figure 3.22 shows the time-dependent distribution of Mach number. Figure 3.22 indicates that the generator becomes unstable as is expected by the linear stability analysis.

Table 3.10 summarizes results of linear stability analyses and time-dependent calculations in the case of the feedback loading scheme. In Table 3.10, the linear stability analysis and the time-dependent calculation indicate that the MHD generator, with feedback loading scheme, cannot work stably even when large inductors (for example L_{link}=500 mH) are inserted into the diagonal links.

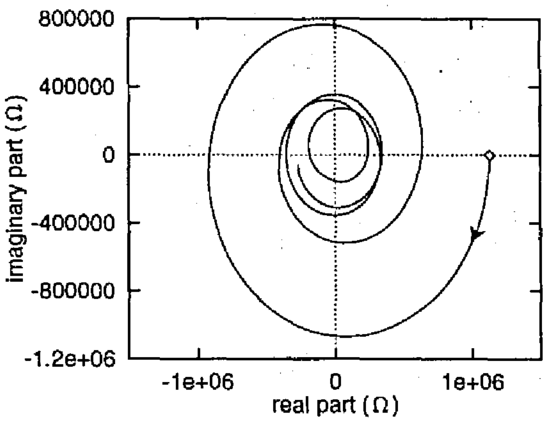

Figure 3.21: Locus $\Delta(j\omega)(\omega \geq 0)$ with ohmic loads (feedback loading scheme)

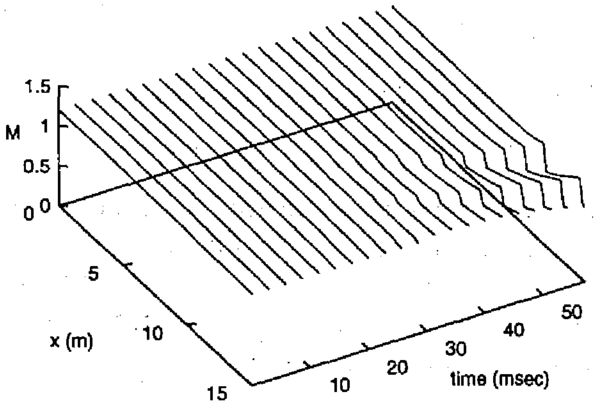

Figure 3.22: Time-dependent distribution of Mach number (feedback loading scheme)

Table 3.10: Results of linear stability analyses and time-dependent calculations with feedback loading scheme

Loading condition	Diagonal link condition	Linear stability analysis	Time-dependent calculation
ohmic	shorted	unstable	unstable
ohmic	L_{link}=100 mH	unstable	unstable
ohmic	L_{link}=500 mH	unstable	unstable

3.7 Concluding Remarks

The sensitivity analysis, the linear stability analysis and the time-dependent calculation were carried out for the coal-fired supersonic MHD generator of commercial-scale. The followings are the summaries of the results of these analyses.

- The MHD generator with constant current loads has a large spatial growth rate of perturbations and is apt to be unstable.
- The growth rates of low frequency perturbations are small in the MHD generator with constant voltage loads or ohmic loads.
- When inductors are inserted into the diagonal links, the growth of high frequency perturbations is suppressed.
- The subdivision of the unstable loading sections can prevent the growth of load current fluctuation.
- In the MHD generator analyzed here, the growth of the load current fluctuation cannot be suppressed with the feedback ohmic loads.
- The result of the time-dependent calculation confirms the validity of the linear stability analyses for small disturbances.

It is concluded that the generator with constant voltage loads or ohmic loads of the direct coupling scheme can be operated stably when the fluctuation of the electrode current is kept small.

Chapter 4 Stability Analysis of Subsonic Diagonal-Type MHD Generator of Commercial-Scale

4.1 Introduction

This chapter treats commercial-scale coal-fired subsonic diagonal-type MHD generators. Subsonic MHD generators have a merit that shock waves are absent in the duct flow. Acceleration and deceleration of flow in the subsonic channel are easier than in the supersonic channel. The author here examines the stability of commercial-scale subsonic diagonal-type MHD generators by a local linear perturbation analysis and a linear stability analysis of channel-length scale.

The local linear perturbation analysis 26) estimates local growth rates of traveling waves in the MHD channel by using a dispersion equation.

The channel-length stability analysis deals with the resonance instability related with gasdynamical boundary conditions. The gasdynamical boundary conditions of subsonic generator induce the reflection of waves at the inlet and the exit. If the repetition of the reflection amplifies the wave of flow disturbance, the generator becomes unstable. This instability however cannot be examined by the local linear perturbation analysis. Research 32) for disk type MHD generators has shown that the instability is greatly affected by the boundary conditions of the duct inlet and exit, and that the subsonic disk type generator works stably under appropriate boundary conditions. The author applies the channel-length linear stability analysis32), which was proposed for the subsonic disk type MHD generator by T. Matsuo, to the diagonal type generator.

At first, a conventionally designed channel 46) in which the flow velocity is near the sound velocity is examined. The linear stability analyses and time-dependent calculations are carried out for the conventional channel. The analyses show that the conventionally designed channel is apt to be unstable because of the growth of the upstream acoustic wave.

The author designs a new channel in which the Mach number is relatively low in order to suppress the instability. The new channel is also examined by the linear stability analyses and time-dependent calculations. These analyses show that the local growth rate of the upstream acoustic wave is reduced and that the instability of the generator is suppressed in the new channel.

4.2 Basic Equations

4.2.1 Gasdynamics and Electrodynamics

The basic equations used for the gasdynamical part are the same as the equations used in the analysis for the supersonic MHD generator. The flow in the MHD channel is described by Equation (3.1) and the state equations are given by Equation (3.5). The steady state flow is described by Equation (3.6).

The relation between the electric field and the electric current density is given by Equations (3.7), (3.8), (3.9) and (3.10), where the diagonal links are assumed to be short-circuited in this chapter except for the case particularly mentioned.

In order to analyze the stability of the generator, the perturbation is added to the steady-state flow. The perturbations of $\boldsymbol{U}$ and I are assumed to be given as

$$\boldsymbol{U} \to \boldsymbol{U} + \delta\boldsymbol{U}(x)\exp(st), \quad I \to I + \delta I\exp(st) \tag{4.1}$$

where s is the time growth rate of perturbations. From Equations (3.1) and (4.1), the equation which describes the propagation of perturbations is given by Equation (3.13).

4.2.2 Loading Condition

The MHD generator analyzed here has multi-loads and is divided into n loading sections $[x_{k-1}, x_k](k = 1, \cdots, n)$ as is shown in Figure 4.1. The position of the nozzle inlet is $x = x_{\text{int}}$ and the position of the diffuser exit is $x = x_{\text{ext}}$. In the present analysis, a direct coupling scheme is adopted as is shown in Figure 4.1.

The generator voltage vector $\boldsymbol{V}_{\text{gen}}$, the load current vector $\boldsymbol{I}$ and the load voltage vector $\boldsymbol{V}_{\text{load}}$ are defined by the following equations:

$$\boldsymbol{V}_{\text{gen}} = \begin{pmatrix} V_{\text{gen1}} \\ \vdots \\ V_{\text{gen}n} \end{pmatrix}, \quad \boldsymbol{I} = \begin{pmatrix} I_1 \\ \vdots \\ I_n \end{pmatrix}, \quad \boldsymbol{V}_{\text{load}} = \begin{pmatrix} V_{\text{load1}}(\boldsymbol{I}) \\ \vdots \\ V_{\text{load}n}(\boldsymbol{I}) \end{pmatrix}. \tag{4.2}$$

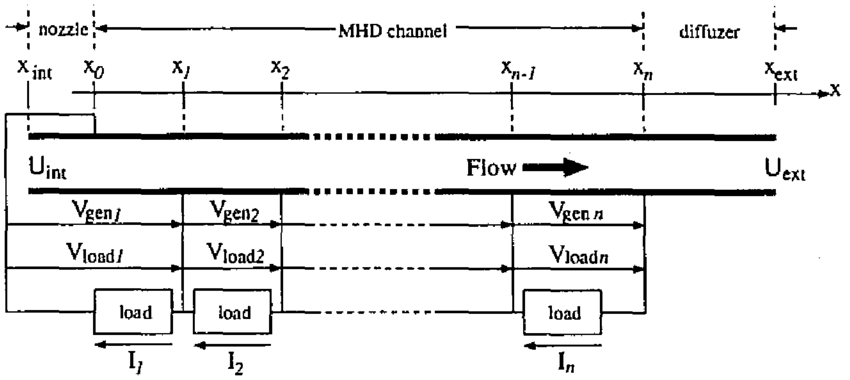

Figure 4.1: Loading scheme of multi-loaded MHD channel

The load voltages $\boldsymbol{V}_{\text{load}}$ are determined by the characteristics of loading circuit and by the load currents $\boldsymbol{I}$, while $V_{\text{gen}k}$ is determined by the gasdynamical variables $\boldsymbol{U}$ and the load current I_{k}, as given by Equation (3.16).

The gasdynamical variable vectors at the inlet and the exit are denoted by $\boldsymbol{U}_{\text{int}}$ and $\boldsymbol{U}_{\text{ext}}$, respectively. The integration of Equation (3.6) from $x = x_{\text{int}}$ gives $\boldsymbol{U}(x)$ in the steady state, which is written as a function of $\boldsymbol{U}_{\text{int}}$ and $\boldsymbol{I}$:

$$\boldsymbol{U}(x) = \boldsymbol{U}(x, \boldsymbol{U}_{\text{int}}, \boldsymbol{I}). \tag{4.3}$$

The exit condition $\boldsymbol{U}_{\text{ext}}$ and the generator voltages $\boldsymbol{V}_{\text{gen}}$ in the steady state are also described by functions of $\boldsymbol{U}_{\text{int}}$ and $\boldsymbol{I}$ from Equations (3.16) and (4.3) as:

$$\boldsymbol{U}_{\text{ext}} = \boldsymbol{U}_{\text{ext}}(\boldsymbol{U}_{\text{int}}, \boldsymbol{I}) \text{ , } \boldsymbol{V}_{\text{gen}} = \boldsymbol{V}_{\text{gen}}(\boldsymbol{U}_{\text{int}}, \boldsymbol{I}). \tag{4.4}$$

Then, the loading condition is given by

$$\boldsymbol{V}_{\text{gen}}(\boldsymbol{U}_{\text{int}}, \boldsymbol{I}) - \boldsymbol{V}_{\text{load}}(\boldsymbol{I}) = 0. \tag{4.5}$$

4.2.3 Gasdynamical Boundary Conditions

The inlet boundary requires two equations for the boundary condition while the exit boundary requires only one equation:

$$\text{inlet} : \boldsymbol{b}_{\text{int}}(\boldsymbol{U}_{\text{int}}) = 0(\in \boldsymbol{R}^2) \tag{4.6}$$

$$\text{exit} : b_{\text{ext}}(\boldsymbol{U}_{\text{ext}}) = 0(\in \boldsymbol{R}). \tag{4.7}$$

4.3 Method of Local Linear Perturbation Analysis

There exist three kinds of waves (entropy wave, upstream acoustic wave and downstream acoustic wave) in the MHD channel. The local linear perturbation analysis evaluates local, temporal or spatial growth rates of the three waves.

The local linear perturbation analysis does not treat perturbations of load currents, and thus the following equation is assumed.

$$\delta I = 0 \tag{4.8}$$

Next, we assume that $\delta \boldsymbol{U}(x)$ in Equation (4.1) is given by the following form

$$\delta \boldsymbol{U}(x) = \boldsymbol{U}_o e^{-\mathrm{j}kx} \tag{4.9}$$

where k is the wave number. Then from Equation (3.13) the following equation for the perturbation is obtained.

$$\boldsymbol{A}_d \boldsymbol{U}_o = \boldsymbol{0} \tag{4.10}$$

where

$$\boldsymbol{A}_d = s\boldsymbol{1} - \mathrm{j}k\frac{\partial \boldsymbol{F}}{\partial \boldsymbol{U}} - \frac{\partial \boldsymbol{S}}{\partial \boldsymbol{U}} + \frac{\mathrm{d}\boldsymbol{U}}{\mathrm{d}x}\frac{\partial^2 \boldsymbol{F}}{\partial \boldsymbol{U}^2} + \frac{\mathrm{d}A}{\mathrm{d}x}\frac{\partial^2 \boldsymbol{F}}{\partial A \partial \boldsymbol{U}}. \tag{4.11}$$

When Equation (4.10) has a non-zero solution of $\boldsymbol{U}_o$, the following dispersion equation is required.

$$\det\{\boldsymbol{A}_d(s)\} = 0 \tag{4.12}$$

This equation is a third order complex equation for s. When a solution of Equation (4.12) is written as $s = \alpha + \mathrm{j}\omega$, Equations (4.1) and (4.9) give a perturbation wave written as

$$\delta \boldsymbol{U}(x)\exp(st) = \boldsymbol{U}_o \exp(\alpha t)\exp\{\mathrm{j}(\omega t - kx)\}. \tag{4.13}$$

Equation (4.13) implies that the propagation velocity of wave is given by ω/k. When the wave number is sufficiently large, the propagation velocities of three waves are given by u, $u + a$ and $u - a$ where a is the sound velocity. Equation (4.13) also means that the amplitude of perturbation wave is multiplied by $\exp(\alpha|k/\omega|)$ during the propagation of the unit length. The present paper thus adopts the multiplier as the stability index, i.e.,

$$\text{Stability index} = \exp(\alpha|k/\omega|). \tag{4.14}$$

4.4 Method of Linear Stability Analysis of Channel-Length Scale

4.4.1 Separation of Perturbations into Downstream and Upstream Waves

The matrix $\partial \boldsymbol{F}/\partial \boldsymbol{U}$ has three eigenvalues which are given by

$$\lambda_1 = u + a, \lambda_2 = u, \lambda_3 = u - a. \tag{4.15}$$

Let the corresponding left-eigenvector matrix be

$$\boldsymbol{L} = \begin{pmatrix} \boldsymbol{l}_1 \\ \boldsymbol{l}_2 \\ \boldsymbol{l}_3 \end{pmatrix} = \frac{1}{a} \begin{pmatrix} \chi + \frac{\kappa u^2}{2} - au & -\kappa u + a & \kappa \\ \kappa(h - \frac{u^2}{2}) & \kappa u & -\kappa \\ \chi + \frac{\kappa u^2}{2} + au & -\kappa u - a & \kappa \end{pmatrix} \tag{4.16}$$

where

$$\chi = (\frac{\partial p}{\partial \rho})_{\epsilon=\text{constant}} \tag{4.17}$$

$$\kappa = (\frac{\partial p}{\partial \epsilon})_{\rho=\text{constant}} \tag{4.18}$$

$$\epsilon = \rho \varepsilon \tag{4.19}$$

$$a = \sqrt{\chi + \kappa h}. \tag{4.20}$$

We transform $\delta \boldsymbol{U}$ into $\delta \boldsymbol{w}$ by $\boldsymbol{L}$ as

$$\delta \boldsymbol{w} = \boldsymbol{L}(\boldsymbol{U}) \delta \boldsymbol{U}. \tag{4.21}$$

Then Equation (3.13) is also transformed into

$$\frac{\partial \delta \boldsymbol{w}}{\partial t} + \begin{pmatrix} u + a & 0 & 0 \\ 0 & u & 0 \\ 0 & 0 & u - a \end{pmatrix} \frac{\partial \delta \boldsymbol{w}}{\partial x} = \boldsymbol{S}_w \delta \boldsymbol{w} \tag{4.22}$$

where

$$\boldsymbol{S}_w = \boldsymbol{L}[(\frac{\partial \boldsymbol{S}}{\partial \boldsymbol{U}} - \frac{\mathrm{d}\boldsymbol{U}}{\mathrm{d}x} \frac{\partial^2 \boldsymbol{F}}{\partial \boldsymbol{U}^2} - \frac{\partial^2 \boldsymbol{F}}{\partial A \partial \boldsymbol{U}} \frac{\mathrm{d}A}{\mathrm{d}x}) \boldsymbol{L}^{-1} - \frac{\partial \boldsymbol{F}}{\partial \boldsymbol{U}} \sum_{k=1}^{3} \frac{\mathrm{d}U_k}{\mathrm{d}x} \frac{\partial \boldsymbol{L}^{-1}}{\partial U_k}]. \tag{4.23}$$

From Equation (4.22), we can separate $\delta \boldsymbol{w}$ into the downstream running part, $\delta \boldsymbol{w}^+$, and the upstream running part, δw^-, as

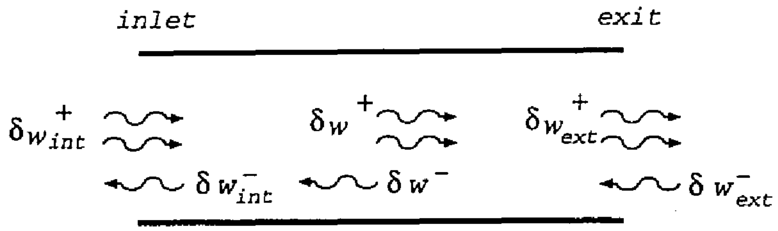

Figure 4.2: Downstream and upstream waves

$$\delta \boldsymbol{w}^{+} = \boldsymbol{L}^{+}\delta \boldsymbol{U}, \quad \delta w^{-} = \boldsymbol{l}^{-}\delta \boldsymbol{U} \tag{4.24}$$

where

$$\boldsymbol{L}^{+} = \begin{pmatrix} \boldsymbol{l}_1 \\ \boldsymbol{l}_2 \end{pmatrix}, \boldsymbol{l}^{-} = \boldsymbol{l}_3. \tag{4.25}$$

The upstream wave δw^{-} is reflected at the inlet so as to satisfy the boundary condition (4.6) as

$$\frac{\partial \boldsymbol{b}_{\mathrm{int}}}{\partial \boldsymbol{U}_{\mathrm{int}}}\left(\frac{\partial \delta \boldsymbol{U}_{\mathrm{int}}}{\partial \delta \boldsymbol{w}_{\mathrm{int}}^{+}}\delta \boldsymbol{w}_{\mathrm{int}}^{+} + \frac{\partial \delta \boldsymbol{U}_{\mathrm{int}}}{\partial \delta w_{\mathrm{int}}^{-}}\delta w_{\mathrm{int}}^{-}\right) = 0 \tag{4.26}$$

where

$$\left(\frac{\partial \delta \boldsymbol{U}}{\partial \delta \boldsymbol{w}^{+}}, \frac{\partial \delta \boldsymbol{U}}{\partial \delta w^{-}}\right) = \boldsymbol{L}^{-1}. \tag{4.27}$$

The downstream wave $\delta \boldsymbol{w}^{+}$ is reflected at the exit so as to satisfy the boundary condition (4.7) as

$$\frac{\partial \boldsymbol{b}_{\mathrm{ext}}}{\partial \boldsymbol{U}_{\mathrm{ext}}}\left(\frac{\partial \delta \boldsymbol{U}_{\mathrm{ext}}}{\partial \delta \boldsymbol{w}_{\mathrm{ext}}^{+}}\delta \boldsymbol{w}_{\mathrm{ext}}^{+} + \frac{\partial \delta \boldsymbol{U}_{\mathrm{ext}}}{\partial \delta w_{\mathrm{ext}}^{-}}\delta w_{\mathrm{ext}}^{-}\right) = 0. \tag{4.28}$$

The upstream wave at the inlet, $\delta w_{\mathrm{int}}^{-}$, and the downstream wave at the exit, $\delta \boldsymbol{w}_{\mathrm{ext}}^{+}$, go out of the duct and do not affect the duct flow. On the other hand, the downstream wave at the inlet, $\delta \boldsymbol{w}_{\mathrm{int}}^{+}$, and the upstream wave at the exit, $\delta w_{\mathrm{ext}}^{-}$, propagate into the duct (see Figure 4.2).

For the convenience of analysis, we define a vector $\delta \boldsymbol{W}_{\mathrm{in}}$ which consists of the incoming waves, $\delta \boldsymbol{w}_{\mathrm{int}}^{+}$ and $\delta w_{\mathrm{ext}}^{-}$, as

$$\delta \boldsymbol{W}_{\mathrm{in}} = \begin{pmatrix} \delta \boldsymbol{w}_{\mathrm{int}}^{+} \\ \delta w_{\mathrm{ext}}^{-} \end{pmatrix}. \tag{4.29}$$

If the wave of $\delta \boldsymbol{W}_{\mathrm{in}}$ grows along with time, the generator becomes unstable. From Equations (4.4), (4.24) and (4.29) the relation between $\delta \boldsymbol{W}_{\mathrm{in}}$, $\delta \boldsymbol{U}_{\mathrm{int}}$ and $\delta \boldsymbol{I}$ is given by

$$\delta \boldsymbol{W}_{\text{in}} = \begin{pmatrix} \mathrm{O} \\ \boldsymbol{l}_{\text{ext}}^{-} \dfrac{\partial \boldsymbol{U}_{\text{ext}}}{\partial \boldsymbol{I}} \end{pmatrix} \delta \boldsymbol{I} + \begin{pmatrix} \boldsymbol{L}_{\text{int}}^{+} \\ \boldsymbol{l}_{\text{ext}}^{-} \dfrac{\partial \boldsymbol{U}_{\text{ext}}}{\partial \boldsymbol{U}_{\text{int}}} \end{pmatrix} \delta \boldsymbol{U}_{\text{int}}. \tag{4.30}$$

4.4.2 Linear Stability Analysis of Channel-Length Scale

The equation for perturbations $\delta \boldsymbol{I}$, $\delta \boldsymbol{U}_{\text{int}}$ and $\delta \boldsymbol{W}_{\text{in}}$ is derived from Equation(4.5) (the loading condition), Equations (4.6) and (4.7) (boundary conditions), and Equations (4.4) and (4.30) as follows:

$$\begin{pmatrix} \boldsymbol{A}_{11} & \boldsymbol{A}_{12} & \mathrm{O} \\ \boldsymbol{A}_{21} & \boldsymbol{A}_{22} & \mathrm{O} \\ -\boldsymbol{A}_{31} & -\boldsymbol{A}_{32} & \mathbf{1} \end{pmatrix} \begin{pmatrix} \delta \boldsymbol{I} \\ \delta \boldsymbol{U}_{\text{int}} \\ \delta \boldsymbol{W}_{\text{in}} \end{pmatrix} = 0 \tag{4.31}$$

$$\boldsymbol{A}_{11} = \frac{\partial \boldsymbol{V}_{\text{gen}}}{\partial \boldsymbol{I}} - \frac{\partial \boldsymbol{V}_{\text{load}}}{\partial \boldsymbol{I}}, \ \boldsymbol{A}_{12} = \frac{\partial \boldsymbol{V}_{\text{gen}}}{\partial \boldsymbol{U}_{\text{int}}} \tag{4.32}$$

$$\boldsymbol{A}_{21} = \begin{pmatrix} \mathrm{O} \\ \dfrac{\partial \boldsymbol{b}_{\text{ext}}}{\partial \boldsymbol{U}_{\text{ext}}} \dfrac{\partial \boldsymbol{U}_{\text{ext}}}{\partial \boldsymbol{I}} \end{pmatrix}, \ \boldsymbol{A}_{22} = \begin{pmatrix} \dfrac{\partial \boldsymbol{b}_{\text{int}}}{\partial \boldsymbol{U}_{\text{int}}} \\ \dfrac{\partial \boldsymbol{b}_{\text{ext}}}{\partial \boldsymbol{U}_{\text{ext}}} \dfrac{\partial \boldsymbol{U}_{\text{ext}}}{\partial \boldsymbol{U}_{\text{int}}} \end{pmatrix} \tag{4.33}$$

$$\boldsymbol{A}_{31} = \begin{pmatrix} \mathrm{O} \\ \boldsymbol{l}_{\text{ext}}^{-} \dfrac{\partial \boldsymbol{U}_{\text{ext}}}{\partial \boldsymbol{I}} \end{pmatrix}, \ \boldsymbol{A}_{32} = \begin{pmatrix} \boldsymbol{L}_{\text{int}}^{+} \\ \boldsymbol{l}_{\text{ext}}^{-} \dfrac{\partial \boldsymbol{U}_{\text{ext}}}{\partial \boldsymbol{U}_{\text{int}}} \end{pmatrix} \tag{4.34}$$

where differentials of $\boldsymbol{U}_{\text{ext}}$ and $\boldsymbol{V}_{\text{gen}}$ with respect to $\boldsymbol{U}_{\text{int}}$ or $\boldsymbol{I}$ are given by integration of the variational equation (3.13) in similar ways to those described Subsection 3.3.2.1 and Subsection 3.6.1. In the case of the constant current loading condition, the following equation is substituted for Equation (4.32) :

$$\boldsymbol{A}_{11} = \mathbf{1}\ , \ \boldsymbol{A}_{12} = \mathbf{0}. \tag{4.35}$$

The elimination of $\delta \boldsymbol{U}_{\text{int}}$ from Equation (4.31) gives

$$\begin{pmatrix} \boldsymbol{A}_{11} - \boldsymbol{A}_{12}\boldsymbol{A}_{32}^{-1}\boldsymbol{A}_{31} & \boldsymbol{A}_{12}\boldsymbol{A}_{32}^{-1} \\ \boldsymbol{A}_{21} - \boldsymbol{A}_{22}\boldsymbol{A}_{32}^{-1}\boldsymbol{A}_{31} & \boldsymbol{A}_{22}\boldsymbol{A}_{32}^{-1} \end{pmatrix} \begin{pmatrix} \delta \boldsymbol{I} \\ \delta \boldsymbol{W}_{\text{in}} \end{pmatrix} = 0. \tag{4.36}$$

The perturbations increase when the time growth rate s satisfies

$$\begin{aligned} \Delta(s) &= \det(\begin{pmatrix} \boldsymbol{A}_{11} - \boldsymbol{A}_{12}\boldsymbol{A}_{32}^{-1}\boldsymbol{A}_{31} & \boldsymbol{A}_{12}\boldsymbol{A}_{32}^{-1} \\ \boldsymbol{A}_{21} - \boldsymbol{A}_{22}\boldsymbol{A}_{32}^{-1}\boldsymbol{A}_{31} & \boldsymbol{A}_{22}\boldsymbol{A}_{32}^{-1} \end{pmatrix}) \\ &= \det(\begin{pmatrix} \boldsymbol{A}_{11} & \boldsymbol{A}_{12} \\ \boldsymbol{A}_{21} & \boldsymbol{A}_{22} \end{pmatrix})/\det(\boldsymbol{A}_{32}) = 0 \end{aligned} \tag{4.37}$$

and

$$\mathrm{Re}(s) > 0. \tag{4.38}$$

We can judge whether or not $\Delta(s)$ has a zeropoint which satisfies Equation (4.38) by the locus $\Delta(\mathrm{j}\omega)(\omega : -\infty \to \infty)$ in a similar way to the supersonic case in Subsection 3.3.3. The generator is unstable if the origin exists on the right-hand side of the locus $\Delta(\mathrm{j}\omega)(\omega : -\infty \to \infty)$.

4.5 Conceptual Design of MHD Generator

Table 4.1 shows basic specifications of subsonic MHD generators which are analyzed in this chapter. Figure 4.3 shows the distribution of the applied magnetic flux density.

Under the basic specifications mentioned above, the conceptual design of the MHD generators analyzed here are given by determining the distribution of the flow velocity in the duct, Mach number of the channel inlet and the load currents within the limitation of Equations (3.34) and (3.35).

Table 4.1: Basic specifications of MHD generators

Fuel	Chinese Datung Coal
Thermal input	1300 MW
Channel length	15 m
Nozzle length	1 m
Diffuser length	4 m
Number of loads	4
Number of electrodes	600
Channel inlet stagnation pressure	4.5 atm
Channel inlet stagnation temperature	2700 K
Channel exit stagnation pressure	about 1 atm

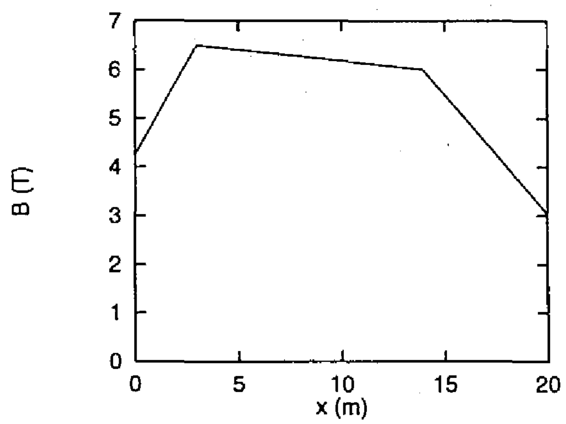

Figure 4.3: Distribution of magnetic flux density

4.6 Stability Analysis of Conventionally Designed MHD Generator

A conventionally designed channel [46] in which the flow velocity is near the sound velocity is examined in this section.

4.6.1 Conventionally Designed MHD Generator

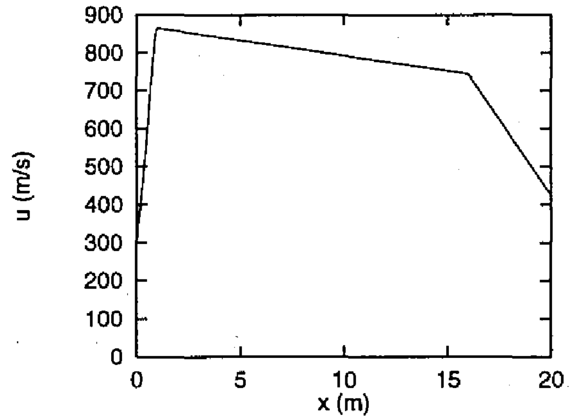

Figure 4.4: Distribution of flow velocity in the conventionally designed generator

The Mach number at the channel inlet is 0.95 and the distribution of velocity is given as in Figure 4.4, where the nozzle region ranges from $x = 0$ to 1 m, the MHD channel from $x = 1$ to 16 m and the diffuser from $x = 16$ to 20 m. The load currents are 11000, 8800, 6800 and 5000 A, respectively. The result of the conceptual design is shown in Table 4.2, Figures 4.5. Figure 4.5 (d) depicts the distribution of the Mach number, which shows that the flow velocity is close to the velocity of sound through the channel.

Table 4.2: Conceptual design of conventional channel

	Channel inlet	Channel exit
Static pressure	2.70 atm	0.63 atm
Static temperature	2532 K	2104 K
Mach number	0.95	0.88
Load currents	11000 8800 6800 5000 A	
Power output	253 MW	
Enthalpy extraction ratio	19.5 %	

4.6.2 Results of Linear Stability Analyses of Channel-Length Scale

Figure 4.6 depicts the locus of $\Delta(\mathrm{j}\omega)(\omega \geq 0)$ under the constant current loading condition when T_s (stagnation temperature), p_s (stagnation pressure) are kept constant at the duct inlet for the inlet boundary condition (4.6), and p_s is kept constant at the duct exit for the exit boundary condition (4.7). In Figure 4.6, (◇) mark indicates the point corresponding to $\omega = 0$. The locus in Figure 4.6 turns clockwise around the origin, which means that the generator is unstable. Figure 4.7 shows the locus of $\Delta(\mathrm{j}\omega)(\omega \geq 0)$ under the constant current loading condition when p and T are kept constant at the inlet, and p is constant at the exit. The locus also turns clockwise around the origin indicating that the generator cannot work stably.

Figure 4.8 plots the locus of $\Delta(\mathrm{j}\omega)(\omega \geq 0)$ under the constant voltage loading condition when p_s and T_s are kept constant at the inlet, and p_s is constant at the exit. The locus turns clockwise around the origin and the generator becomes unstable.

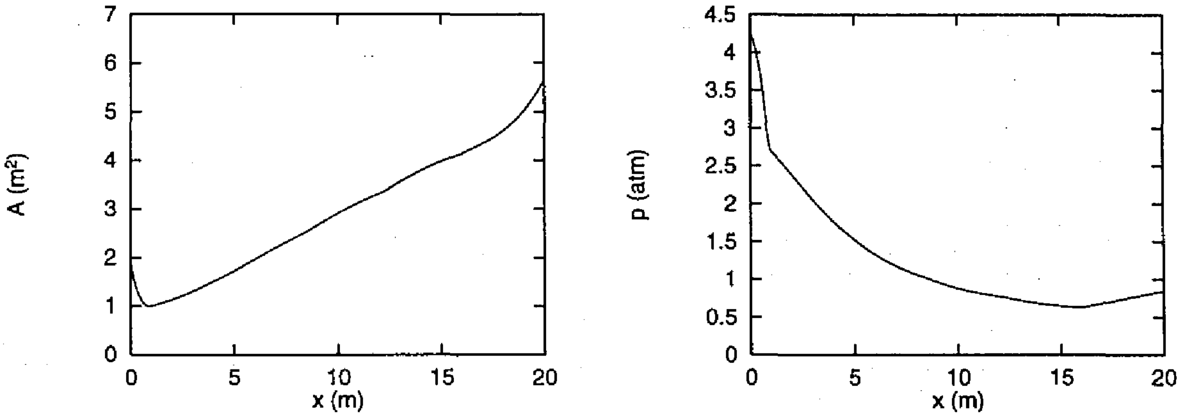

(a) Duct cross section (b) Pressure

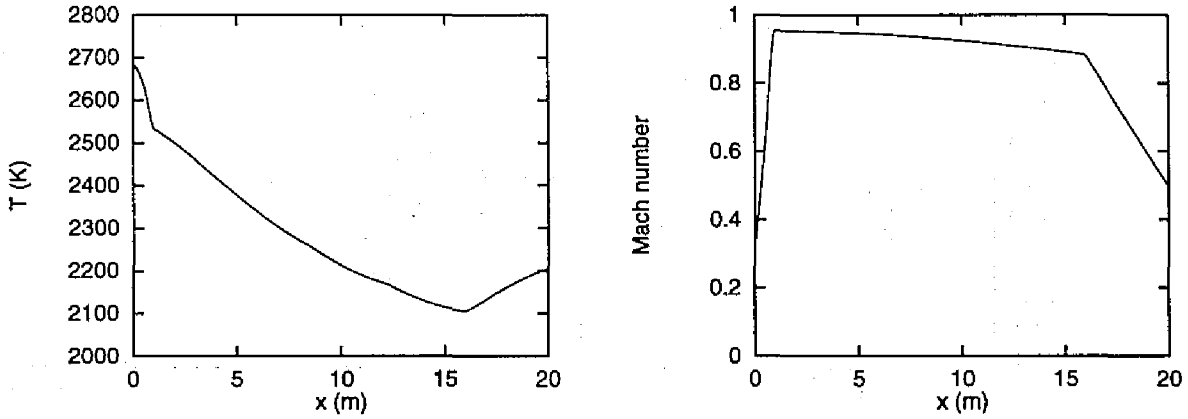

(c) Temperature (d) Mach number

Figure 4.5: Distributions of quantities obtained with design condition of the conventionally designed generator

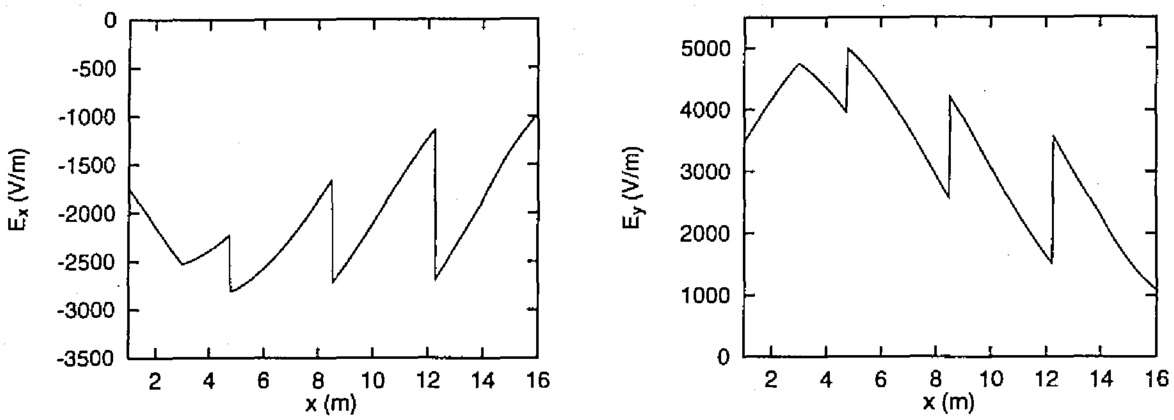

(e) Electric field in x-direction (f) Electric field in y-direction

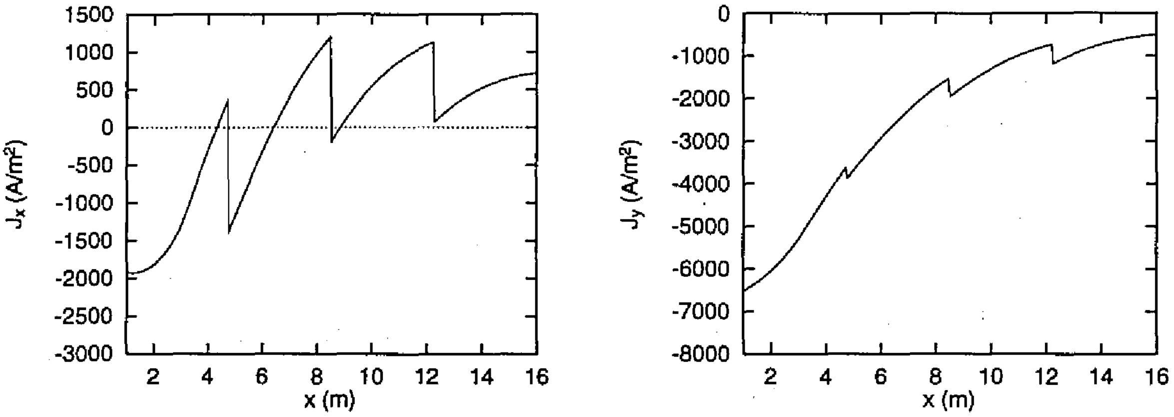

(g) Electric current density in x-direction (h) Electric current density in y-direction

Figure 4.5: Distributions of quantities obtained with design condition of the conventionally designed generator

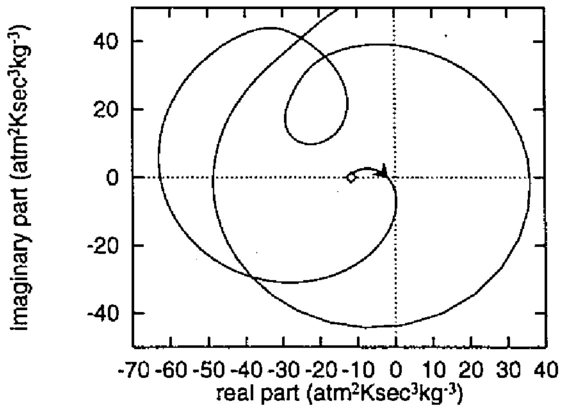

Figure 4.6: Locus of $\Delta(j\omega)(\omega \geq 0)$ under constant current loading condition when T_s, p_s are kept constant at inlet and p_s is kept constant at exit (conventionally designed MHD generator)

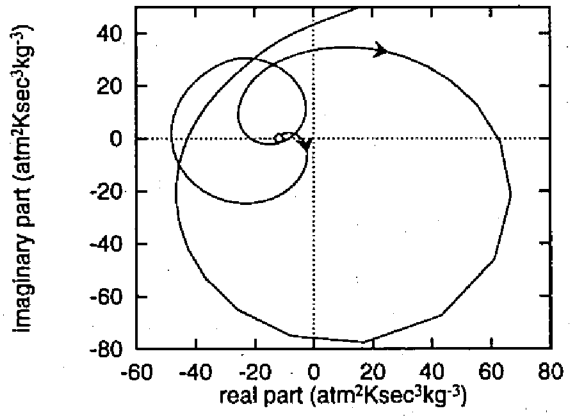

Figure 4.7: Locus of $\Delta(j\omega)(\omega \geq 0)$ under constant current loading condition when T, p are kept constant at inlet and p is kept constant at exit (conventionally designed MHD generator)

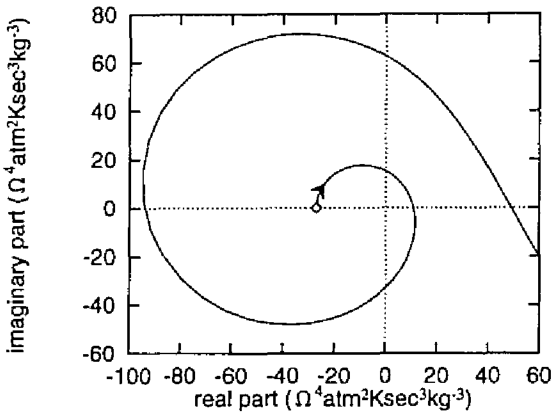

Figure 4.8: Locus of $\Delta(j\omega)(\omega \geq 0)$ under constant voltage loading condition when T_s, p_s are kept constant at inlet and p_s is kept constant at exit (conventionally designed MHD generator)

4.6.3 Results of Time-Dependent Calculations

Time-dependent calculations are carried out to confirm the linear stability analysis of channel-length scale. Figure 4.9 shows the time-dependent distribution of Mach number, when p_s and T_s are kept constant at the duct inlet, and p_s is kept constant at the duct exit. In this case, a shock wave occurs in the channel and the generator becomes unstable. Figure 4.10 shows the time-dependent distribution of Mach number under the constant voltage loading condition, when p_s and T_s are kept constant at the inlet, and p_s is kept constant at the exit. The MHD generator also becomes unstable under the constant voltage loading condition.

Table 4.3 lists results of the linear stability analyses and the time-dependent calculations for the conventional generator under various boundary conditions and loading conditions. Both the linear stability analyses and time-dependent calculations show that the conventionally designed channel tends to be unstable. The condition "fixed electrode currents" in Table 4.3 means that the electrode currents are fixed by setting the link inductance $L_{link} \to \infty$. Table 4.3 shows that the MHD generator can be operated stably if the electrode currents are fixed. This result suggests that severe control of electrode current is required for stabilizing the conventional subsonic MHD generator whose flow velocity is near the sound velocity.

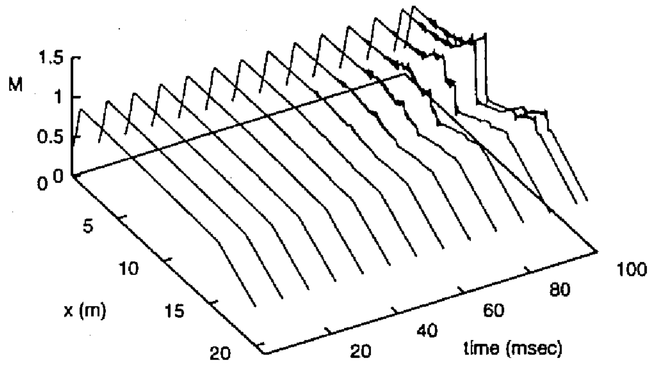

Figure 4.9: Time-dependent distribution of Mach number in the conventionally designed generator with constant current loads

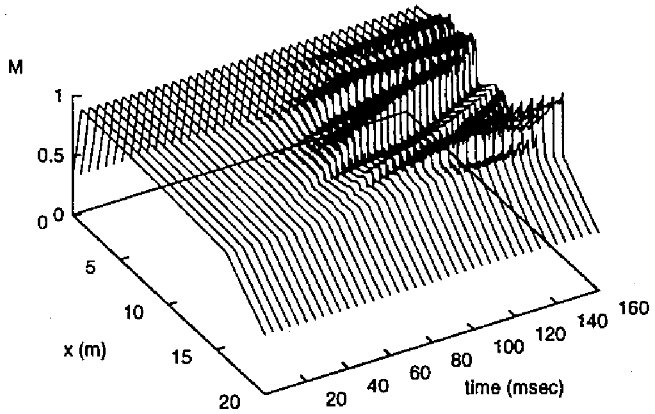

Figure 4.10: Time-dependent distribution of Mach number in the conventionally designed generator with constant voltage loads

Table 4.3: Results of linear stability analyses and time-dependent calculations for conventionally designed channel

Inlet condition	Exit condition	Loading condition	Linear stability	Time-dependent calculation	
p_s,T_s constant	p_s constant	constant current	unstable	unstable	
p,T constant	p constant	constant current	unstable	unstable	
p,T constant	p constant	constant voltage	unstable	unstable	
p_s,T_s constant	p_s constant	constant current	stable	stable	electrode current fixed

4.7 Newly Designed Channel to Suppress Instability of Magneto-Acoustic Waves

The preceding section shows that a conventionally designed channel is apt to be unstable. Figure 4.11 plots the stability index (local growth rate) of the three waves along the conventionally designed channel. Since the stability index does not depend on the wavelength of the perturbation when the wavelength is sufficiently large $^{26)}$, Figure 4.11 shows the stability index with k (wavelength)=10 m^{-1}. Figure 4.11 indicates that the $(u - a)$ wave has a large growth rate and causes the instability in the conventionally designed channel.

Equation (4.14) shows that increasing the wave velocity can reduce the growth rate of the wave. This means that the growth of $(u - a)$ wave is suppressed by designing the channel where $|u - a|$ becomes large, i.e., the flow velocity is kept low. On the other hand, if the flow velocity is too low, the electromotive force decreases and thus the generator cannot yield sufficient power output. Consequently, when the distribution of the flow velocity is determined in the design of subsonic MHD generators, it follows that both the stability and the power output should be taken into account.

We then design the new channel in which the Mach number is relatively low and the velocity of $(u - a)$ wave is relatively large.

The Mach number at the channel inlet is set to be 0.8 and the distribution of velocity is determined as is shown in Figure 4.12. The load currents are chosen to

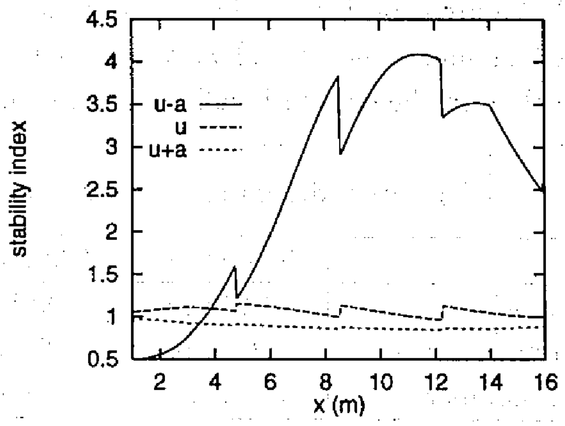

Figure 4.11: Stability index along the conventionally designed channel

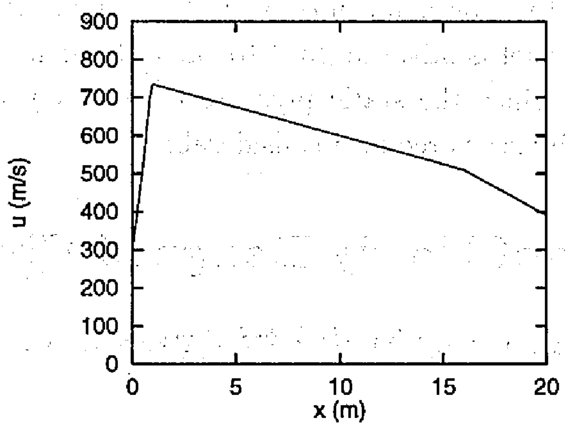

Figure 4.12: Distribution of flow velocity in the newly designed MHD generator

be 14000, 10500, 9000 and 7000 A, respectively. The result of conceptual design is obtained as is shown in Table 4.4 and Figures 4.13. Figure 4.13 (d) shows that the generator has lower Mach number than the conventionally designed generator analyzed in Section 4.6. Figure 4.14 depicts the stability index of the three waves along the newly designed channel. The $(u-a)$ wave has a lower growth rate in the newly designed channel than in the conventionally designed channel.

Table 4.4: Conceptual design of the new channel

	Channel inlet	Channel exit
Static pressure	3.12 atm	0.81 atm
Static temperature	2580 K	2196 K
Mach number	0.80	0.60
Load currents	14000 10500 9000 7000 A	
Load voltages	6120 7187 5859 5294 V	
Load resistances	0.437 0.685 0.651 0.756 Ω	
Power output	251 MW	
Enthalpy extraction ratio	19.3 %	

While this new channel has low flow velocity, its gas conductivity is high because of the high static temperature (see Figure 4.13 (c)), compared with the conventional channel. As a result, the power outputs of both channels are almost the same. Moreover, the new channel is advantageous to the diffuser from the view point of the pressure recovery. Since the static pressure is relatively high at the channel exit, the load on the diffuser is reduced considerably.

4.8 Stability of Newly Designed Channel

4.8.1 Results of Linear Stability Analysis of Channel-Length Scale

Figure 4.15 shows the locus of $\Delta(j\omega)(\omega \geq 0)$ with the constant current loads when T_{sint}, p_{sint} and p_{sext} are kept constant for the inlet and exit boundary conditions, where T_{sint} is the stagnation temperature of the duct inlet, p_{sint} is the stagnation pressure of the duct inlet and p_{sext} is the stagnation pressure of the duct exit,

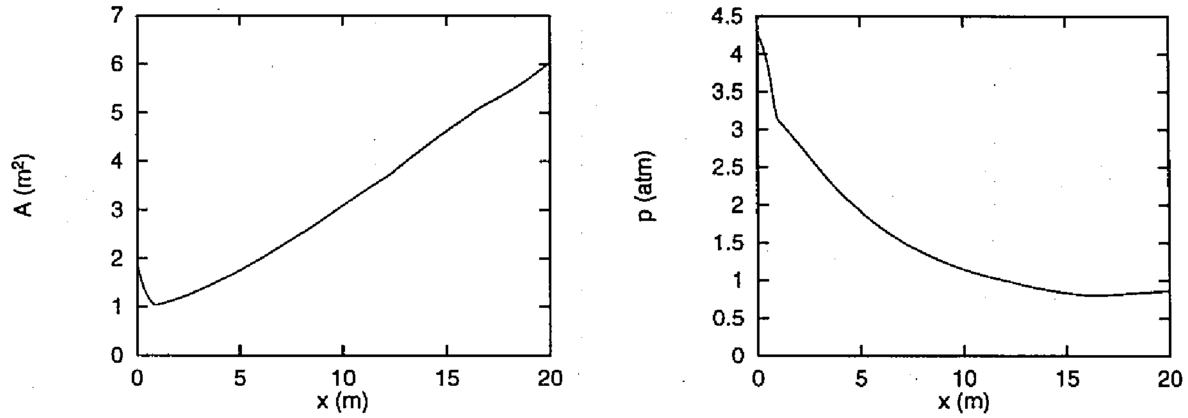

(a) Duct cross section

(b) Pressure

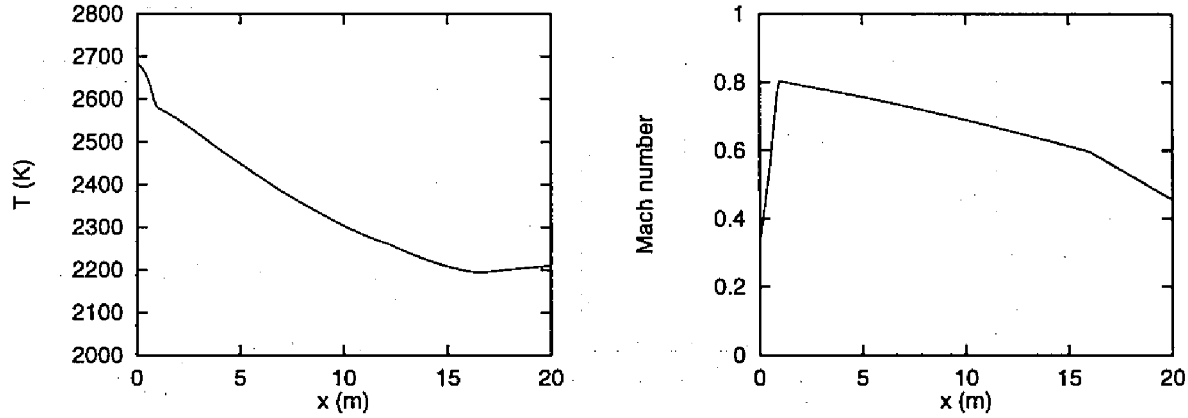

(c) Temperature

(d) Mach number

Figure 4.13: Distributions of quantities obtained with design condition of the newly designed generator

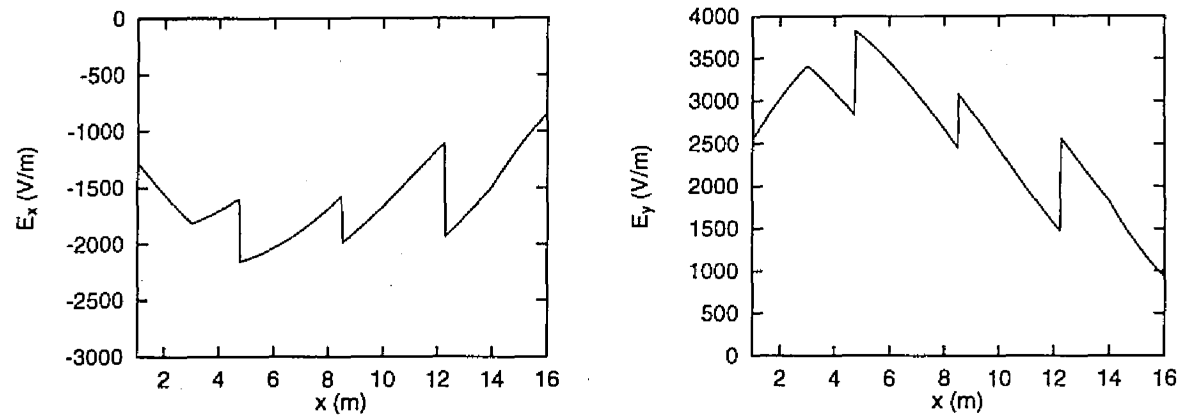

(e) Electric field in x-direction (f) Electric field in y-direction

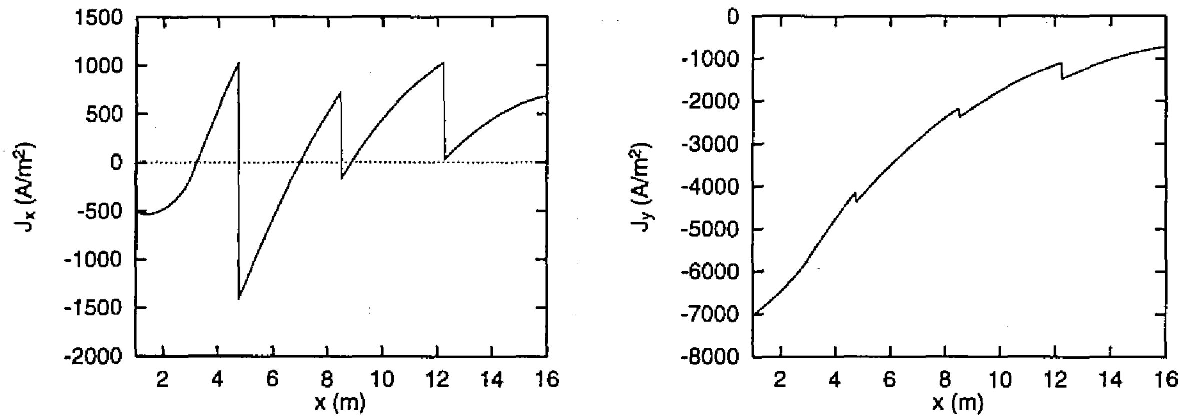

(g) Electric current density in x-direction (h) Electric current density in y-direction

Figure 4.13: Distributions of quantities obtained with design condition of the newly designed generator

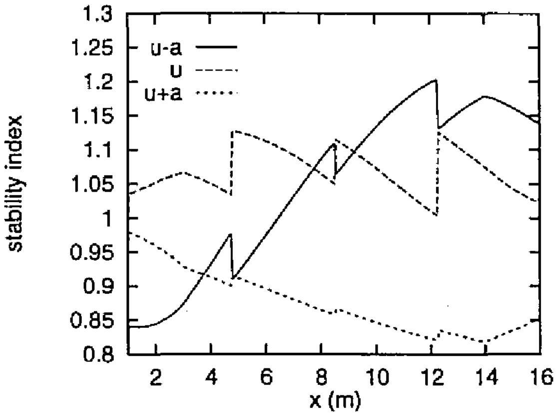

Figure 4.14: Stability index along the newly designed channel

respectively. In Figure 4.15 the origin is in the left-hand side of the locus indicating that the generator is stable.

Figure 4.16 depicts the locus of $\Delta(\mathrm{j}\omega)(\omega \geq 0)$ with the constant current loads when p and T are kept constant at the duct inlet, and p is kept constant at the duct exit. Figure 4.16 shows that the generator is also stable.

Figure 4.17 plots the locus of $\Delta(\mathrm{j}\omega)(\omega \geq 0)$ under the constant voltage loading condition when T_{sint}, p_{sint} and p_{sext} are kept constant. In Figure 4.17, the origin stays on the left-hand side of the locus, and thus the generator is stable. Figure 4.18 shows the locus of $\Delta(\mathrm{j}\omega)(\omega \geq 0)$ under the ohmic loading condition when T_{sint}, p_{sint} and p_{sext} are kept constant. The origin is on the left-hand side of the locus in Figure 4.18 indicating that the generator is stable.

4.8.2 Results of Time-Dependent Calculations

Figure 4.19 shows the time-dependent distribution of Mach number with the constant current loads, when p_{s} and T_{s} are kept constant at the inlet, and p_{s} is kept constant at the exit. The generator works stably in this case. Figures 4.20 depicts the time-dependent distribution of Mach number with the constant voltage loads and the ohmic loads, respectively. The generator also behaves stably with the constant voltage loads and the ohmic loads.

Table 4.5 lists results of the linear stability analysis and the time-dependent calculation for the newly designed generator under various boundary conditions. In table 4.5, "L+constant voltage" means the constant voltage loads with series

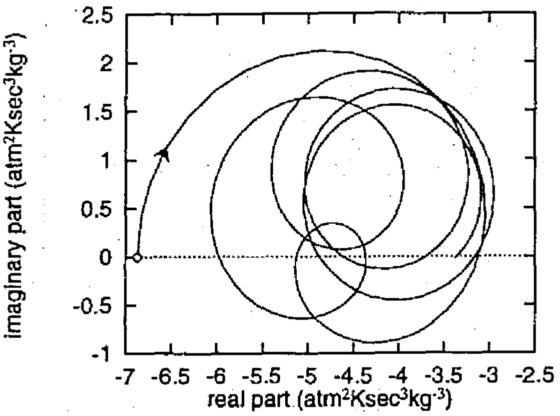

Figure 4.15: Locus of $\Delta(j\omega)(\omega : 0 \rightarrow 200)$ of the newly designed generator with constant current loads when $p_{\rm sint}$, $T_{\rm sint}$ and p_{sext} are kept constant

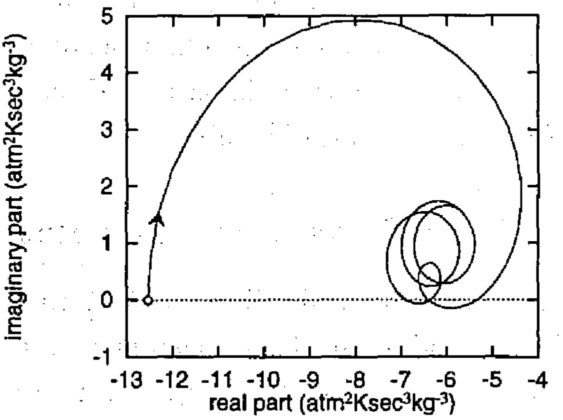

Figure 4.16: Locus of $\Delta(j\omega)(\omega : 0 \rightarrow 300)$ of the newly designed generator with constant current loads when p, T are kept constant at inlet and p is kept constant at exit

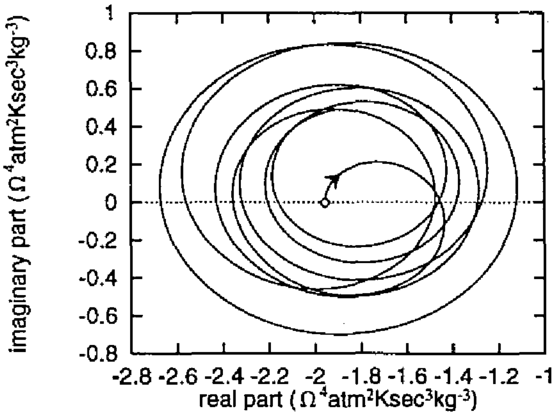

Figure 4.17: Locus of $\Delta(j\omega)(\omega \geq 0)$ of the newly designed generator with constant voltage loads when p_{sint}, T_{sint} and p_{sext} are kept constant

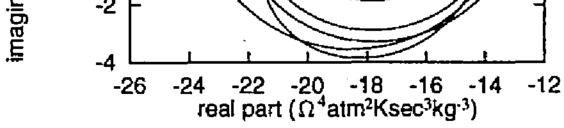

Figure 4.18: Locus of $\Delta(j\omega)(\omega \geq 0)$ of the newly designed generator with ohmic loads when p_{sint}, T_{sint} and p_{sext} are kept constant

Table 4.5: Results of linear stability analyses and time-dependent calculations for the newly designed generator

Inlet condition	Exit condition	Loading condition	Linear stability analysis	Time-dependent calculations
p_s, T_s constant	p_s constant	constant current	stable	stable
p_s, T_s constant	p_s constant	L(30mH) + constant voltage	stable	stable
p_s, T_s constant	p_s constant	L(100mH) + constant voltage	stable	stable
p, T constant	p constant	constant current	stable	stable
p, T constant	p constant	constant voltage	stable	stable
p, T constant	p constant	ohmic loads	stable	stable

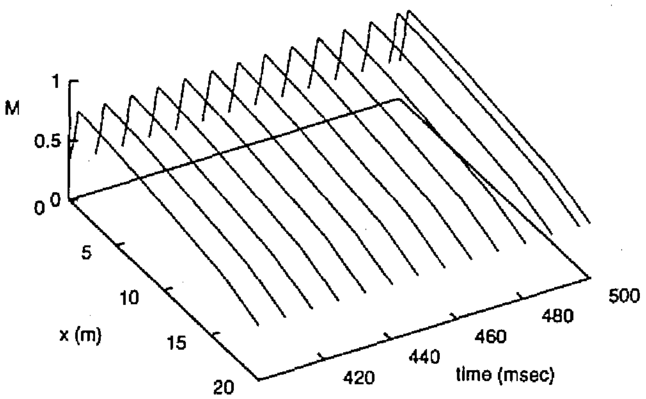

Figure 4.19: Time-dependent distribution of Mach number in the newly designed generator with constant current loads when p_{sint}, T_{sint} and p_{sext} are kept constant

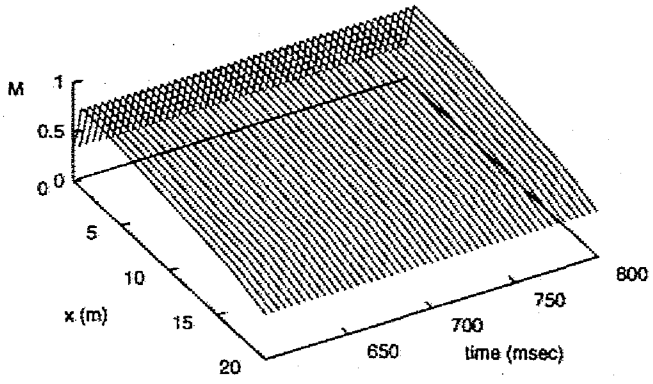

(a) Constant voltage loads

Figure 4.20: Time-dependent distributions of Mach number in the newly designed generator with constant voltage loads and ohmic loads

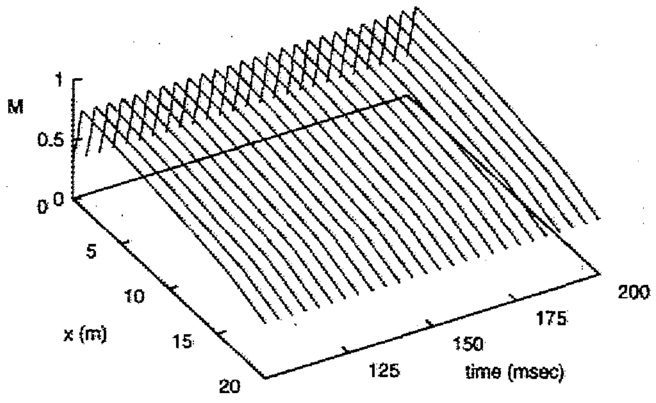

(b) Ohmic loads

Figure 4.20: Time-dependent distributions of Mach number in the newly designed generator with constant voltage loads and ohmic loads

inductors of L mH. Table 4.5 shows that the newly designed channel is stable. In the present analyses, the two following kinds of gasdynamical boundary conditions are adopted. (1) p_s, T_s are constant at the inlet, p_s is constant at the exit. (2) p, T are constant at the inlet, p is constant at the exit. The linear stability analysis of channel-length scale shows that the stability of the generator does not vary between the two boundary conditions. This is because the inlet and exit flow velocities are low, and the stagnation pressure and temperature are not much different from the static pressure and temperature.

4.9 Concluding Remarks

The local linear perturbation analysis and the linear stability analysis of channel-length scale are carried out for subsonic diagonal type MHD generators.

At first, the stability of the conventionally designed generator is examined. The linear stability analyses and the time-dependent calculation show that the conventionally designed generator tends to be unstable.

Then the author designs the new channel in which the Mach number is relatively low in order to suppress the instability. The author also examines the stability of the newly designed generator and the main results are listed below:

- In spite of the low flow velocity, the newly designed generator yields almost the same power output as the conventionally designed generator because of high electrical conductivity resulting from the high temperature of working gas.
- The local perturbation analysis shows that the low flow velocity suppresses the growth of traveling waves in the new channel.
- The linear stability analysis of channel-length scale and time-dependent calculations show that the newly designed generator works stably.

Chapter 5 Stability Analysis of Faraday Type MHD Generator

5.1 Introduction

In this chapter, a subsonic Faraday type MHD generator of commercial scale is analyzed. M. Ishikawa and A. Kyogoku et al. examined the stability of Faraday type MHD generators of commercial scale, showing that the generator can be operated stably with ohmic loads while the generator becomes unstable with constant loading factors [46]. In this chapter, a local linear perturbation analysis and a linear stability analysis of channel-length scale are carried out for a subsonic Faraday type MHD generator. These analyses show the generator is operated stably with constant current loads, constant voltage loads or ohmic loads. On the other hand, the generator is unstable when the loading factors are fixed or when each load power is kept constant.

5.2 Basic Equations

The basic equations used for the gasdynamical part are the same as the equations used in the analysis for the diagonal type MHD generators. The flow in the MHD channel is described by Equation (3.1) and the state equations are given by Equation (3.5). The steady state flow is described by Equation (3.6).

The relation between the electric field and the electric current density is given by the generalized Ohm's law (3.7), (3.8), by the loading condition described below and by the following equation of leakage in the x-direction:

$$J_x = -\frac{E_x}{R_{leak} w_{chl}}. \tag{5.1}$$

Four types of loading conditions are examined, being written below:
When each loading factor K is kept fixed,

$$E_y = K(uB - \frac{\Delta V}{h_{chl}}). \tag{5.2}$$

When each load resistance R_{load} is kept fixed,

$$E_y h_{chl} = -R_{load} J_y w_{chl} \Delta x. \tag{5.3}$$

When each load power P_{load} is kept fixed,

$$-E_y J_y w_{chl} h_{chl} \Delta x = P_{load}. \tag{5.4}$$

When each load voltage V_{load} is kept fixed,

$$E_y h_{chl} = V_{load}. \tag{5.5}$$

5.3 Basic Specifications of Subsonic Faraday Type MHD Generator

Table 5.1 lists the basic specifications of subsonic Faraday type MHD generator [46) analyzed here. Figure 5.1 shows the distributions of various quantities under the design condition.

Table 5.1: Basic specifications of subsonic Faraday type MHD generator

Fuel	Chinese Datung Coal	
Seed, Seed fraction	K_2CO_3, 1 %(wt)	
Thermal input	1300 MW	
Channel length	15 m ($1 \le x \le 16$)	
Nozzle length	1 m ($0 \le x \le 1$)	
Diffuser length	4 m ($16 \le x \le 20$)	
	Channel inlet	Channel exit
Static pressure	2.70 atm	0.65 atm
Static temperature	2533 K	2106 K
Stagnation pressure	4.50 atm	0.99 atm
Stagnation temperature	2700 K	2252 K
Mach number	0.95	0.89
Power output	258.7 MW	
Enthalpy extraction ratio	19.9 %	
Loading factor	0.807 (constant along the whole channel)	

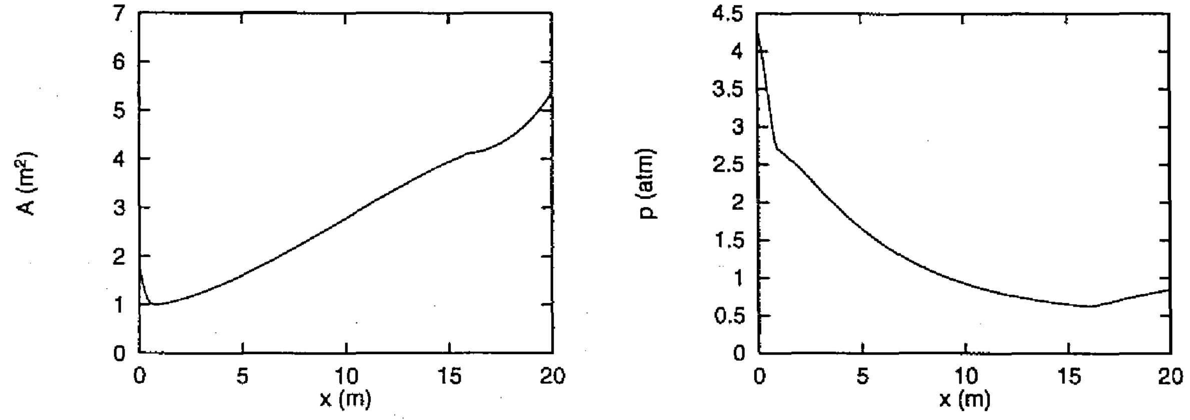

(a) Duct cross section

(b) Pressure

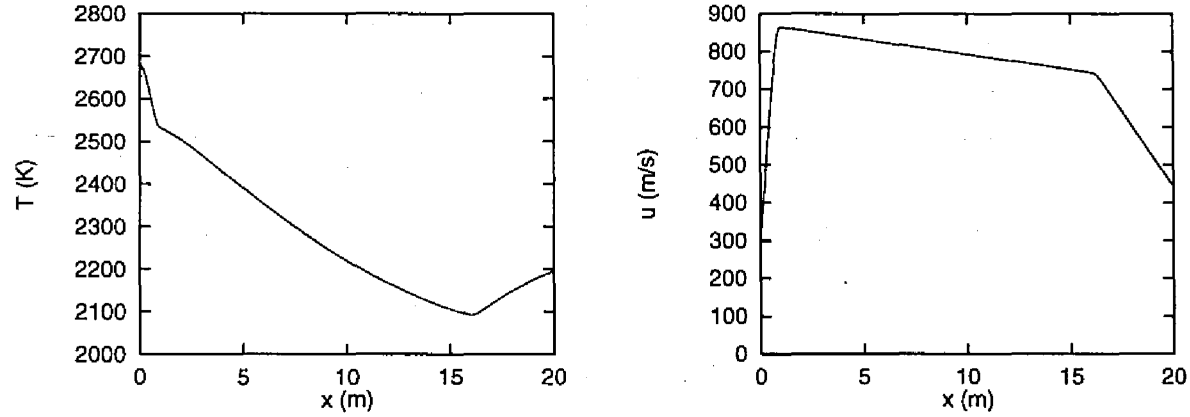

(c) Temperature

(d) Flow velocity

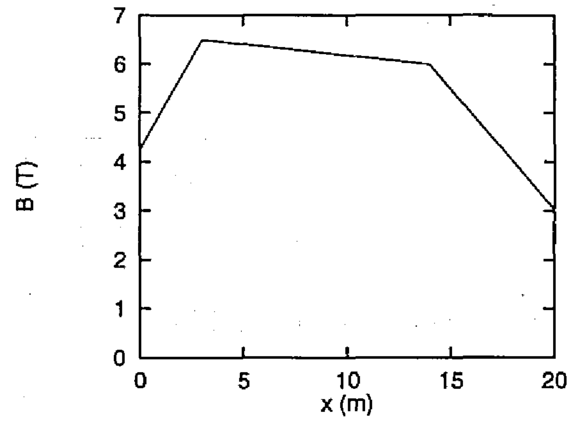

(e) Magnetic flux density

Figure 5.1: Distributions of quantities under design condition

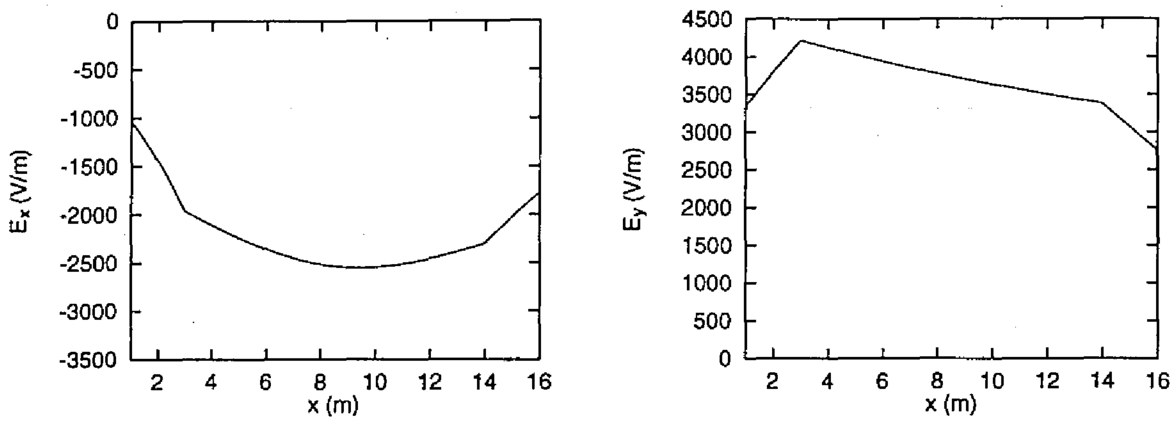

(f) Electric field in x-direction (g) Electric field in y-direction

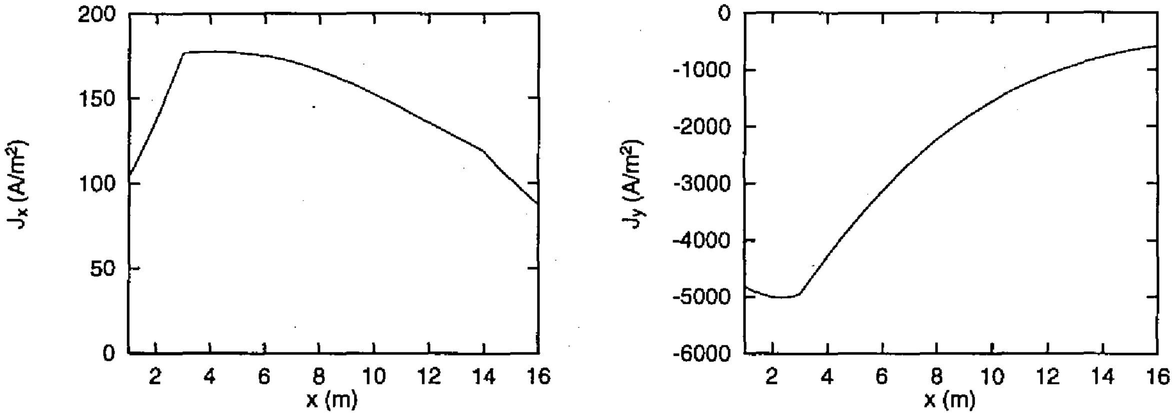

(h) Electric current density in x-direction (i) Electric current density in y-direction

Figure 5.1: Distributions of quantities under design conditions

5.4 Results of Analyses

5.4.1 Local Linear Perturbation Analysis

In this subsection, the local spatial growth rates of traveling waves are shown when the wavelength, k, is set to be 10 m^{-1}. Figure 5.2 shows the stability index(local growth rate) of three traveling waves along the channel with the constant voltage loads. The two acoustic waves, $(u - a)$ wave and $(u + a)$ wave, are stable while the u wave is unstable. The local growth rate of u wave, however, is very small. Figure 5.3 depicts the local growth rates of the waves when each load power is kept constant. Figure 5.3 indicates that u wave is stable while $(u - a)$ wave and $(u + a)$ wave are unstable. In particular, $(u - a)$ wave has a large growth rate in the upstream region.

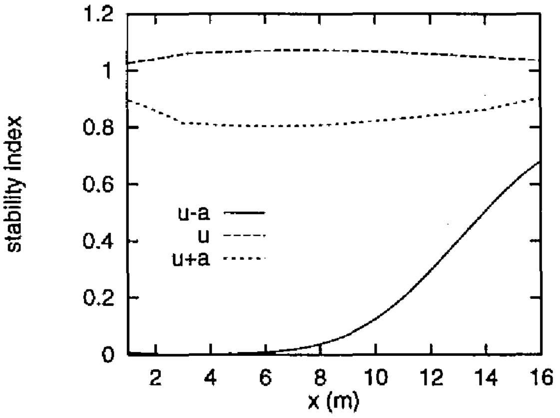

Figure 5.2: Stability index with constant voltage loads

5.4.2 Channel-Length Scale Linear Stability Analysis

A linear stability analysis of channel-length scale for the subsonic Faraday type generator is performed in a similar way to the diagonal channel with constant current loads. In this subsection, p_{sint} and T_{sint} are kept constant for the inlet boundary condition and p_{sext} is kept constant for the exit boundary condition. Figure 5.4 depicts the locus $\Delta(\mathrm{j}\omega)(\omega \geq 0)$ with the ohmic loads. In Figure 5.4, the locus does not turn clockwise around the origin and thus, the generator behaves stably. Figure 5.5 plots the locus $\Delta(\mathrm{j}\omega)(\omega \geq 0)$ with the constant voltage loads. The locus sees the origin in the left-hand side, showing the generator is stable. Figure

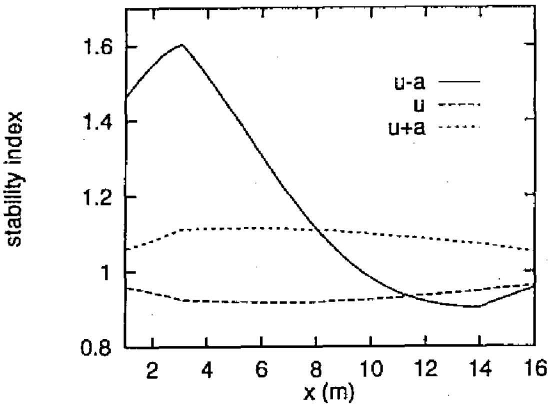

Figure 5.3: Stability index when each load power is kept constant

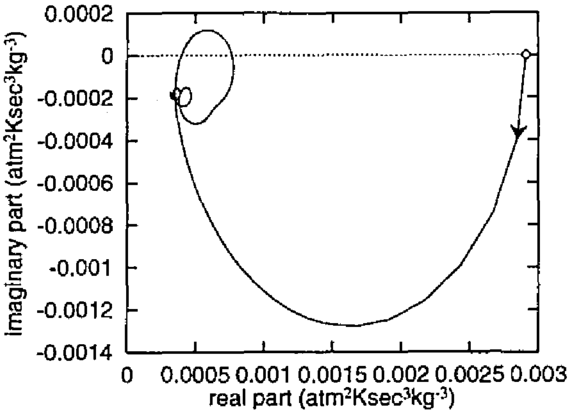

Figure 5.4: Locus of $\Delta(j\omega)(\omega \geq 0)$ with ohmic loads

5.6 shows the locus $\Delta(j\omega)(\omega \geq 0)$ when each load power is kept constant. The locus turns around the origin clockwise, showing the generator becomes unstable.

5.4.3 Time-Dependent Calculation

Time-dependent calculations are performed for confirming the linear stability analysis. Figure 5.7 shows the time-dependent distribution of Mach number with the constant voltage loads, indicating that the generator is stably operated. This calculation result agrees with the result of the linear stability analysis. Figure 5.8 depicts the time-dependent distribution of Mach number when each load power is kept constant. In Figure 5.8, large fluctuations of the flow occurs in the upstream

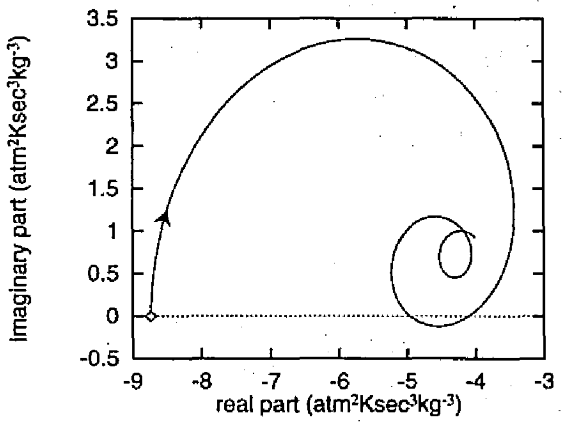

Figure 5.5: Locus of $\Delta(j\omega)(\omega \geq 0)$ with constant voltage loads

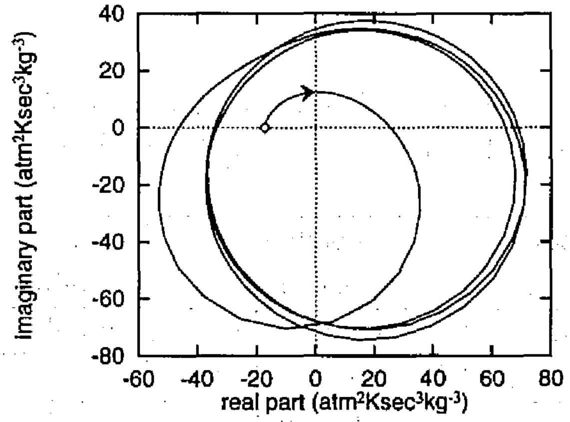

Figure 5.6: Locus of $\Delta(j\omega)(\omega \geq 0)$ when each load power is kept constant

region and a shock wave is induced. This is because the $(u - a)$ wave has a large growth rate in the upstream region as is shown by the local linear perturbation analysis. This instability is also predicted by the channel-length scale linear stability analysis. Table 5.2 summarizes the linear stability analysis of channel-length scale and the time-dependent calculation. The analyses show that the generator with the constant current loads can work stably. The results listed in Table 5.2 agree with the analytical result in Ref. 46).

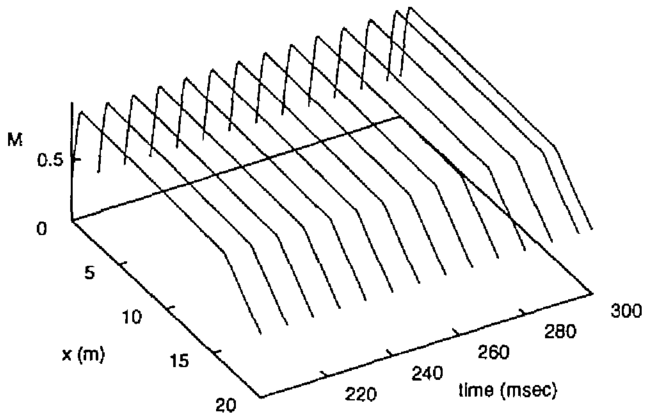

Figure 5.7: Time-dependent distribution of Mach number with constant voltage loads

Table 5.2: Results of linear stability analysis and time-dependent calculation for the subsonic Faraday type generator

Inlet condition	Exit condition	Loading condition	Linear stability	Time-dependent calculation
p_s,T_s constant	p_s constant	ohmic loads	stable	stable
p_s,T_s constant	p_s constant	fixed loading factors	unstable	unstable
p_s,T_s constant	p_s constant	constant voltage	stable	stable
p_s,T_s constant	p_s constant	constant power load	unstable	unstable
p_s,T_s constant	p_s constant	constant current	stable	stable

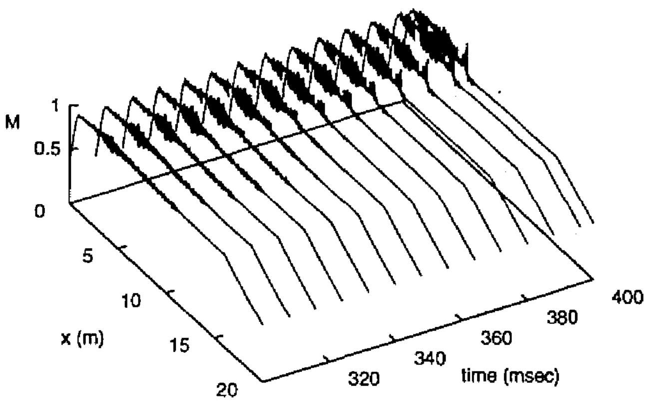

Figure 5.8: Time-dependent distribution of Mach number when each load power is kept constant

5.5 Concluding Remarks

In this chapter, the local linear perturbation analysis, the linear stability analysis of channel-length scale and the time-dependent calculation are carried out for the coal-fired Faraday type MHD generator of commercial-scale. These analyses show the following results.

- The generator is operated stably with constant current loads, constant voltage loads or ohmic loads.
- When each load power is kept constant, the generator becomes unstable because of the large growth of the $(u - a)$ wave in the upstream region.

Chapter 6 Analysis of Interconnecting System of Diagonal-Type MHD Generator and AC Power System

6.1 Introduction

In this chapter, the stability of a subsonic diagonal type MHD generator, connected with an AC power system, is studied. A time-dependent calculation is performed for the interconnecting system of MHD generator and AC power system with 12-phase line-commutated inverters. The calculations show that the generator can provide the rated power to the AC power line under the nominal condition.

Next, the behavior of the interconnecting system with faults in the AC power system is examined. A time-dependent calculation is performed when a firing fault of thyristor occurs. The calculation shows that the MHD generator recovers the nominal condition following the recovery of the inverter operation after the firing fault. The author also analyzes the interconnecting system when line faults occur in a transmission line. The analysis indicates that some control of the firing angle is required for the recovery of the nominal condition of the MHD generation system. The analysis also shows that a control of firing angle recovers the inverter operation, which enables the MHD generator to recover to its nominal condition.

6.2 Basic Equations

The basic equations used for the gasdynamical variables in the MHD channel are the same as the equations used in the analysis in Chapters 3 and 4. The flow in the channel is described by Equation (3.1) and the state equations are given by Equation (3.5).

The relation between the electric field and the electric current density is given by Equations (3.7), (3.8), (3.9) and (3.10) where the diagonal links are assumed to be short-circuited in this chapter.

6.3 Interconnecting System of MHD Generator and AC Power Network

The MHD generator analyzed here is conceptually designed in Chapter 4, and its basic specifications are listed in Table 6.1.

Table 6.1: Basic specifications of the MHD generator

Fuel	Chinese Datung Coal	
Thermal input	1300 MW	
Channel length	15 m	
Nozzle length, Diffuser length	1 m, 4 m	
	Channel inlet	Channel exit
Stagnation temperature	2700 K	2254 K
Static temperature	2580 K	2197 K
Stagnation pressure	4.50 atm	0.98 atm
Static pressure	3.12 atm	0.81 atm
Mach number	0.80	0.60
Power output	251.1 MW	
Enthalpy extraction ratio	19.3 %	
Load current	14000, 10500, 9000, 7000 A	
Load voltage	6120, 7187, 5859, 5294 V	
Load resistance	0.437, 0.685, 0.651, 0.756 Ω	

Figure 6.1 shows the schematic diagram of the interconnecting system of MHD generator and AC power system analyzed here. The MHD generator has four pairs of output terminals which are connected with four 12-phase line-commutated inverters. The outputs of these inverters are supplied to the 3-phase infinite bus through transformers and transmission lines. The rated effective line voltage and frequency of the infinite bus are selected as 275 kV and 60 Hz, respectively. The double-circuit transmission lines are adopted where the impedance of each line is 0.01+j0.1 pu on the basic capacity of 250 MVA and the basic effective line voltage of 275 kV. Each 12-phase line-commutated inverter is connected with a pair of transformers with the same rated values. Table 6.2 lists the rated values of transformers on each loading

section, where the loading sections are numbered from upstream to downstream. The leakage impedance of all transformers is set to be 0.007+0.15 pu based on the rated capacity and voltage of each transformer. The control and margin angles of each inverter are shown in Table 6.3.

The AC filter and the phase modifier are usually equipped on the secondary side of the transformers to absorb the harmonics and the reactive power generated by the line-commutated inverters. In the present model, the 11th filter with a quality factor of 50 and a capacity of 20 MVA, the 13th filter with a quality factor of 50 and a capacity of 17 MVA and high-pass filter (24th) with a quality factor of 3 and capacity of 29 MVA are equipped as the AC filters, while the capacitor with capacity of 100 MVA including 6 % reactors is set as the phase modifier.

The DC reactors are equipped between the MHD generator and the inverters in order to suppress the ripples of DC load currents. The inductance of every reactor is selected as 30 mH.

Table 6.2: Rated values of transformers

	Frequency Hz	Capacity MVA	Voltage kV
1st loading section	60	60	2.75/275
2nd loading section	60	60	3.06/275
3rd loading section	60	40	2.50/275
4th loading section	60	30	2.29/275

Table 6.3: Operation condition of line-commutated inverters

	Firing angle	Overrapping angle	Margin angle
1st loading section	142 °	14.1 °	23.9 °
2nd loading section	145 °	13.0 °	22.0 °
3rd loading section	144 °	13.1 °	22.9 °
4th loading section	145 °	12.6 °	22.4 °

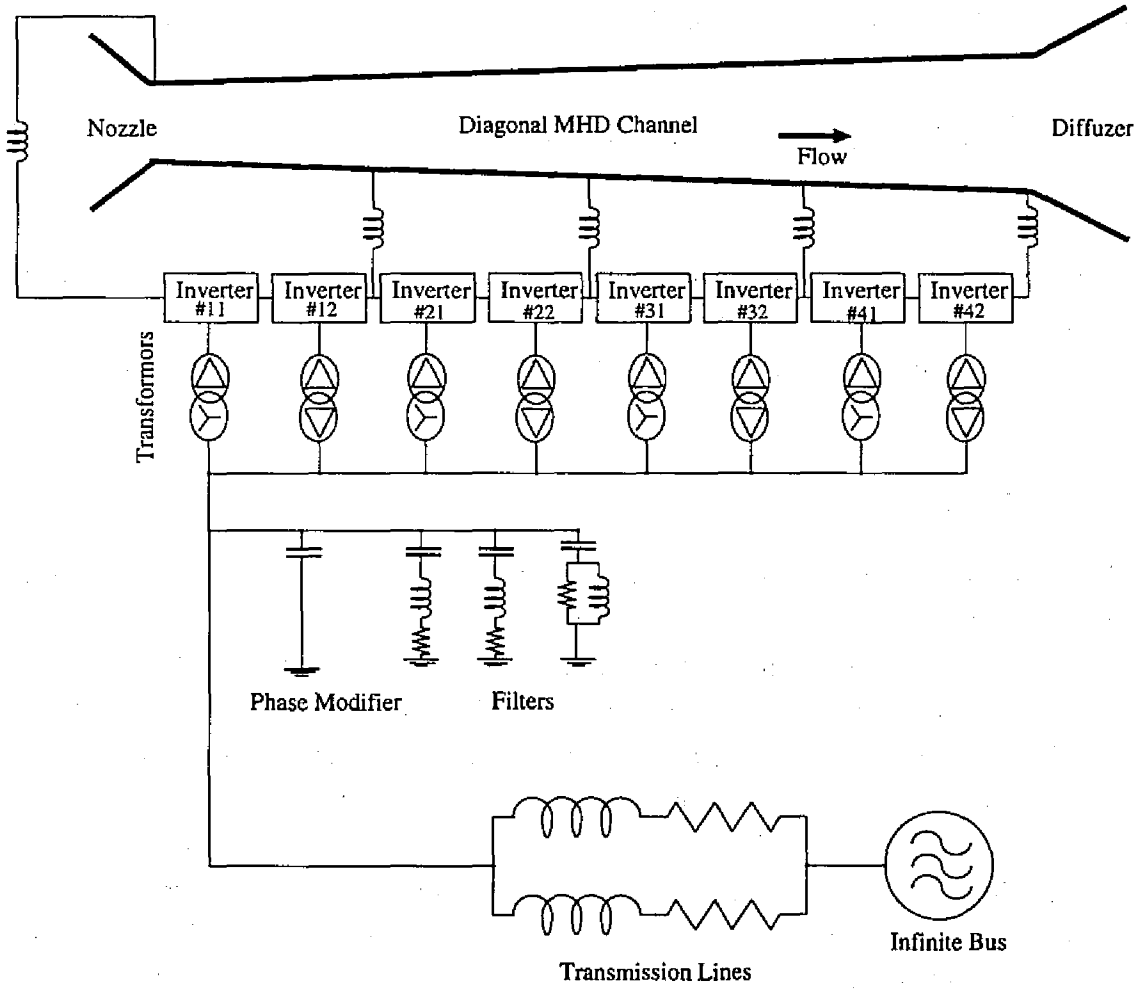

Figure 6.1: Schematic diagram of interconnection system of MHD generator and AC power system

6.4 Numerical Calculation Method

In the present analyses, time-dependent calculations are carried out for the detailed three-phase circuit described in the preceding section. The node voltages and the branch currents are determined by a nodal admittance matrix method [48), while the gasdynamical behavior in the MHD channel is calculated by the 1969 MacCormack two-step explicit method. The detailed procedure is described in Subsection 2.3.1.

6.5 Stability of MHD Generator Connected with AC Power Network

In this section, the MHD generator, connected with AC power network, is analyzed. Here, the inlet stagnation pressure and stagnation temperature are kept constant for the inlet boundary condition, while the exit stagnation pressure is kept constant for the exit boundary condition.

6.5.1 Performance at Nominal Condition

A time-dependent calculation is performed for the interconnecting system of MHD generator and AC power network at the nominal condition. Figure 6.2 shows the three-phase line currents. The wave form of line currents is nearly equal to the sine-wave whose frequency is 60 Hz since the harmonics are removed by the AC filters. A Fourier analysis is also carried out for the line currents in order to evaluate the harmonics. The calculation shows that the DC part is under 0.001 % of the fundamental wave, the 11th harmonic is 1.83 % and the 13th harmonics is 1.17 %. The other harmonics are under 0.1 %. Figure 6.3 plots the three-phase thyristor currents in the inverter #11. Figure 6.3 shows the commutation of the inverter is in the normal condition. Figure 6.4 depicts the active power supplied to the infinite bus through the transmission lines. The active power is 248.9 MW which is almost equal to the rated value where the power factor is 0.98 lead. Figure 6.5 shows the time-dependent variations of load currents of MHD generator. Every load current is maintained to be the rated value where the fluctuation of the current is suppressed under 0.1 % by the DC reactor. Figure 6.6 depicts the time-dependent distribution of the Mach number, indicating that the MHD generator is stably operated, although disturbances are steadily brought into the MHD channel from the inverter system.

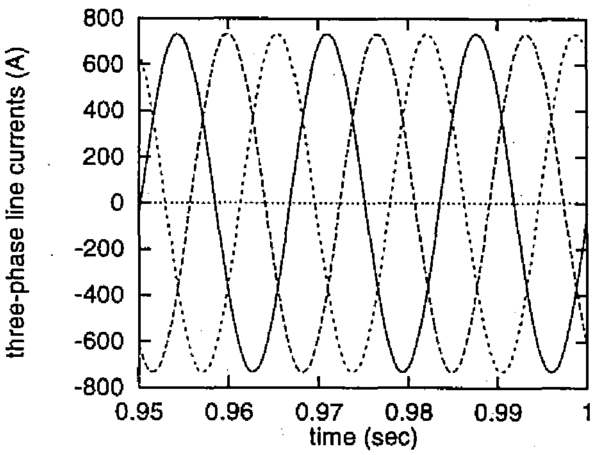

Figure 6.2: Three-phase line currents under nominal condition

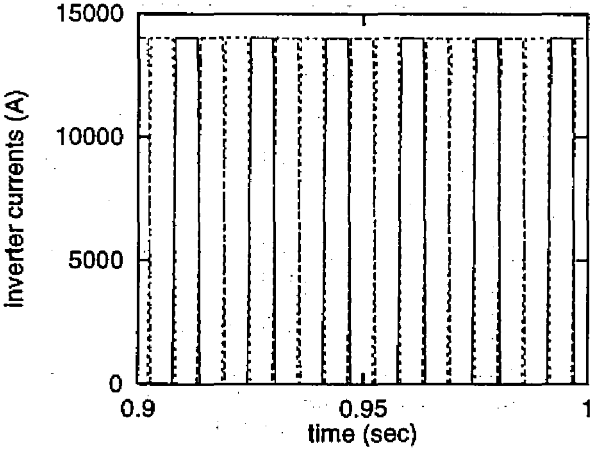

Figure 6.3: Three-phase thyristor currents in inverter #11

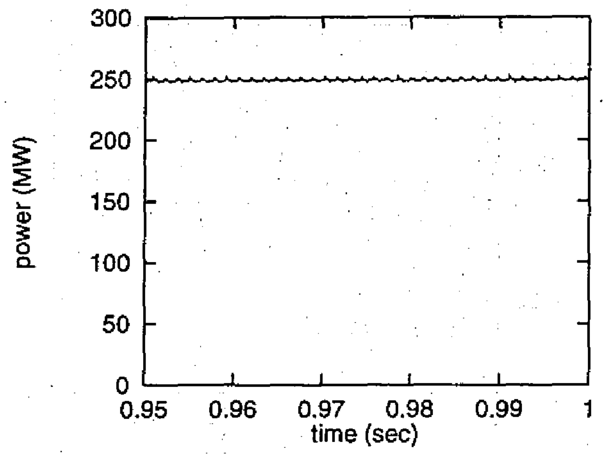

Figure 6.4: Transmission active power under nominal condition

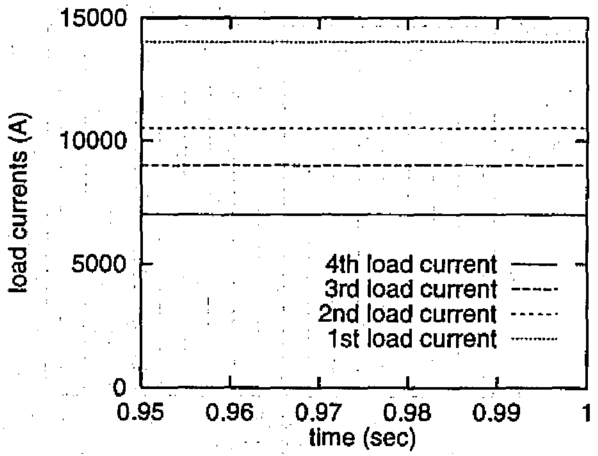

Figure 6.5: Load currents of MHD generator under nominal condition

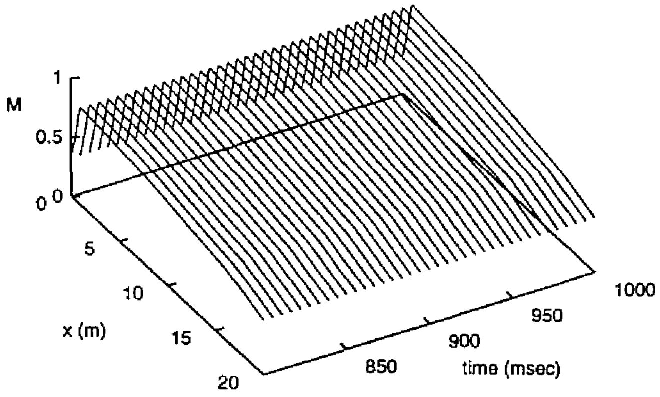

Figure 6.6: Mach number distribution in MHD channel under nominal condition

6.5.2 Performance of MHD Generator When Firing Angles of Inverters Are Changed

In this subsection, the performance of the MHD generator is examined when the firing angles of inverters are changed. Figure 6.7 shows the time-dependent distribution of the Mach number and Figure 6.8 plots the load currents, when the firing angle of each inverter decreases by 10° from the rated value. A shock wave occurs in the generator since the flow is accelerated with the increase of load currents. The shock wave propagates upstream and disappears in the nozzle region, after which the shock waves occur and decay repeatedly. The load currents accordingly fluctuate large. Time-dependent calculations have shown that the MHD generator can be stably operated without any shock wave when the firing angle ranges within -8° and +2° from the rated value. Figure 6.9 depicts the voltage-current characteristics of the loading sections of the MHD generator, showing nearly linear characteristics.

6.6 Fault Analyses

In this section, the interconnecting system is analyzed when faults occur in the inversion system or in the transmission line. When faults occur in the AC power network, large disturbances are induced in the MHD channel. In the subsonic MHD channel, these disturbances propagate upstream and in fact affect the performance

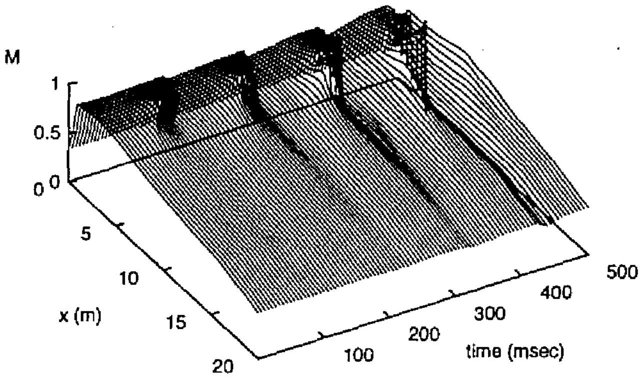

Figure 6.7: Time-dependent distribution of Mach number when firing angle of each inverter decreases by 10° from the rated value

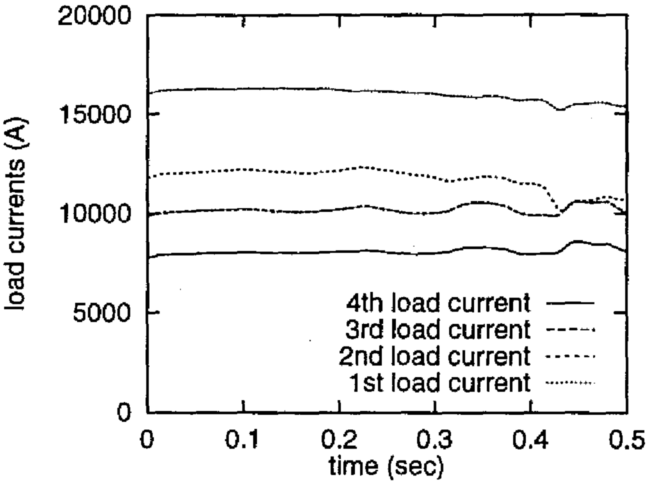

Figure 6.8: Time variation of load currents when firing angle of each inverter decreases by 10° from the rated value

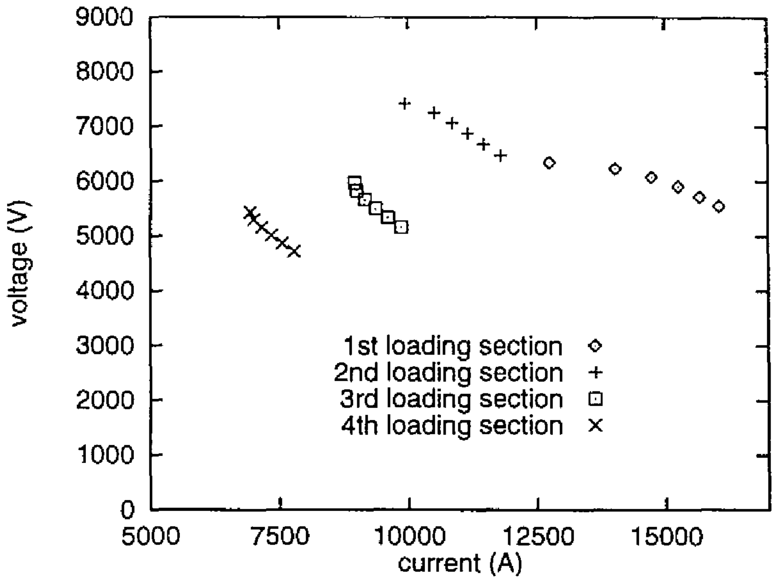

Figure 6.9: Voltage-current characteristics of MHD generator

of the combustor. It is, however, difficult to analyze the system, taking into account the interaction of the MHD generator and the combustor, because the reaction process is complicated in the combustor. In the present fault analysis, the exit condition of the combustor (i.e., the inlet condition of the MHD generator) is assumed to be constant, because the reaction time of the working fluid in the combustor is much longer than the variation time of the flow in the MHD channel.

6.6.1 Firing Fault of Thyristor in Inverter

In this subsection, the author analyzes the case where the firing signal cannot come in the thyristor because of the fault on the control circuit of the firing angle. A firing fault occurs on one of the thyristors in the inverter #41 at $t = 0.002$ sec, after which the commutation of the inverter is restored to the normal condition. Figure 6.10 shows the three-phase thyristor currents in inverter #41 and Figure 6.11 plots the time-dependent variation of the fourth load current. When the firing fault occurs in the inverter, the inverter is short-circuited and the load current increases. Following the recovery of the commutation of the inverter, the load current decreases to the rated value. Figure 6.12 depicts the time-dependent distribution of Mach number in this case. The small disturbance from the faulted loading section propagates upstream, but it decays without inducing a shock wave, after which the flow filed

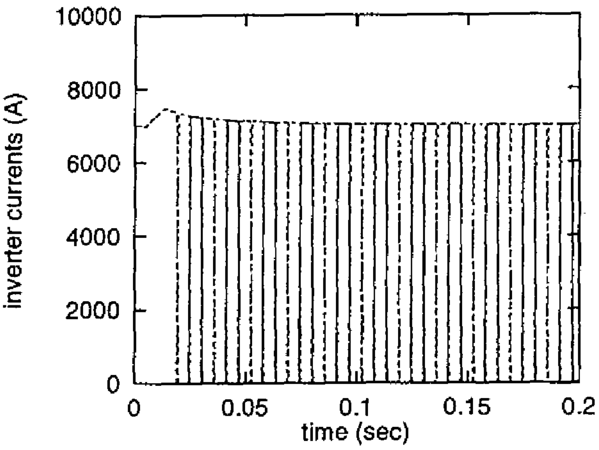

Figure 6.10: Three-phase thyristor currents in inverter #41 when firing fault occurs on inverter #41

in the MHD generator is restored to the nominal condition.

6.6.2 Single-Line Ground Fault

In this subsection, the interconnecting system of MHD generator and AC power network is analyzed when a single-line ground fault occurs at the center of the transmission line. In the present analysis, the single-line ground fault occurs at $t = 0.05$ sec and the fault line is cut off at $t = 0.2$ sec, i.e., at 9 AC cycles after the ground fault. The system is analyzed when the firing angles of all the inverters are kept constant at the rated values. Figure 6.13 shows the time-dependent variation of three-phase line voltages of the secondary side of transformers. Figure 6.14 depicts the time-dependent variation of load currents of the MHD generator. Figures 6.15 shows the time-dependent distribution of the Mach number in the MHD generator. Figure 6.16 plots the time-dependent variation of three-phase thyristor currents in the inverter #11. When the ground fault occurs, the voltage of the faulted line decreases to about one third of its rated value as shown in Figure 6.13. Since the line voltage decreases by large amount, inverters are short-circuited and load currents increase as shown in Figure 6.14. Since the Lorentz force J_yB is weakened due to the increase of load currents, the flow is accelerated and a shock wave is induced in the MHD channel. The shock wave propagates upstream and disappears in the nozzle region, after which the low flow-velocity region appears in the entire channel. After the faulted line is cut off at t =0.2 sec, the line voltage recovers

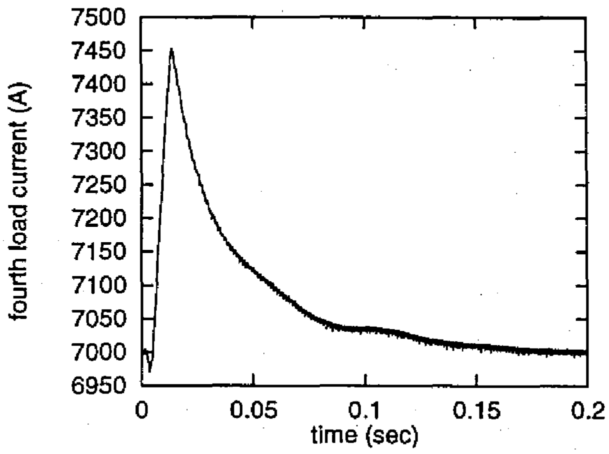

Figure 6.11: Fourth load current when firing fault occurs on inverter #41

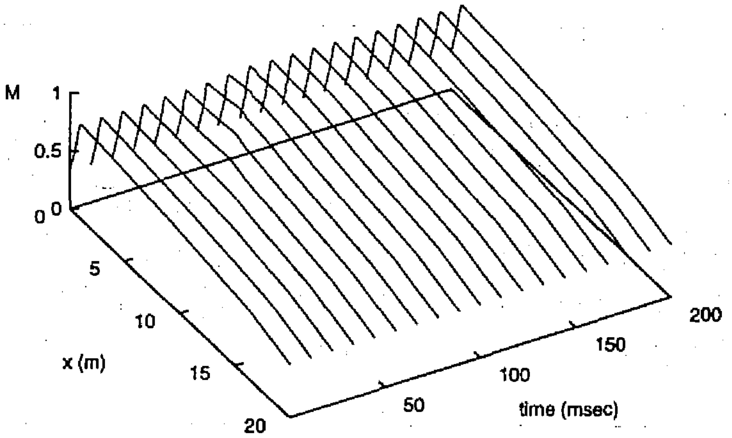

Figure 6.12: Time-dependent distribution of Mach number when firing fault occurs on inverter #41

and the increase of the load currents stops. The commutation of the inverters is, however, not restored to its normal operation. Consequently, the load currents cannot recover to the rated values. Since the load currents fluctuate following the commutation fault of inverters, the Mach number also fluctuates, in particular, in the upstream region of the generator.

The present system cannot recover to the nominal condition from the single-line ground fault unless the firing angle of the inverter is controlled. Then, the firing angle is set to be 90° at $t = 0.05$ sec after the line fault occurs. The decrease of the firing angle, which increases the margin angle, is expected to restore the normal inverter operation. Figure 6.17 shows the three-phase thyristor currents in the inverter #11, indicating that the inverter operation is recovered when the firing angle is reduced to 90°. After the faulted line is cut off, the firing angle gradually increases to the rated value with no commutation faults of the inverters. In Figure 6.18, the load currents gradually decrease to the rated values. Figure 6.20 shows the time-dependent distribution of Mach number with the operation of the firing angle of the inverter. The flow in the MHD channel is also restored to its nominal condition during the recovery of the load currents. Figure 6.19 plots the time-dependent variation of the transmission power. The transmission power fluctuates heavily until the faulted line is cut off. After the cutting the faulted line, the transmission power is restored to the rated value at about $t = 0.4$ sec.

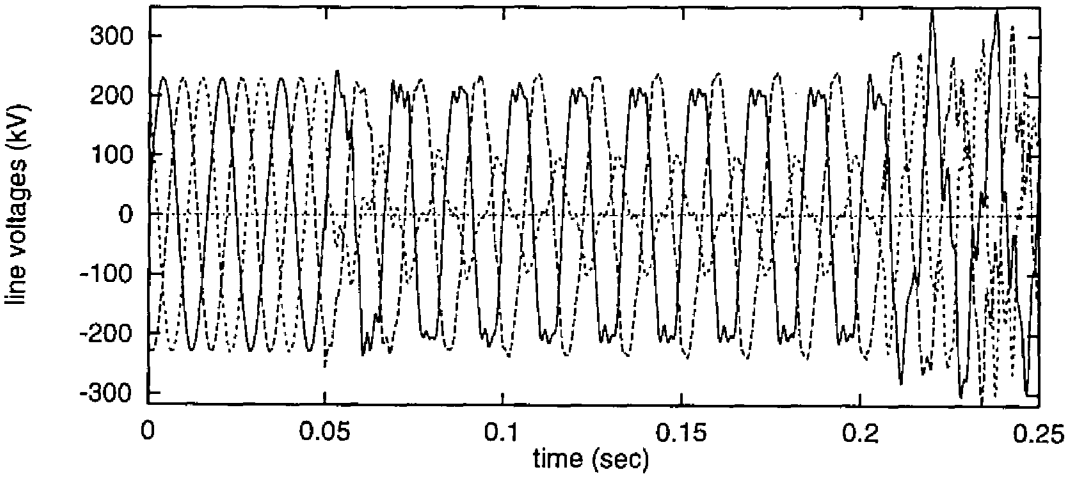

Figure 6.13: Time-dependent variations of three-phase line voltages (single-line ground fault, firing angle is constant at rated value)

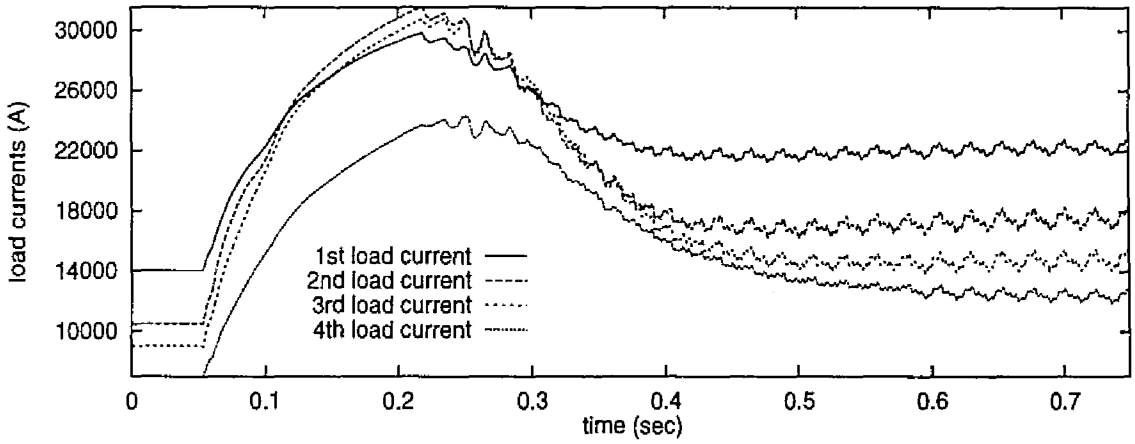

Figure 6.14: Time-dependent variations of load currents
(single-line ground fault, firing angle is constant at rated value)

6.6.3 Three-Phase Short Circuit Fault

In this subsection, the interconnecting system of MHD generator and AC power network is analyzed when a three-phase short-circuit fault occurs at the center of the transmission line. In the present analysis, the three-phase short-circuit fault occurs at $t = 0.05$ sec and the fault line is cut off at $t = 0.2$ sec, i.e., at 9 AC cycles after the fault. Figure 6.21 shows the time-dependent variation of three-phase line voltages. Figure 6.22 depicts the time-dependent variation of load currents of the MHD generator. Figures 6.23 shows the time-dependent distribution of the Mach number in the MHD generator. After the short-circuit fault, the voltages of the transmission line decrease sharply and the inverters are short-circuited. The load currents increase and the flow in the generator is accelerated. This behavior of the system is almost identical as the one with the single-line ground fault. Accordingly, the control of the firing angle of inverter is also required to restore the nominal condition after the three-phase short-circuit fault. In the present analysis, after the fault line is cut off, the firing angle is set to 90° in order to recover the commutation of the inverter. After the recovery of the commutation, the firing angle is increased to the rated value. Figures 6.24 and 6.25 show the three-phase thyristor currents in the inverter #11 and the time-dependent distribution of the Mach number, respectively. These figures show that the control of the inverter can restore the nominal operation of the MHD generation system.

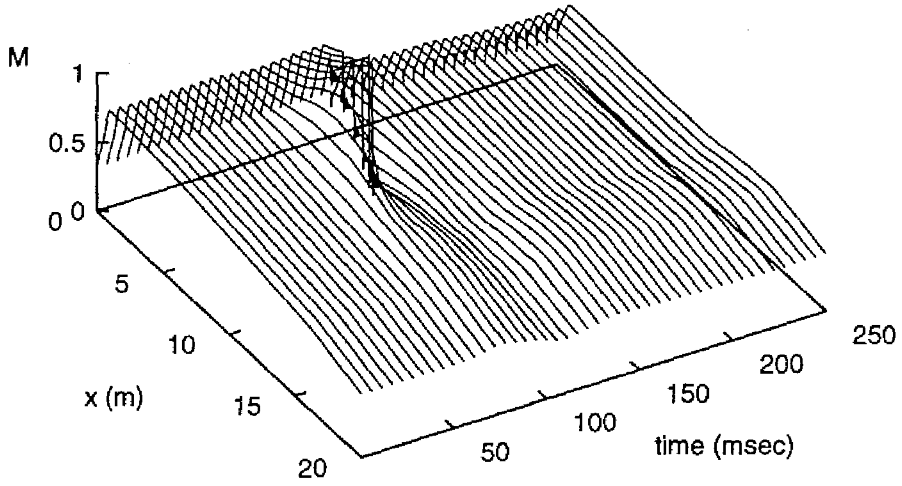

(a) $0 \leq t \leq 250$ msec

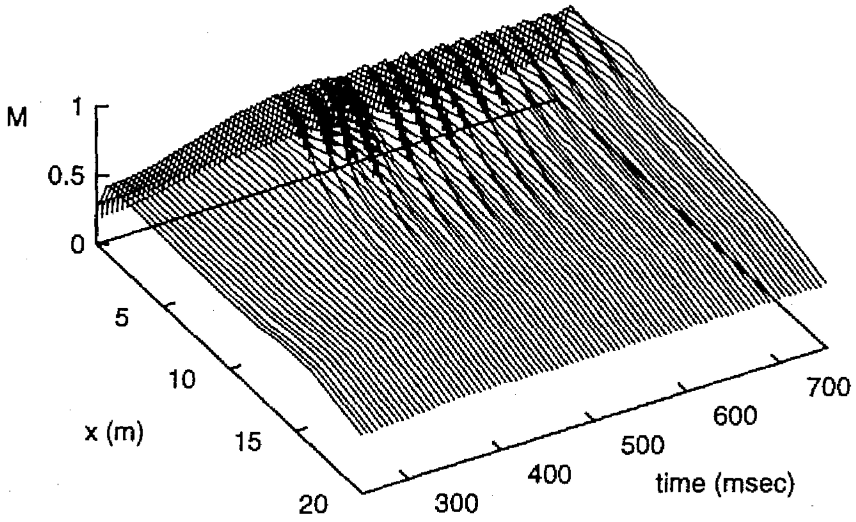

(b) $250 \leq t \leq 750$ msec

Figure 6.15: Time-dependent distribution of Mach number (single-line ground fault, firing angle is constant at rated value)

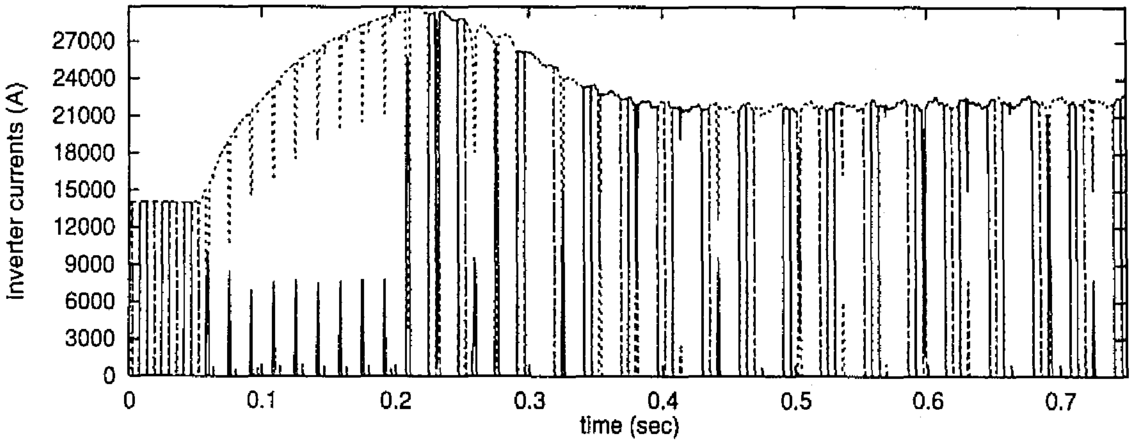

Figure 6.16: Time-dependent variations of three-phase currents of inverter #11 (single-line ground fault, firing angle is constant at rated value)

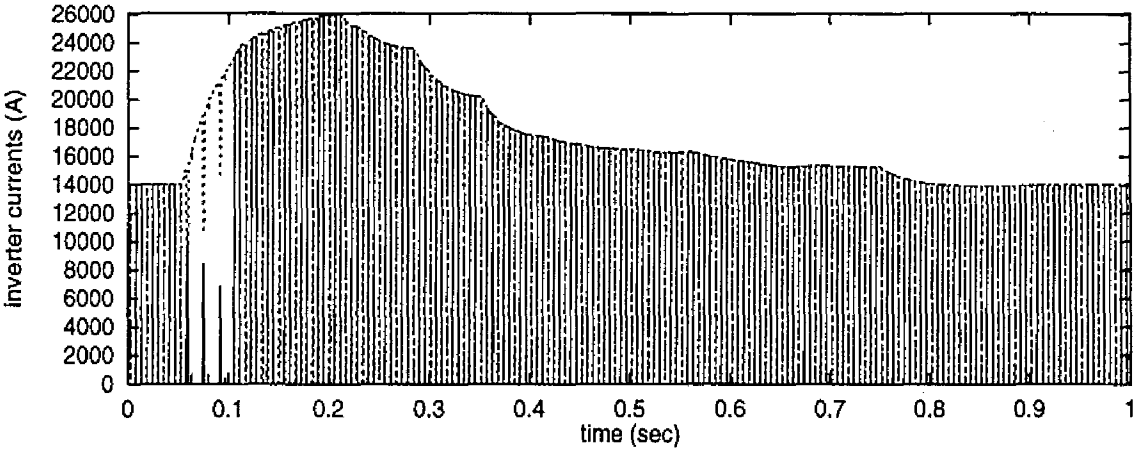

Figure 6.17: Time-dependent variations of three-phase currents of inverter #11 (single-line ground fault, firing angle is controlled)

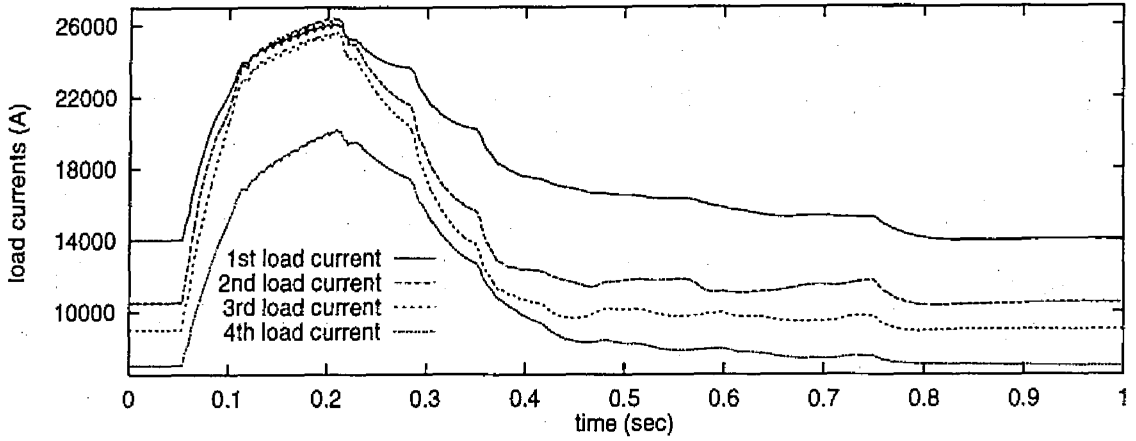

Figure 6.18: Time-dependent variations of load currents (single-line ground fault, firing angle is controlled)

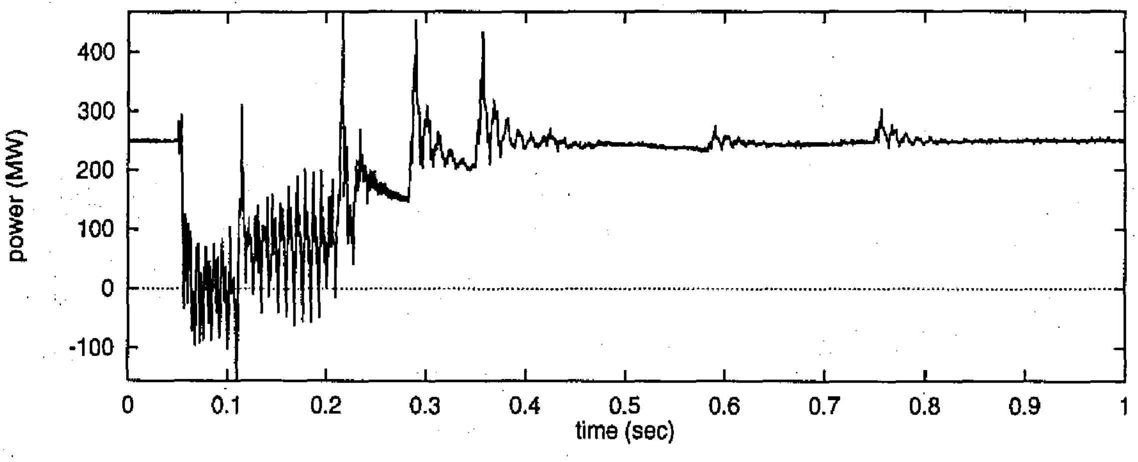

Figure 6.19: Time-dependent variations of transmission active power (single-line ground fault, firing angle is controlled)

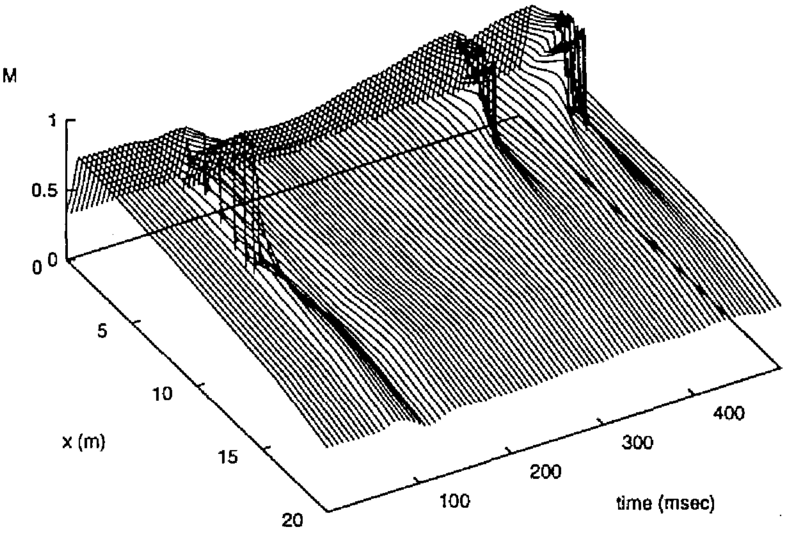

(a) $0 \leq t \leq 500$ msec

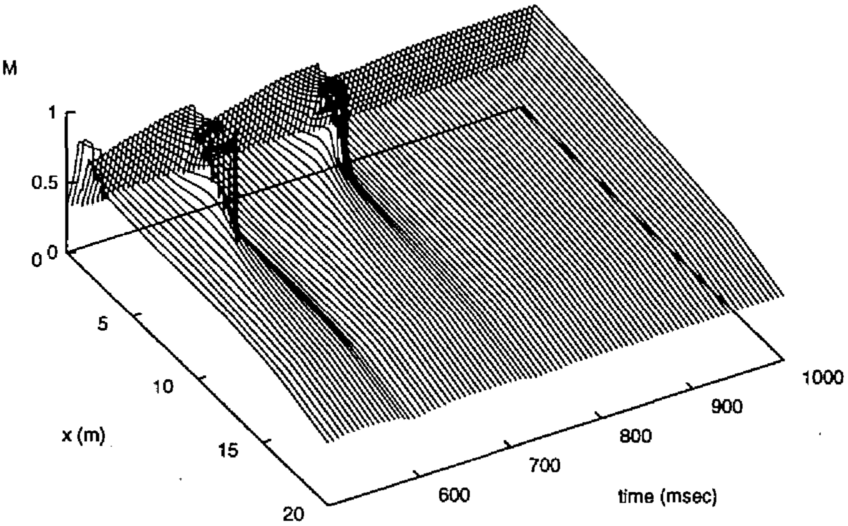

(b) $500 \leq t \leq 1000$ msec

Figure 6.20: Time-dependent distributions of Mach number (single-line ground fault, firing angle is controlled)

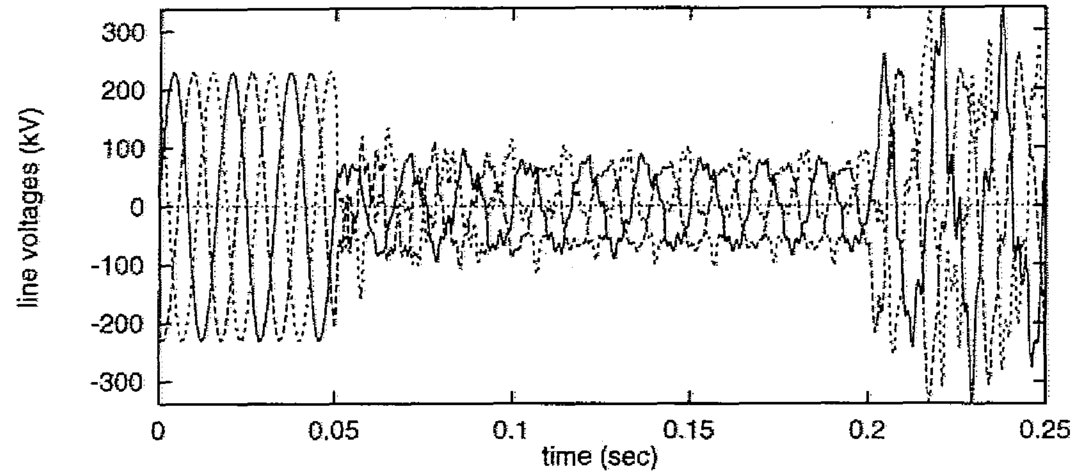

Figure 6.21: Time-dependent variations of three-phase line voltages
(three-phase short circuit fault)

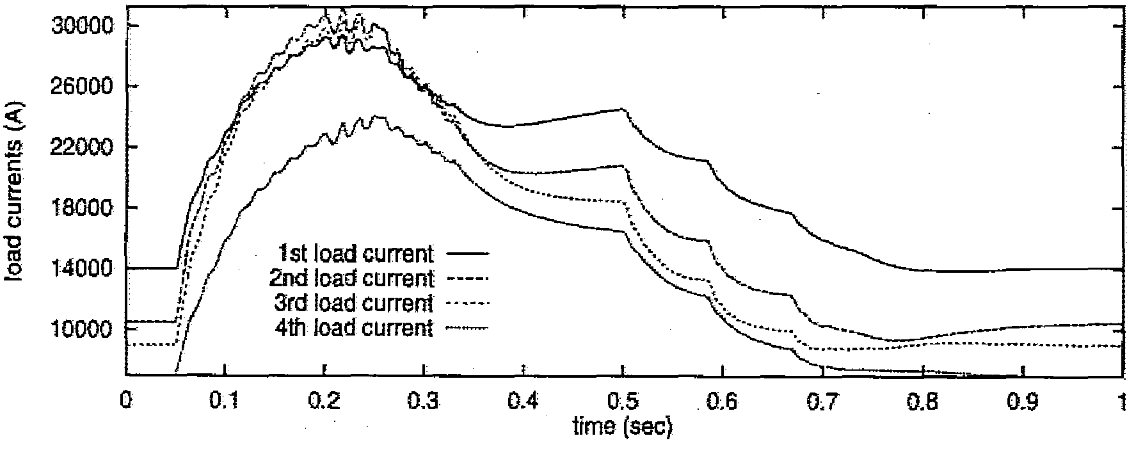

Figure 6.22: Time-dependent variations of load currents
(three-phase short circuit fault)

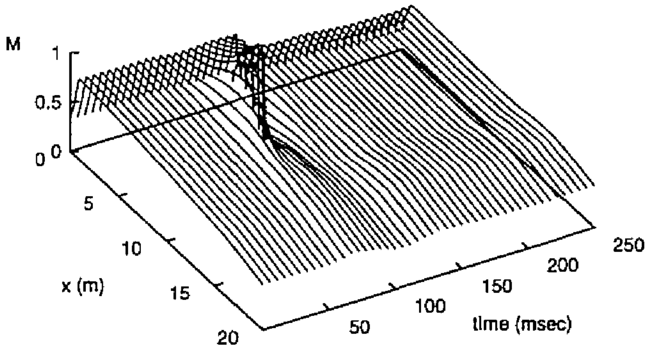

Figure 6.23: Time-dependent distribution of Mach number
(three-phase short circuit fault)

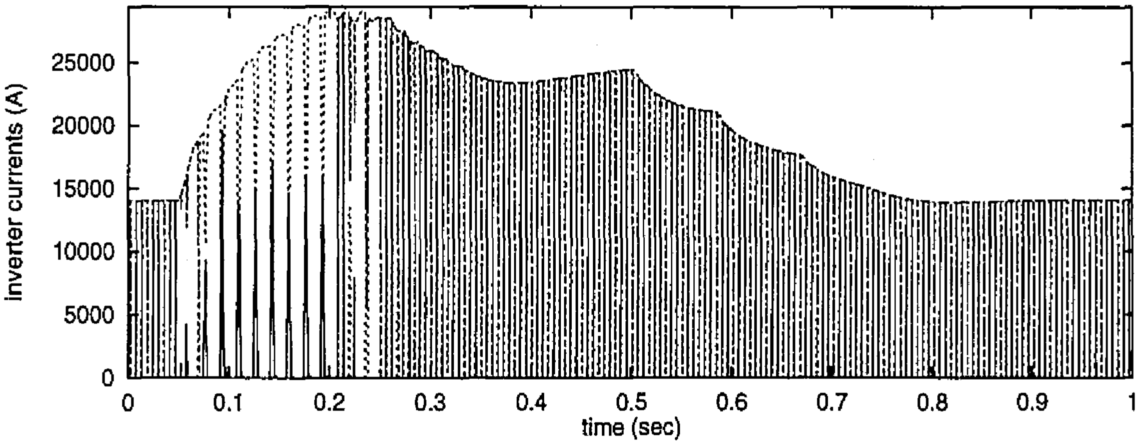

Figure 6.24: Time-dependent variations of three-phase currents of inverter#11
(three-phase short circuit fault)

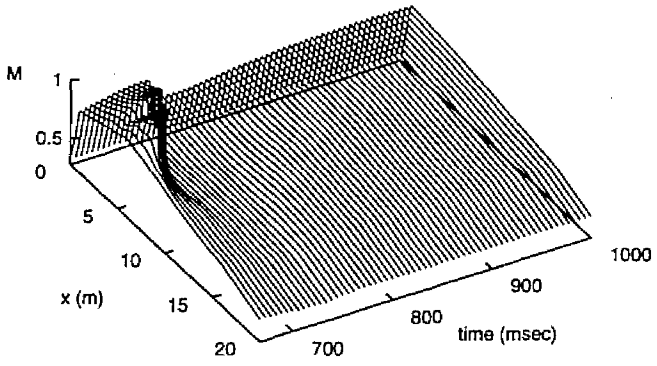

Figure 6.25: Time-dependent distribution of Mach number after firing angle is controlled (three-phase short circuit fault)

6.7 Concluding Remarks

The subsonic diagonal type MHD generator connected with AC power network is analyzed in this chapter. The following is a summary of the results of the analysis.

- The MHD generator works stably though periodic disturbances of load currents come into the generator from the inversion system.
- The MHD generator can provide the rated power output to the transmission line under the nominal condition.
- When line faults occur on the transmission line, the control of the firing angle is required for the recovery of the normal inverter operation. The control of the firing angle can restore the MHD generation system to the nominal operation.

Chapter 7 Conclusion

Chapter 2 treats the Chinese coal-fired Faraday type MHD channel at IEE. At first, three key parameters of the MHD channel are evaluated with the experimental data corresponding to experiments performed in 1992 and in 1993. It is found that (1) the effective electrical conductivity is 5/9 times that of the theoretical value, (2) the leakage resistance in the x-direction is 0.024 Ω, and (3) the leakage resistance in the y-direction is 82.4 Ω. These three parameters give simulation results which agree with experimental ones. Next, experimental data of power run in November, 1994, is analyzed to examine the effect of the modification of the channel, showing that the implemented improvement was effective in reducing the leakage current in the y-direction and resulted in the maximum power output (about 120 kW).

In Chapter 2, the performance of diagonal operation of the Chinese MHD channel is also estimated. The analysis shows that the diagonal operation will produce almost the same power output as the Faraday operation (98 kW). The load current is about 70 A with the load voltage of 1400 V. Finally, the hidden capability of the Chinese channel is estimated. This analysis indicates that the Chinese channel can yield the power output of over 400 kW if the electrical conductivity is improved to its theoretical value.

In Chapter 3, the sensitivity analysis, the linear stability analysis and the time-dependent calculation are carried out for the coal-fired supersonic diagonal type MHD generator of commercial-scale. These analyses show the following. (1) The growth rates of low frequency perturbations are small in the MHD generator with constant voltage loads or ohmic loads. (2) The growth of high frequency perturbations is suppressed by inserting inductors into the diagonal links. (3) For preventing the growth of load current fluctuation it is effective to subdivide the unstable loading sections. It is concluded that the generator with constant voltage loads or ohmic loads of the direct coupling scheme can be operated stably when the fluctuation of the electrode current is kept small.

In Chapter 4, the local linear perturbation analysis, the linear stability analysis of channel-length scale and the time-dependent calculation are performed for the coal-fired subsonic diagonal type MHD generator of commercial-scale. These analyses show that the conventional type generator, whose flow velocity is close to the velocity of sound, is apt to be unstable due to the high growth rate of the upstream acoustic wave. Then the author proposes the new subsonic channel in which the Mach number is relatively low in order to suppress the instability. The stability analyses show that the newly designed generator has the low growth rate of the upstream acoustic wave and can work stably. The linear stability analysis of channel-length scale and the time-dependent calculation indicate that the new generator can be operated stably under various loading conditions, for example constant current loading condition, constant voltage loading condition and ohmic loading condition.

In Chapter 5, the local linear perturbation analysis, the linear stability analysis of channel-length scale and the time-dependent calculation are carried out for the coal-fired Faraday type MHD generator of commercial-scale. These analyses show that the generator is stably operated with the constant current loads, the constant voltage loads or the ohmic loads whereas the generator becomes unstable with the constant load power.

In Chapter 6, the subsonic diagonal type MHD generator newly proposed in Chapter 4 is analyzed when the generator is connected with AC power network. The following is a summary of the results of the analysis. The MHD generator works stably though periodic disturbances of load currents come into the generator from the inversion system. The MHD generator can provide the rated power output to the transmission line under the nominal condition. When line faults occur on the transmission line, the nominal condition of the MHD power system can be recovered by the control of the inverter operation.

Acknowledgements

The author wishes to express his sincere and hearty appreciation to Professor Kohshi Okumura of Department of Electrical Engineering, Kyoto University for his useful advice and encouragements to complete this thesis.

The author would like to express his highest and sincere gratitude to Associate Professor Motoo Ishikawa of Department of Electrical Engineering, Kyoto University for his continual guidances and advice.

The author wishes to thank Professor Masaaki Shimasaki of Department of Electrical Engineering, Kyoto University for his encouragements.

The author would like to thank Professor Emeritus Juro Umoto of Kyoto University for his encouragements.

The author also wishes to express his sincere and hearty appreciation to Instructor Tetsuji Matsuo of Department of Electrical Engineering, Kyoto University for his guidances for the study on the stability of MHD generators, his useful advice and his encouragements to complete this work.

The author would like to thank Lecturer Yoshitaka Inui of Department of Electrical Engineering, Kyoto University for his guidances for the investigation on the interaction of MHD generator and AC power network and for useful discussions.

The author wishes to thank staffs of IEE, China for providing the experimental data of the Chinese MHD facility.

The author also wishes to thank Mrs. Maura Hurley and Mr. Gautam Basu for their correction of English usage in this thesis.

The author would like to thank staffs of Shimasaki's laboratory for their encouragements.

Bibliography

1) R. J. Rosa, "Magnetohydrodynamic Energy Conversion", McGraw-Hill, New York (1968).

2) J. N. Chapman, "Environmental Aspects: SOx and NOx Removal, Seed Regeneration and Recovery", 1995 MHD Status Report (1995).

3) M. Ishikawa and J. Umoto, "Environmentally Attractive Oxygen-Coal-Fired MHD-Steam Combined System with CO_2 Recovery", Energy Conversion and Management, Vol. **34**, No. 8, pp.597-605 (1993).

4) J. Zixiang and J. T. Lineberyy, "The Status and Some Key Problems of Open Cycle MHD Research", Proc. 12th Int. Conf. MHD Electr. Power Generation, Vol. 1, pp.16-27 (1996).

5) S. Kabashima and H. Yamasaki, "Recent Progress in Closed Cycle Nonequilibrium MHD Power Generation", Proc. 12th Int. Conf. MHD Electr. Power Generation, Vol. 1, pp.1-15 (1996).

6) W. R. Owens et al., "Open Cycle MHD System", 1995 MHD Status Report (1995).

7) A. T. Hart and D. A. Lofftus, "Coal-Fired MHD Test Progress at the Component Development and Integration Facility", Proc. 32nd Symp. Engng. Aspects MHD, Ses. 2 (1994).

8) R. C. Attig, J. N. Chapman and N. R. Johanson, "Status of Proof-Of-Concept Testing at the Coal-Fired Flow Facility-93", Proc. 31st Symp. Engng. Aspects MHD, II. 5 (1993).

9) V. M. Batenin et al., "Directions of Improving MHD Power Plants", 11th Int. Conf. MHD Electr. Power Generation, Vol. 5, 1372 (1992).

10) Y. Aiyama, "MHD Research Activities in Japan", Proc. 9th Int. Conf. MHD Electr. Power Generation, Vol. 5, pp.1768-1770 (1986).

11) H. K. Messerle, "MHD-Related Work in Australia", Proc. 9th Int. Conf. MHD Electr. Power Generation, Vol.5 pp.1803-1807 (1986).

12) J. Tong, C. Huang, Q. Ni and S. Pei, "Design and Preliminary Test of A Coal-Combustion Driven Faraday-Type MHD Generator Channel with 25MW Thermal Input", Proc. 31st Symp. Engng. Aspects MHD, VII. 2 (1993).

13) S. A. Arunachalam, V. R. Malghan and K.Thiagarajan, "Indian MHD Program -Status Review ", Proc. 31st Symp. Engng. Aspects MHD, I. 2 (1993).

14) F. Negrini, "Status of MHD Research and Development Activities in Italy", Proc. 10th Int. Conf. Electr. MHD Power Generation, Vol. I, I.27 (1989).

15) Committee of investigation of MHD power generation technology, IEE Japan, "Plasma MHD Power Generation", IEE Tech. Report No. 621 (1997) (In Japanese).

16) Y. Luguang, J. Zixiang and S. Ciwen, "Progress and National Program of MHD Generator in China", Proc. 32nd Symp. Engng. Aspects MHD, Ses. 1 (1994).

17) Q. Ni, J. Tong, B. Wang, Y. Zhao, L. Yao and X. Meng, "The Performance of an Experimental Coal-Fired MHD Generator with 25MW Thermal Input", Proc. 32nd Symp. Engng. Aspects MHD, Ses. 3 (1994).

18) J. Tong and Q. Ni, "Recent Progress in Experiment and Performance Evaluation of Chinese 25 MWt Coal-Fired MHD Generator", Proc. 33rd Symp. Engng. Aspects MHD, II. 2(1995).

19) Q. Ni, J. Tong, Y. Zhao, X. Meng, Y.Cui, S. Cheng and J. Wu, "A Study on Electrical Nonuniformity of an Experimental Coal-Fired MHD Generator", Proc. 12th Int. Conf. Electr. MHD Power Generation, Vol. 1, pp.142-147 (1996).

20) Q. Ni, G. Lou, J. Wang, Y. Kan, X. Meng, Y.Zhao, L. Yao and J. Tong, "The Latest Experimental and Analytical Results of Chinese 25MWt Coal-Fired MHD Generator", Proc. 34th Symp. Engng. Aspects MHD, 1.1 (1997).

21) Y. Fujita,"Analytical Study on Design and Performance of Commercial-Scale Coal-Fired MHD Generator with 1300 MWth", Master thesis, Department of Electrical Engineering, Kyoto University (1993) (In Japanese).

22) E. P. Velikhov, "Hall Instability of Current-Carrying Slightly-Ionized Plasmas", Proc. 1st Int. Symp. MPD Electr. Power Generation, Newcastle upon Tyne, pp.135-162 (1962).

23) J. E. McCune, "Wave Growth and Instability in Partially Ionized Gases", Proc. 2nd Int. Symp. MHD Electr. Power Generation, Paris, pp.523-538 (1964).

24) E. V. Locke and J. E. McCune, "Growth Rates for Axial Magneto-Acoustic Waves in a Hall Generator", AIAA J., **4**, 10, pp.1748-1751 (1966).

25) W. L. Powers and J. B. Dicks, "Transient Wave Growth in Magnetogasdynamic Generator", AIAA J., **6**, 6, pp.1007-1012 (1968).

26) M. Ishikawa, A. Kyogoku and J. Umoto, "Stability of Large-Scale MHD Channels Designed for Coal-Fired MHD Power Generation", Energy Conversion and Management, **37**, No. 1, pp.31-41 (1996).

27) I. M. Rutkevich and P. M. Tokar, "Stability of the Non-Uniform Subsonic Flows in the Open Cycle MHD Generators", Proc. 9th Int. Conf. MHD Electr. Power Generation, Tsukuba, pp.1620-1629 (1986).

28) V. I. Komov and I. M. Rutkevich, "Stability of Subsonic Plasma Flows in Disk MHD Generators", Proc. 11th Int. Conf. MHD Power Generation, Beijing, pp.1712-1719 (1992).

29) F. J. Fishman, "Instability of Hall MHD Generators to Magneto-Acoustic Waves", AIAA J., **8**, 4, pp.632-639 (1970).

30) S. M. Marty, F. J. Fishman, S. W. Simpson and H. K. Messerle, "Operating Characteristics of MHD Disk Generators", 23th Symp. Eng. Aspects of MHD, pp.605-623 (1985).

31) T. Matsuo, M. Ishikawa and J. Umoto, "Stability of Open-Cycle Supersonic Disk MHD Generator", Energy Conversion and Management, Vol. **38**, No. 3, pp.287-300 (1997).

32) T. Matsuo, M. Ishikawa and J. Umoto, "Stability Analysis of Open-Cycle Subsonic Disk MHD Generator", Trans. IEE of Japan, Vol. **116**-B, No. 3, pp.360-366 (1996) (In Japanese).

33) Committee of investigation of MHD power generation technology, IEE Japan, "Present Status of MHD Power Generation Technology", IEE Tech. Report No. 309 (1989).

34) M.Petrick and B.Ya.Shumyatskey (Editors), "Open-Cycle Magnetohydrodynamic Electrical Power Generation", pp. 275-319 (1978).

35) N. Hayanose, M. Ishikawa and J. Umoto, "Behavior of Binary Combined System of MHD and Synchronous Generators Including Power Transmission System", 11th Int. Conf. MHD Electr. Power Generation, pp. 135-142 (1992).

36) N. Hayanose, A. L. Tan, T. Matsuo, Y. Inui, M. Ishikawa and J. Umoto, "A Study of Behavior of Open Cycle Multi-Load Disk Type MHD Generator Connected to Power Transmission System", 12th Int. Conf. MHD Electr. Power Generation, Vol. 2, pp.843-852 (1996).

37) M.Ishikawa, "Unsteady Phenomena in High-Interaction MHD Generators",Tech. Rep. Institute of Atomic Energy Kyoto Univ., No 192(1982).

38) D. A. Oliver, R.D. Crouse, C. D. Maxwell and S. T. Demetriades, "Transient Processes in Large Magnetohydrodynamic Generator Flowtrains", Proc. 7th Int. Conf. MHD power Electrical Power Generation, 4 (1980).

39) K.Takano and K.Kato, "Calculation Code of Properties of Combustion Gas for MHD Power Generation", 11th Symp. Efficient Use of Energy and Direct Electrical Power Generation, pp.173-184 (1989) (In Japanese).

40) D. A. Oliver, "The Time Dependent Magnetohydrodynamic Generator", Proc. 14th Symp. on Engng. Aspect MHD, V.5 (1974).

41) M. Ishikawa, Y. F. Liao, Y. C. L. Wu and M. H. Scott, "Time-Dependent Analysis of Fault Currents in Mid-Channel Power Takeoff of a DCW MHD Generator", Proc. 20th Symp. on Engng. Aspect MHD, 7.3 (1982).

42) M. Ishikawa, T.Suemura, M.Fujita and J.Umoto, "Behavior of Coal-Fired Supersonic Diagonal Type MHD Generator with External Control Circuit", 29th Symp. Engng Aspects MHD, 9.1 (1991).

43) M. Yoshida and J. Umoto, "A New Quasi-Two-Dimensional Analysis of Whole Electrical and Gasdynamical Performances of Linearly-Diverging Diagonal Type Generator", Proc. 7th Int. Conf. MHD, Vol. 2, pp.524-529 (1980).

44) H. Schlichting, "Boundary Layer Theory", 6th edn. McGraw-Hill (1968).

45) M. Ishikawa, M. Fujita, Y. Fujita and J. Umoto, "Performance of Coal-Fired MHD Generators with Large Leakage Current" Energy Conversion and Management, Vol. **34**, No.8, pp.607-617 (1993).

46) A. Kyogoku, "Stability of Large-Scale Coal-Fired MHD Generators"', Master thesis, Department of Electrical Engineering, Kyoto University (1994) (In Japanese).

47) T.Matsuo, M. Ishikawa and J. Umoto, " Local Growth Rates of Traveling Waves in Open-Cycle MHD Channels", Proc. 12th Int. Conf. MHD Electr. Power Generation, Vol. 2, pp.691-700 (1996).

48) Y. Inui, H. Sugita, M. Ishikawa and J. Umoto, "Behavior of He-Cs Closed-Cycle Disk MHD Generator Connected to Electric Power System Through Line-Commutated Inverter", Energy Conversion and Management, **38**, No. 7, pp.625-635 (1997).

49) Technical Report of the Investigation Committee of MHD Generator Plant in Japan (1982) (In Japanese).

References by the Author

50) T. Iwashita, T. Matsuo, M. Ishikawa and J. Umoto, "Analysis of Performance Characteristic of Multi-Loaded Supersonic Diagonal Type MHD Generator", Record of the 1993 Kansai-Section Joint Convention of Institutes of Electrical Engineering, Japan, G4-17 (1993) (In Japanese).

51) A. Kyogoku, T. Iwashita, M. Ishikawa and J. Umoto, "Stability Analysis of Coal-Fired Large-Scale Diagonal Type MHD Generator", 1994 National Convention Record I.E.E. Japan, 1653 (1994) (In Japanese).

52) T. Iwashita, T. Matsuo, M. Ishikawa and J. Umoto, "Sensitivity Analysis of Large-Scale Coal-Fired Diagonal Type MHD Generator with Inlet Gasdynamical Perturbations", Record of the 1994 Kansai-Section Joint Convention of Institutes of Electrical Engineering, Japan, G5-51 (1994) (In Japanese).

53) T. Iwashita, T. Matsuo, M. Ishikawa and J. Umoto, "Effects of Loading Condition on Stability of Diagonal Type MHD Generator", Proc. 17th Symp, Efficient Use of Energy and Direct Electrical Power Generation, pp.153-162 (1995) (In Japanese).

54) M. Ishikawa, T. Iwashita and J. Tong, "Leak Current in the Faraday Direction of Coal-Fired MHD Channel (China, IEE)", 1995 National Convention Record I.E.E. Japan, 1833 (1995) (In Japanese).

55) T. Iwashita, T. Matsuo, M. Ishikawa and J. Umoto, "Stability Dependence on Loading Condition of Supersonic Diagonal Type MHD Generator", 1995 National Convention Record I.E.E. Japan, 1834 (1995) (In Japanese).

56) M. Ishikawa, T. Iwashita, and J. Tong, "Preliminary Analyses of Coal-Fired MHD Power Experiments Carried Out at IEE, China", 26th AIAA PDLC, 95-1932 (1995).

57) M. Ishikawa, T. Iwashita, and J. Tong, "Numerical Analysis of 25 MWth Coal-Fired MHD Generator at IEE, China", Proc. 33rd Symp. Engng. Aspects MHD, pp.2.3-1-2.3.12 (1995).

58) T. Iwashita, T. Matsuo, M. Ishikawa and J. Umoto, "Examination of Loading Condition for Stabilization of Supersonic Diagonal Type MHD Generator", Proc. 6th Annual Conf. Power and Energy Society. IEE of Japan, Session II, 27 (1995) (In Japanese).

59) T. Iwashita, T. Matsuo, M. Ishikawa and J. Umoto, "Stability Analysis of Large-Scale Subsonic Diagonal Type MHD Generator Considering Inlet and Exit Boundary Conditions", IEE of Japan Trans on ESC, ESC-95-22 (1995) (In Japanese).

60) T. Iwashita, T. Matsuo, M. Ishikawa and J. Umoto, "Conceptual Design for Stabilization of Commercial-Scale Subsonic Diagonal Type MHD Generator", Record of the 1995 Kansai-Section Joint Convention of Institutes of Electrical Engineering, Japan, G5-22 (1995) (In Japanese).

61) T. Iwashita, T. Matsuo, M. Ishikawa and J. Umoto, "Conceptual Design of Commercial-Scale Subsonic Diagonal Type MHD Generator - Suppression of Magneto-Acoustic Instability -", Proc. '96 Symp. Advanced Research of Energy Technology, pp. 91-100 (1996) (In Japanese).

62) M. Ishikawa, T. Iwashita and J. Tong, "Performance Analysis of Diagonal Operation of Coal-Fired MHD Channel (China, IEE)", 1996 National Convention Record I.E.E. Japan, 1733 (1996) (In Japanese).

63) T. Iwashita, T. Matsuo, M. Ishikawa and J. Umoto, "Stability Analysis of Large-Scale Coal-Fired Subsonic Diagonal Type MHD Generators Considering Inlet and Exit Conditions", 27th AIAA PDLC, 96-2344 (1996).

64) T. Iwashita, T. Matsuo, M. Ishikawa and J. Umoto, "Stabilization Analysis of Supersonic Diagonal Type MHD Generators of Commercial Scale", Trans. IEE of Japan, Vol. **116**-B, No. 8 pp.973-978 (1996) (In Japanese).

65) T. Iwashita, T. Matsuo, M. Ishikawa and J. Umoto, "Effects of Loading Conditions on Stability of Subsonic MHD Generator of Commercial Scale", IEE of Japan Trans on ESC, ESC-96-17 (1996) (In Japanese).

66) M. Ishikawa, T. Iwashita and J. Tong, "Analysis of Faraday and Diagonal Modes of Coal-Fired MHD Generator at IEE, China", Proc. 12th Int. Conf. MHD Electr. Power Generation, Vol. 1, pp.116-125 (1996).

67) T. Iwashita, T. Matsuo, M. Ishikawa and J. Umoto, "Stabilization Analysis of Coal-fired Subsonic Diagonal Type MHD Generator of Commercial Scale", Proc. 7th Annual Conf. Power and Energy Society. IEE of Japan, Session I, 22 (1996) (In Japanese).

68) T. Iwashita, T. Matsuo, M. Ishikawa and J. Umoto, "Stabilization of Commercial-Scale Coal-Fired Subsonic Diagonal Type MHD Generator", Proc. 12th Int. Conf. MHD Electr. Power Generation, Vol. 2, pp.896-905 (1996).

69) T. Iwashita, T. Matsuo, M. Ishikawa and J. Umoto, "Channel-Length Scale Linear Stability Analysis of Subsonic Faraday Type MHD Generator of Commercial-Scale", Record of the 1996 Kansai-Section Joint Convention of Institutes of Electrical Engineering, Japan, G5-4 (1996) (In Japanese).

70) T. Iwashita, T. Matsuo, M. Ishikawa and J. Umoto, "Stability of Commercial-Scale Coal-Fired Subsonic MHD Generators Operated with Loads Including Inductance", '97 Symp. Advanced Research of Energy Technology (1997) (In Japanese).

71) T. Iwashita, T. Matsuo, Y. Inui, M. Ishikawa and J. Umoto, "Analysis of Interconnecting System of Commercial-scale Subsonic Diagonal Type MHD Generator and AC Power System Using a Simplified Model of MHD Generator", 1997 National Convention Record I.E.E. Japan, 1893 (1997) (In Japanese).

72) K. Tateishi, T. Iwashita, M. Kajiwara, T. Matsuo, Y. Inui and M. Ishikawa, "Two-Dimensional Time-Dependent Analysis of 25MWth Coal-Fired MHD Generator at China", 1997 National Convention Record I.E.E. Japan, 1892 (1997) (In Japanese).

73) M. Ishikawa, T. Iwashita and J. Tong, "Performance Analysis of Coal-Fired MHD Faraday Channel at IEE, China", Energy Conversion and Management, **38**, No. 5, pp.499-510 (1997).

74) T. Iwashita, T. Matsuo, M. Ishikawa and J. Umoto, "Stabilization Analysis of Coal-Fired Subsonic Diagonal Type MHD Generators of Commercial Scale - Improvement of Stability of MHD Generators with Reduced Velocity -", Trans. IEE of Japan, Vol. **117**-B, No. 6, pp.864-871 (1997) (In Japanese).

75) T. Iwashita, T. Matsuo, M. Ishikawa and J. Umoto, "Effects of Loading Conditions on Stability of Commercial-Scale Diagonal Type MHD Generator", Proc. 34th Symp. Engng. Aspects MHD, pp. 7.2.1-7.2.10 (1997).

76) T. Iwashita, T. Matsuo, M. Ishikawa and J. Umoto, "Stability of Subsonic MHD Generators Operated with Partially Ionized Coal Combustion Gas", 28th AIAA PDLC, 97-2376 (1997).

77) T. Iwashita, T. Matsuo, Y. Inui, M. Ishikawa and J. Umoto, "Stabilization Analysis of Commercial-Scale Subsonic Diagonal Type MHD Generator Considering Loading Conditions", Proc. the 8th Annual Conf. Power and Energy Society. IEE of Japan, Session I, pp.193-198 (1997) (In Japanese).

78) T. Iwashita, T. Matsuo, M. Ishikawa and J. Umoto, Fault Analysis of Interconnecting System of Commercial Scale Subsonic MHD Generator between AC Power System, IEE of Japan Trans on ESC, ESC-97-24 (1997) (In Japanese).

Appendix A Boundary Layer and Slag Layer

The quasi one-dimensional analysis used in the present thesis cannot treat the effects of the boundary layer and the slag layer in detail. In the present analysis, the approximate equations shown below are used for accounting the effects of the boundary layer and the slag layer.

(1) Friction loss and heat loss [37)]

The friction f_{ric} and the heat loss q_{loss} are estimated according to the turbulent boundary layer theory [44)]:

$$\begin{aligned} f_{ric} &= 2D\rho u^2 c_f \\ c_f &= \{2.87 + 1.58 \log(x^*/k_s)\}^{-2.5} \\ x^* &= 1 + x \text{ m} \\ k_s &= 0.003 \text{ m} \\ D &= \sqrt{A} \end{aligned} \tag{A.1}$$

$$\begin{aligned} q_{loss} &= q_t + q_r \\ q_t &= 2D\rho u C_p c_f (T_s - T_w) \\ q_r &= 4D\sigma_B C_r (T^4 - T_w^4) \\ \sigma_B &= 5.66 \times 10^{-8} \text{ J/sm}^2\text{K}^4 \\ C_r &= 0.41 \end{aligned} \tag{A.2}$$

where q_t is the heat loss due to the heat transfer on the wall, q_r the heat loss due to the radiation, c_f the friction factor, C_p the constant pressure specific heat of the gas, D the hydraulic diameter, k_s the equivalent sand roughness representing the roughness level of walls, T the gas temperature, T_s the stagnation temperature, T_w the wall temperature, x^* the modified duct length to eliminate the singularity, C_r the coefficient relating to the coal-slag carry-over and σ_B the Stefan-Boltzmann constant. In the present analysis, the wall temperature is set to be 1800 K which is the melting point of coal-slag.

(2) Electrode voltage drop

In the boundary layer, the flow velocity and the gas temperature are much smaller than in the main flow. Consequently, the electromotive force and the electrical conductivity also decrease substantially and the voltage drop is induced near electrodes. In the present analysis, the voltage drop is given by the next approximate equation proposed in Ref. 33).

$$\begin{aligned} \Delta V &= 70.0 + 292\left(\frac{|J_y|}{J^*}\sqrt{1+\beta^2}\right) \mathrm{V} \\ J^* &= \sqrt{q_t \sigma / \delta} \end{aligned} \tag{A.3}$$

where δ is the boundary layer thickness.

Appendix 2

Appendix B Composition of Coal

In the present analysis, the thermodynamical properties of coal are calculated with thermodynamical equilibrium approximation taking into account the composition of coal. Table B.1 lists the composition of the coal used in Chinese experiments [17].

Table B.1: Composition of coal in Chinese experiments

		Power run in 1992	Power run in 1993
Proximate Analysis	Moisture %	2.26	2.01
	Ash %	17.76	19.02
	Sulfur %	0.78	0.85
	Volatile %	25.22	24.94
	HHV MJ/kg	26.22	26.21
Ultimate Analysis	Carbon %	65.80	65.16
	Hydrogen %	3.75	3.54
	Nitrogen %	0.70	0.68
	Oxygen %	9.07	8.74
Ash Composition	SiO_2 %	56.94	57.74
	Al_2O_3 %	20.11	21.64
	TiO_2 %	1.14	1.04
	Fe_2O_3 %	11.25	9.00
	CaO %	3.32	3.59
	MgO %	0.87	1.37
	Na_2O %	0.54	0.49
	K_2O %	1.59	1.80
	SO_3 %	2.54	1.58

Table B.2 lists the composition of the Datung coal [49)] used in Chapter 3, 4, 5 and 6.

Table B.2: Composition of Chinese Datung coal

		Chinese Datung coal
Proximate Analysis	Moisture %	2.9
	Ash %	8.9
	Sulfur %	0.7
	Volatile %	28.2
	HHV MJ/kg	30.1
Ultimate Analysis	Carbon %	79.9
	Hydrogen %	4.5
	Nitrogen %	0.9
	Oxygen %	7.0
Ash Composition	SiO_2 %	47.61
	Al_2O_3 %	17.91
	Fe_2O_3 %	19.41
	CaO %	5.48
	MgO %	2.05
	Na_2O %	0.30
	SO_3 %	3.99

Appendix C Assumption in Linear Stability Analysis

In the linear stability analysis used in Chapter 3, whether or not $\Delta_k(s)$ has a zeropoint in the right half plain ($\mathrm{Re}(s) > 0$) is judged by plotting the locus of $\Delta_k(\mathrm{j}\omega)(\omega : -\infty \rightarrow \infty)$. There exists a zeropoint in the right half plain if the locus turns clockwise around the origin. This analysis requires the assumption that the transformation: $s \rightarrow \Delta_k(s)$ transforms the right half plain into the right-hand side of the locus $\Delta_k(\mathrm{j}\omega)(\omega : -\infty \rightarrow \infty)$. We can examine whether or not the assumption holds by plotting values of $\Delta_k(s)$ for various points s.

For example, we plot values of $\Delta_4(s)$ for various points s when the supersonic MHD generator is connected with four constant voltage loads. Figure C.1 plots the loci of $\Delta_4(\alpha + \mathrm{j}\omega)(\alpha = -20, -10, 0, 10, 20, 30, 40\ \omega \geq 0)$. Figure C.1 indicates that transformation: $s \rightarrow \Delta_4(s)$ transforms the right half plain into the right-hand side of the locus $\Delta_4(\mathrm{j}\omega)(\omega : -\infty \rightarrow \infty)$. The assumption in the other cases can be also confirmed in the same way as mentioned above.

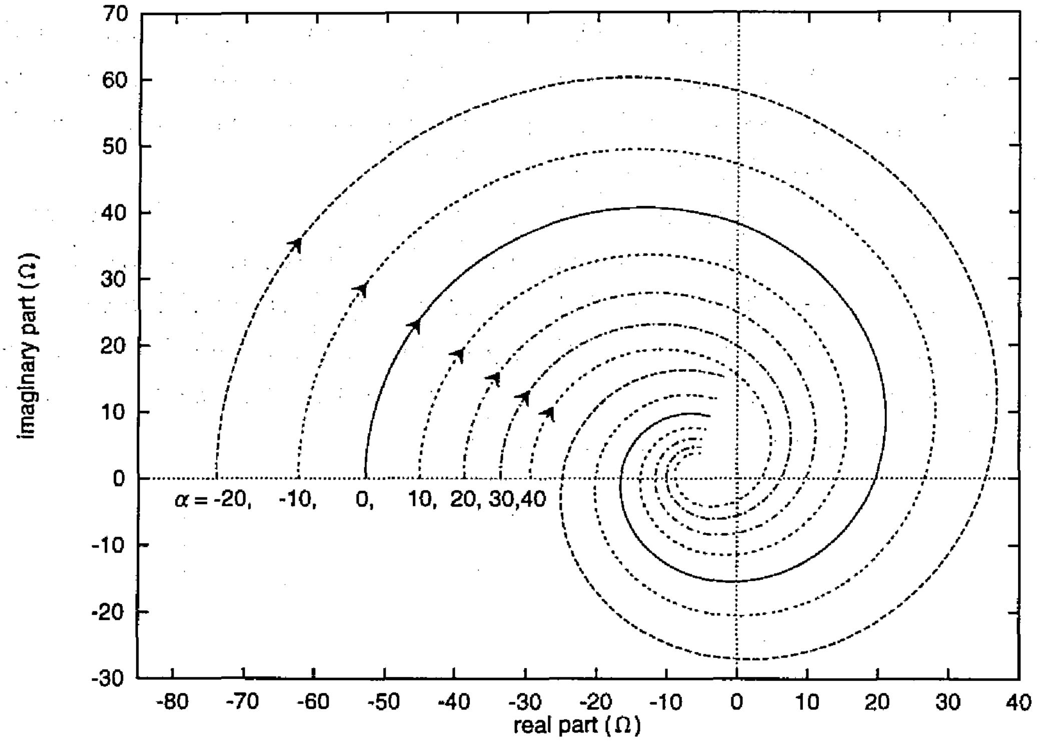

Figure C.1: The loci of $\Delta_4(\alpha + j\omega)(\alpha = -20, -10, 0, 10, 20, 30, 40\ \omega \geq 0)$